Potassium channels, megapolarization, and water pore formation are key determinants for cationic cell-penetrating peptide translocation into cells

Evgeniya Trofimenko[2], Gianvito Grasso[1,3], Mathieu Heulot[1,2], Nadja Chevalier[1,2], Marco A. Deriu[4], Gilles Dubuis[2], Yoan Arribat[2], Marc Serulla[2], Sébastien Michel[2], Gil Vantomme[5], Florine Ory[2], Julien Puyal[5], Francesca Amati[2,6], Anita Lüthi[5], Andrea Danani[3], and Christian Widmann[2,7]

[1]equal contribution

[2]Department of Physiology, University of Lausanne, 1005 Lausanne, Switzerland
[3]Dalle Molle Institute for Artificial Intelligence (IDSIA), Scuola Universitaria Professionale della Svizzera italiana (SUPSI), Università della Svizzera italiana (USI), Centro Galleria 2, Manno, CH-6928, Switzerland.
[4] Polito[BIO]Med Lab Department of Mechanical and Aerospace Engineering, Politecnico di Torino, 10129 Turin, Italy
[5]Department of Fundamental Neurosciences, University of Lausanne, 1005 Lausanne, Switzerland
[6]Institute of Sports Sciences, University of Lausanne, 1005 Lausanne, Switzerland

[7]Corresponding author

Keywords: potassium channels, cell-penetrating peptides, membrane potential, water pores

Address correspondence: Christian Widmann, Department of Physiology, Rue du Bugnon 7, 1005 Lausanne, Switzerland, Phone: +41 21 692 5123, Fax: +41 21 692 5505, E-mail: Christian.Widmann@unil.ch.

Summary

Cell-penetrating peptides (CPPs) allow intracellular delivery of cargo molecules. CPPs provide efficient methodology to transfer bioactive molecules in cells, in particular in conditions when transcription or translation of cargo-encoding sequences is not desirable or achievable. The mechanisms allowing CPPs to enter cells are ill-defined and controversial. This work identifies potassium channels as key regulators of cationic CPP translocation. Using a CRISPR/Cas9-based screening, we discovered that KCNQ5, KCNN4, and KCNK5 positively modulate CPP cellular direct translocation by reducing transmembrane potential (V_m). Cationic CPPs further decrease the V_m to megapolarization values (about -150 mV) leading to the formation of ~2 nm-wide water pores used by CPPs to access the cell's cytoplasm. Pharmacological manipulation to lower transmembrane potential boosted CPPs cellular uptake in zebrafish and mouse models. Besides identifying the first genes that regulate CPP translocation, this work characterizes key mechanistic steps used by CPPs to cross cellular membrane. This opens the ground for pharmacological strategies augmenting the susceptibility of cells to capture CPP-linked cargos *in vitro* and *in vivo*.

46 **Introduction**

47 Cell-penetrating peptides (CPPs) are non-toxic molecules of 5-30 amino acids that can
48 translocate into living cells. CPPs can be hooked to a variety of cargos (siRNAs, DNA,
49 polypeptides, liposomes, nanoparticles, etc.) to allow their transport into cells for
50 therapeutic or experimental purposes (*1-10*). The origin of CPPs is diverse. For
51 example, TAT_{48-57} is a 10 amino-acid fragment derived from the trans-activator of
52 transcription (TAT) HIV-1 protein (*11, 12*), penetratin is a 16 amino-acid peptide
53 derived from the Antennapedia *Drosophila melanogaster* protein (*13*), and MAP (model
54 amphipatic peptide) is a synthetic alanine/leucine/lysine-rich peptide (*14*). The vast
55 majority of CPPs are cationic (*1, 3, 6, 7*).

56 How CPPs enter cells is debated and not fully characterized at the molecular level
57 (reviewed in (*1-8*)). Due to this knowledge gap, it is difficult to ameliorate CPP cellular
58 entry and this slows down development of CPP-based interventions. Two main modes
59 of CPP entry have been described: endocytosis and direct translocation(*1-8*).
60 Endocytosed CPPs gain cytosolic access by escaping endosomes. Direct
61 translocation has been proposed to occur through transient pore formation or
62 membrane destabilization. Endocytosis and direct translocation are not mutually
63 exclusive. Several entry routes can be followed simultaneously by a given CPP in a
64 given cell line (*9, 10*).

65 Here, we used CRISPR/Cas9-screenings to identify proteins required for the cellular
66 uptake of CPPs. This approach identified three potassium channels as mandatory for
67 the direct translocation of CPPs into various cell types. Further, we highlighted the
68 requirement of an appropriate membrane potential to generate a 2 nm-wide water
69 pores through which CPP translocation occurred. This allowed the establishment of

70 protocols to rationally manipulate the transmembrane potential of cells to render them
71 more permeable to specific CPPs *in vitro* and *in vivo*.

72

73 **Results**

74 **TAT-RasGAP$_{317-326}$ enters cells via endocytosis and direct translocation, but only**
75 **direct translocation mediates its biological activity**

76 In the present work, we have used TAT-RasGAP$_{317-326}$ as a model compound to
77 investigate the molecular basis of CPP cellular uptake. This peptide is made up of the
78 CPP TAT$_{48-57}$ and a 10 amino-acid sequence derived from the SH3 domain of p120
79 RasGAP (*15*). TAT-RasGAP$_{317-326}$ sensitizes cancer cells to chemo-, radio- and
80 photodynamic therapies (*16-19*) and prevents cell migration and invasion (*20, 21*).
81 Some cancer cell lines, such as Raji (Burkitt's lymphoma), SKW6.4 (transformed B-
82 lymphocytes) and HeLa (cervix carcinoma), are directly killed by this peptide (*22*). To
83 characterize the mode of entry of TAT-RasGAP$_{317-326}$, Raji, SKW6.4 and HeLa cells
84 were incubated with a FITC-labelled version of the peptide and visualized over time.
85 Peptide-cell interaction and internalization occurred through the following pattern:
86 binding to the plasma membrane (Movie S1), uptake leading to vesicular staining
87 and/or diffuse cytoplasmic staining, and eventually cell death characterized by
88 membrane disruption (Fig. 1A-B, S1A and Movie S1). Only in a minority of Raji and
89 SKW6.4 cells, was the peptide found in vesicular structures (Fig. 1A-B). Most of the
90 cells acquired the peptide rapidly in their cytoplasm without any detectable presence
91 of labelled vesicles (Fig. 1A-B and Movie S1-2). Even though labelled vesicles might
92 be masked by the intense cytoplasmic staining (when present), resulting in an
93 underestimation of the percentage of cells with mixed staining, these results

94 nevertheless demonstrate that, quantitatively, the main mode of entry of TAT-
95 RasGAP$_{317-326}$ in Raji and SKW6.4 cell lines occurs via a non-vesicular direct plasma
96 membrane translocation mechanism. In HeLa cells, direct translocation and the
97 vesicular mode of entry appeared to occur equally frequently for TAT-RasGAP$_{317-326}$
98 (Fig. 1A-B and Movie S3). Direct translocation across the cell membrane often seemed
99 to originate from specific areas of the cells (Fig. S1B-C), suggesting discrete structures
100 on the plasma membrane involved in CPP entry. Laser illumination-induced damage
101 to cell integrity (*23-26*) was ruled out as a mechanism of fluorescent dye-labelled CPP
102 cellular uptake (Fig. S1D). Cells were able to concentrate the CPP in their cytoplasm
103 (Fig. S1E). TAT-RasGAP$_{317-326}$ uptake was found to be temperature-dependent (Fig.
104 S1F). The contribution of the peptide surface binding to the overall cell-associated
105 signal only accounted to about 20% (Fig. S1G-H); hence, the majority of the cell-
106 associated peptide signal comes from within cells. Despite the intensity difference, the
107 kinetics of appearance of the two populations with vesicular and diffuse cytoplasmic
108 staining was similar (Fig. 1C-D). There was an almost perfect correspondence
109 between i) the percentage of cells with low intensity peptide fluorescence and the
110 percentage of cells with vesicular staining (Fig. 1E), ii) the percentage of cells with high
111 intensity peptide fluorescence and the percentage of cells with diffuse staining (Fig.
112 1F). Cell death induced by TAT-RasGAP$_{317-326}$ was mostly recorded in cells from the
113 high-intensity fluorescent population (Fig. 1G), which can only be achieved through
114 direct translocation of the peptide through the cell membrane as cell death was not
115 seen in cells where only vesicular CPP entry had occurred. Hence, direct translocation
116 of the peptide into cells is what allows TAT-RasGAP$_{317-326}$ to kill HeLa cells. In Raji and
117 SKW6.4 cells incubated with TAT-RasGAP$_{317-326}$, only one fluorescence intensity peak
118 was observed at a given time point that progressively shifted towards higher

119 fluorescence intensities (Fig. 1H). As little vesicular staining was detected in Raji and
120 SKW6.4 cells incubated with TAT-RasGAP$_{317-326}$ (Fig. 1A-B), the peak seen in Fig. 1H
121 mostly corresponds to cells that have acquired the peptide through direct translocation.
122 As in HeLa cells therefore, it is the direct translocation of the peptide in Raji and
123 SKW6.4 cells that eventually induces their death. Together these results show that
124 even though two modes of entry can be used by TAT-RasGAP$_{317-326}$ to penetrate cells,
125 it is direct translocation that is necessary for its biological activity.

126

127 **Identification of potassium channels as mediators of the direct translocation of**
128 **CPPs into cells**

129 The mode of CPP cellular entry is currently debated and no molecular proteins have
130 been identified that regulate this process. Interaction with acid sphingomyelinase (*27*),
131 local membrane deformation (*28*), as well as calcium influxes (*29*) have been
132 suggested to play a role in CPP direct translocation into cells. To screen for genes that
133 control the uptake of CPPs, we performed a CRISPR/Cas9 screen using TAT-
134 RasGAP$_{317-326}$ as a selective agent (Fig. S2A). In Raji and SKW6.4 cell lines, among
135 the most highly significantly differentially modulated genes were specific potassium
136 channels or genes coding for proteins known to regulate such channels indirectly (e.g.
137 PIP5K1A (*30*)) (Fig. 2A and S2B). KCNQ5, identified in Raji cells, is a voltage-
138 dependent potassium channel. KCNN4 and KCNK5, identified in SKW6.4 cells, are
139 calcium-activated channels and belong to the two-pore (voltage-independent)
140 potassium channel family (*31*), respectively.

141 These potassium channels were pharmacologically or genetically inactivated (Fig. 2B
142 and S3A-C) to validate their involvement in TAT-RasGAP$_{317-326}$ cellular uptake and the

143 resulting death induction. The KCNQ family inhibitor, XE-991 (*32*), fully blocked peptide
144 uptake in Raji cells and protected them from the killing activity of the peptide (Fig. 2B).
145 Knocking out KCNQ5 (Fig. S3A) in these cells produced the same effect as XE-991
146 (Fig. 2B and S3D). SKW6.4 cells individually lacking KCNN4 or KCNK5 (Fig. S3B), or
147 SKW6.4 cells treated with TRAM-34, a KCNN4 inhibitor (*33, 34*) were impaired in their
148 ability to take up the peptide and were partially protected against its cytotoxic activity
149 (Fig. 2B and S3D). Inhibition of KCNN4 activity with TRAM-34 in KCNK5 knock-out
150 cells did not further protect the cells against TAT-RasGAP$_{317-326}$-induced death. In
151 HeLa cells, TRAM-34, but not XE-991, inhibited TAT-RasGAP$_{317-326}$ uptake and
152 subsequent death (Fig. 2B). Thus in HeLa cells KCNN4 channels participate in the
153 cellular uptake of the peptide. This was confirmed by knocking out KCNN4 in these
154 cells (Fig. 2B and S3C). Resistance to TAT-RasGAP$_{317-326}$-induced death in KCNQ5
155 knock-out Raji cells and KCNN4 knock-out SKW6.4 or HeLa cells was restored through
156 ectopic expression of the corresponding FLAG- or V5-tagged channels (Fig. S3E-F
157 and S4), ruling out off-target effects.

158 To determine if the identified potassium channels affected the biological activity of
159 TAT-RasGAP$_{317-326}$ once inside cells, incubation with the peptide was performed in the
160 presence of pyrene butyrate, a counter anion that, through electrostatic interaction with
161 arginine residues, and in the absence of serum, promotes quick and efficient
162 translocation of CPPs (*35*). As serum removal sensitized cells to TAT-RasGAP$_{317-326}$-
163 induced death (Fig. S5A), the peptide concentrations had to be adapted to perform the
164 experiments in the presence of pyrene butyrate (Fig. S5B). Pyrene butyrate was not
165 toxic at the concentrations used (Fig. S5C). Potassium channel knock-out Raji and
166 HeLa cells incubated with both pyrene butyrate and TAT-RasGAP$_{317-326}$ were no longer
167 resistant against the peptide-induced death (Fig. S5D). These results demonstrate that

168 specific potassium channels play a crucial role in the cellular entry of TAT-RasGAP$_{317-326}$ but that they are not involved in the killing activity of the peptide if it is already in cells.

171 We next determined whether vesicular uptake or direct translocation were affected in cells with impaired potassium channel activities. Compared to their respective wild-type controls, the percentage of cells with diffuse cytoplasmic location of FITC-TAT-RasGAP$_{317-326}$ was drastically diminished in KCNQ5 knock-out Raji cells (Fig. 2C) and in KCNN4 and KCNK5 knock-out SKW6.4 cells (Fig. S6A). The effect was similar in the case of KCNN4 knock-out HeLa cells, albeit to a lesser extent (Fig. S6B). This was mirrored by an increase in the percentage of knock-out cells with vesicular staining (Fig. 2C and S6A-B). To confirm that cytoplasmic peptide accumulation is due to direct translocation and not endosomal escape, FITC-TAT-RasGAP$_{317-326}$ uptake was quantitated over time in a condition where the peptide was allowed to enter cells by endocytosis but then removed from the medium. Figure S6C (left) shows that diffuse cytoplasmic uptake of the peptide occurred when the peptide was present in the medium (see also left panel of Movie S4). However, no significant increase in the cytoplasmic signal was observed in washed out cells containing peptide-labelled endosomes (Fig. S6C, middle and Movie S4, right panel). We could nevertheless detect an increase in cytoplasmic fluorescence when endosomal escape was induced by LLOME (*36*). This confirms that in live cell conditions the diffuse cytoplasmic CPP signal originates from direct translocation and not endosomal escape (Fig. S6C). The invalidation of potassium channels did not affect transferrin uptake into cells, substantiating the non-involvement of these channels in endocytosis pathways (Fig. S6D).

192 One possibility to explain the above-mentioned results is that the absence of potassium
193 channels prevents the peptide binding to cells. At a 20 μM concentration, TAT-
194 RasGAP$_{317-326}$ is readily taken up by wild-type Raji cells but not by KCNQ5 knock-out
195 cells. At this concentration, peptide binding was slightly lower in knock-out than in wild-
196 type cells (Fig. S6E). However, augmenting the peptide concentrations in the
197 extracellular medium of KCNQ5 knock-out cells to reach surface binding signals
198 equivalent or higher than what was obtained in wild-type cells incubated with a 20 μM
199 peptide concentration still did not result in peptide cellular uptake (Fig. S6E). These
200 data show that differences in peptide binding do not explain the inability of the knock-
201 out cells to take up the peptide.

202 We assessed whether the role of potassium channels in cellular uptake also applied
203 to TAT cargos other than RasGAP$_{317-326}$. TAT-PNA is an oligonucleotide covalently
204 bound to TAT, which can correct a splicing mutation within the luciferase-coding
205 sequence (*37, 38*). This can only occur if TAT-PNA reaches the cytosol. The luciferase
206 activity triggered by TAT-PNA was diminished in the presence of potassium channel
207 inhibitors and in potassium channel knock-out cell lines (Fig. S7A). Cytosolic access
208 of TAT-Cre, which can recombine a loxP-RFP-STOP-loxP-GFP (*39, 40*) gene
209 construct, was then assessed. Switch from red to green fluorescence occurs only when
210 TAT-Cre reaches the nucleus. This took place in wild-type Raji cells but not in the
211 KCNQ5 knock-out cells (Fig. S7B). We finally tested a clinical phase III therapeutic D-
212 JNKI1 compound (*1, 2*) used in the context of hearing loss and intraocular
213 inflammation. The uptake of this peptide was completely blocked in Raji cells lacking
214 KCNQ5 (Fig. S7C, left). D-JNKI1 uptake was also diminished in SKW6.4 cells lacking
215 KCNN4 and KCNK5 channels, as well as in HeLa cells lacking KCNN4 potassium
216 channel (Fig. S7C, middle and right panels). These data demonstrate that the absence

217 of specific potassium channels diminishes or even blocks the entry of various TAT-
218 bound cargos.

219

220 **Potassium channels maintain plasma membrane polarization that is required for**
221 **CPP entry into cells**

222 Potassium gradients are critically involved in setting the plasma membrane potential.
223 The potassium channels identified in the CRISPR/Cas9 screen could therefore control
224 cell membrane potential. Figure 3A shows that genetic disruption or pharmacological
225 inhibition of KCNQ5 in Raji cells led to an increase in their membrane potential
226 (from -26 mV to -15 mV, validated with electrophysiological recordings; see Fig. S8A).
227 In SKW6.4 and HeLa cells, plasma membrane potential measurement was much more
228 variable than in Raji cells. Nevertheless, a trend of increased membrane potential was
229 observed when KCNN4 or KCNK5 were invalidated genetically or pharmacologically
230 (Fig. 3A).

231 If the reason why invalidation of the KCNQ5, KCNN4, and KCNK5 potassium channels
232 inhibits TAT-RasGAP$_{317-326}$ cellular entry is cell depolarization, a similar response
233 should be obtained by chemically inducing membrane depolarization. Figure 3B shows
234 that depolarizing cells with gramicidin (*41*) (making non-specific 0.4 nm pores (*42*)
235 within cell membranes) or by increasing the extracellular concentration of potassium
236 (dissipating the potassium gradient) totally blocked peptide entry into the three studied
237 cell lines. Hence, cellular depolarization in itself inhibits TAT-RasGAP$_{317-326}$ cellular
238 uptake. Next, we determined whether hyperpolarization could reverse the inability of
239 potassium channel knock-out cells to take up TAT-RasGAP$_{317-326}$. Cells were either
240 incubated in the presence of valinomycin (*43*), which leads to formation of potassium-

241 like channels, or transfected with KCNJ2 channel that also provokes potassium efflux
242 and membrane hyperpolarization (*44*). Valinomycin was used in the absence of serum
243 as the latter is expected to interfere with the drug (*43*) but serum-removal did not affect
244 membrane potential (Fig. S8B). Figure 3B shows that in Raji cells, treatment with
245 valinomycin was able to hyperpolarize KCNQ5 knock-out cells to a plasma membrane
246 potential value similar to the one found in wild-type cells. This fully restored peptide
247 uptake in the KCNQ5 knock-out cells. Hyperpolarization in SKW6.4 and HeLa cells
248 was achieved through KCNJ2 ectopic expression. This reversed the poor capacity of
249 the KCNN4 and KCNK5 knock-out SKW6.4 cells, as well as KCNN4 knock-out HeLa
250 cells, to take up TAT-RasGAP$_{317-326}$ (Fig. 3B). Moreover, hyperpolarization increased
251 peptide uptake in wild-type cells (Fig. 3B). Altogether these results demonstrate that
252 uptake of TAT-RasGAP$_{317-326}$ in various cell lines can be manipulated through cellular
253 depolarization to block uptake and through hyperpolarization to increase it, confirming
254 earlier results obtained for R8 peptide in Jurkat cells (*45*).

255 Next, we assessed whether the entry of different classes of CPPs was also regulated
256 by the membrane potential. The most commonly used CPPs in biology and medicine,
257 TAT, nanomeric arginine peptide (R9), Penetratin, MAP, and Transportan were tested
258 in depolarized and hyperpolarized conditions. The cytoplasmic signal of these CPPs
259 in HeLa cells appeared to originate from both vesicular and diffuse cytoplasmic staining
260 (Fig. S8C-D). With the apparent exception of Transportan, depolarization led to
261 decreased uptake of all CPPs, while hyperpolarization favored their uptake (Fig. 3C).
262 Transportan, unlike other tested CPPs, enters cells predominantly through endocytosis
263 (Fig. S8C), which could explain the difference in response to membrane potential
264 modulation. Next, we assessed if modulating membrane potential through changes in
265 potassium concentrations in the extracellular medium (Fig. S8E) impacted the uptake.

266 Although the extent of the response varied from one CPP to another, the global
267 observation was that the more depolarized the cells are, the less able they are to take
268 up CPPs (Fig. 3D). CPP membrane binding was only minimally affected by
269 depolarization (Fig. S8F). The reason why depolarized cells do no take up CPPs is
270 therefore not a consequence of reduced CPP binding to cells. The plasma membrane
271 potential also controlled peptide uptake in non-transformed rat primary cortical neurons
272 (Fig. S8G). Together these results show that CPP uptake can be modulated *in vitro* by
273 varying the membrane potential of cells.

274 Extracellular pH might regulate CPP uptake (*46*). However, in our experimental
275 system, cellular uptake of TAT-RasGAP$_{317-326}$ was unaffected by varying the
276 extracellular pH, whether or not membrane potential modulators were used (Fig. S8H).

277

278 **Hyperpolarization favors the formation of ~2 nm-wide water pores used by CPP**
279 **to translocate into cells**

280 To further study the mechanism of CPP cellular entry through direct translocation, we
281 took advantage of coarse-grained molecular dynamics technique and MARTINI force
282 field (*47, 48*). Specifically, asymmetric multi-component physiological membrane (*49*)
283 was constructed and subjected to a constant electric field (Fig. S9A), following a widely
284 applied computational procedure (*50-58*). In our simulations we have used a
285 physiological plasma cell membrane-like composition (for both inner and outer leaflet)
286 while earlier studies have employed simpler membrane composition (*50, 59-63*). The
287 application of transmembrane potential triggered the following molecular events. First,
288 protrusions of a few water molecules, often as a single-file column, on either side of
289 the bilayer were observed (Fig. S9B and Movie S5). The protrusion then extended into

290 the bilayer interior and expanded at the base, forming a conical structure which
291 eventually bridged the membrane, leading to increased radius of the transmembrane
292 water pore up to ~2 nm (Fig. S9B and Movie S5). The process was finalized by
293 considerable reorientation of lipid head groups towards the membrane interior. Polar
294 lipid head groups migrated from the membrane-water interface (*51, 64-67*) to the
295 interior of the bilayer, stabilizing the water pore.

296 CPPs strongly increased the kinetics of water pore formation in plasma membranes
297 (Fig. S9C), indicating that they play an active role in the generation of water pores.
298 CPP entry decreased as the temperature in the simulations was lowered to 12°C (Fig.
299 S9D), consistent with the data obtained in cells (Fig. S1F). As the membrane potential
300 of cells was unaffected by temperature changes (Fig. S9E), the delayed water pore
301 formation at low temperature is therefore a likely consequence of altered physico-
302 chemical properties of membranes such as diminished fluidity (*68*).

303 We next performed Molecular Dynamics simulations in the presence or in the absence
304 of a membrane potential generated by setting an ion imbalance (*50, 69-71*) to
305 determine the behavior of CPPs and their potential ability to move across membranes
306 (Fig. S9F). Membrane hyperpolarization was achieved through a net charge difference
307 of 30 positive ions between the intracellular and extracellular space. This protocol
308 allowed us to observe water pore formation (Fig. 4A) and its closure dynamics, as the
309 hyperpolarization process was reversed by ion transport across the membrane,
310 leading to depolarization and resealing of the water pore (Fig. 4A). In the presence of
311 hyperpolarization, but not in its absence, CPP penetration and translocation through
312 the plasma membrane was observed for all the tested CPPs (Fig. 4A-B, Movie S6-7).
313 Previous observations reporting a role for the plasma membrane potential in CPP

314 penetration into or through bilipidic membranes (*50, 59-63*) support these findings.
315 However, note that translocation of single CPP molecules had not been observed
316 before the present work.

317 To evaluate the structural characteristics of the water pores triggered by CPPs *in vitro*,
318 cells were co-incubated with FITC-labelled CPPs and molecules of different sizes:
319 propidium iodide (PI), with a diameter of 0.8-1.5 nm (*72*), or 3 kDa, 10 kDa, and 40
320 kDa dextrans with diameters of 2.3 ±0.38 nm (*73*), 4.5 nm and 8.6 nm (size estimation
321 provided by Thermofisher), respectively. While PI efficiently co-entered cells with the
322 CPPs, there was only marginal co-entry of the dextrans (Fig. 4C and S10A-B). CPPs
323 did not bind to PI (Fig. S10C) and thus PI entry and accumulation within cells was not
324 the result of CPP carry over. The marginal co-entry of dextrans was inversely
325 correlated with their size (inset in the third panel of Fig. 4C). These data indicate that
326 water pores triggered by CPPs allow molecules up to ~2 nm to efficiently enter cells.
327 Molecules in the 2-5 nm diameter range can still use this entry route to a limited extent
328 (of note the Cre recombinase with a diameter of 5 nm, estimated from crystal structure
329 (NDB:PD0003), can translocate into cells when hooked to TAT; see Fig. S7B) but
330 molecules with larger diameters are mostly prevented to do so.

331 Despite identical net positive charges (Fig. S8D), K9 was less capable of translocating
332 into cells compared to R9 (Fig. 4C and S8C) (*74*). This may be due to the deprotonation
333 of K9 once in the plasma membrane (see discussion). However, in the limited cases
334 cells have taken up K9, PI co-entered as well (Fig. 4C). This indicates that K9 has a
335 reduced capacity compared to R9 to trigger water pore formation but when they do, PI
336 can efficiently translocate through the pores.

337 PI staining is commonly used to assess cell membrane integrity, frequently associated
338 with cell death (see for example Fig. 1G and 2B). This dye poorly fluoresces in solution
339 (Fig. S10D). However, the PI intensity values in dead permeabilized cells are several
340 orders of magnitude higher than those recorded after cell hyperpolarization (compare
341 the left and right panels of Fig. 4D). Cell viability was not affected by transient treatment
342 with the indicated CPPs, membrane potential modulating agents and PI (Fig. S10E).
343 These results indicate that water pore formation does not compromise cell survival.

344 Modelling experiments indicate that water pores are created in membranes subjected
345 to sufficiently high (absolute values) membrane potentials. We therefore tested
346 whether the mere hyperpolarization of cells (i.e. in the absence of CPPs) could trigger
347 the translocation of PI into cells, indicative of water pore formation. Figure 4D (left)
348 shows that the hyperpolarizing drug valinomycin significantly increased PI cell
349 permeability. In contrast, depolarization, mediated by gramicidin, reduced PI uptake
350 (Figure 4D, left). Cells incubated with CPPs took up PI to an even greater extent than
351 when cells were treated with valinomycin (Fig. 4D, left).

352 Figure 4E shows the correlation between cytoplasmic PI uptake and membrane
353 potential. Based on this correlation, we estimated the membrane potential of cells
354 incubated with a CPP to be in the order of -150 mV (Fig. 4F). In accordance with the
355 modelling experiments, these data indicate i) that water pore formation in cells is
356 favored by cell hyperpolarization and inhibited by depolarization and ii) that CPPs
357 themselves (*75, 76*) contribute to the establishment of a strong hyperpolarized plasma
358 membrane environment that we coin megapolarization.

359

360 **Hyperpolarization improves CPP uptake *in vivo***

361 We investigated whether it was possible to experimentally manipulate the membrane
362 potential to favor CPP uptake in *in vivo* situations. Systemic exposure of zebrafish
363 embryos to valinomycin led to cell hyperpolarization (Fig. S11A) and improved uptake
364 of a TAT-based CPP (Fig. S11A-B). This systemic treatment, while not acutely toxic,
365 halted development (Fig. S11C-E). However, local valinomycin injection did not affect
366 long-term viability (Fig. S11F) and efficiently increased CPP cellular uptake (Fig. 5A).
367 Subcutaneous injections of valinomycin in mice induced tissue hyperpolarization (Fig.
368 S11G) and boosted the CPP delivery in skin cells (Fig. 5B). These results demonstrate
369 that hyperpolarizing drugs can be used to ameliorate CPP uptake in animal tissues.

370

371 **Discussion**

372 Multiple models, mostly inferred from artificial experimental paradigms, have been
373 proposed in literature to explain CPP direct translocation. These include the formation
374 of pores made of CPPs for their own entry, the formation of inverted micelles in the
375 plasma membrane that translocate CPP, or diffusion of the CPPs across the plasma
376 membrane (*1, 3-5, 8*). Our simulation and cellular data, while providing no evidence for
377 such models, demonstrate that CPP cellular uptake is potassium channel- and
378 membrane potential-dependent *in vitro* and *in vivo*. Potassium channels are required
379 to establish a basal low V_m, subsequently permissive for CPP direct translocation.
380 Hyperpolarizing drugs, such as valinomycin, enhance permissiveness. When CPPs
381 come into contact with the plasma membrane, they decrease even more the
382 membrane potential, resulting in a local megapolarized membrane. This increases
383 dramatically the likelihood of formation of water pores that the CPPs then use to
384 penetrate cells according to their electrochemical gradient (Fig. S12). Water pores are

385 created by a combination of lipid head group reorientation coupled to intrusion of a
386 column of water in the membrane bilayer. Water movement plays therefore an active
387 role in the formation of the pore and is not merely occurring once the pores are formed.
388 The movement of the positive charges carried by the CPPs into the cell dissipates the
389 V_m, resulting in the collapse of the water pores and sealing of the plasma membrane.
390 CPP-mediated formation of water pores is therefore transient and does not affect cell
391 viability. Multiple rounds of CPP-driven water pore formation and CPP translocation
392 into cells can lead to intracellular accumulation of the CPP to concentrations higher
393 than found outside cells (Fig. S1E).

394 Our model posits that the number of positively charged amino acids influence the ability
395 of CPPs to hyperpolarize cells and hence to form water pores that they take to
396 translocate into cells. There is indeed a good correlation in the simulation experiments
397 between the net positive charge of a CPP and the speed at which it triggers the
398 formation of a water pore (Fig. S9C). CPP hydropathy strongly correlates with
399 penetration of water molecules in the lipid bilayer, thus supporting the hypothesis that
400 the amount of water each CPP can route inside the membrane is modulated by the
401 hydrophobic and hydrophilic character of the peptide (*77*). The nature of cationic
402 amino acids in peptides determines their translocation abilities. It is known for example
403 that peptides made of 9 lysines (K9) poorly enter cells (Fig. 4C and S1I) and replacing
404 arginine by lysine in Penetratin significantly diminishes its uptake(*74, 78*). According to
405 our model, K9 should induce mega hyperpolarization, formation of water pores that
406 should then allow their translocation into cells. However, it has been determined that,
407 once embedded into membranes, lysine residues have a tendency to loose protons(*79,*
408 *80*). This will thus dissipate the strong membrane potential required for the formation
409 of water pores and leave the lysine-containing CPPs stuck with the phospholipids of

410 the membrane. In contrast, arginine residues are not deprotonated in membranes and
411 water pores can therefore be maintained allowing the arginine-rich CPPs to be taken
412 up by cells. CPPs can also enter cells through endocytosis, a mode of entry that is not
413 inhibited by cell depolarization (Fig. S6). The differences between CPPs in terms of
414 how efficiently uptake is modulated by membrane potential (Fig. 3C-D) could be
415 explained by how much they rely on direct translocation or endocytosis to penetrate
416 cells. The more positively charged a CPP is, the more it will enter cells through direct
417 translocation and consequently the more sensitive it will be to cell depolarization (Fig.
418 3C-D). On the other hand, when endocytosis is the predominant type of entry, CPP
419 uptake will be less affected by both hyperpolarization and depolarization, which has
420 been observed for Transportan.

421 We propose, based on the work described here, that hyperpolarization induced by
422 drugs such as valinomycin represents a simple alternative or parallel approach to
423 optimize CPP uptake. However hyperpolarizing drugs may be toxic when systemically
424 applied. For example, valinomycin at the concentrations used to induce
425 hyperpolarization (10 μM) would be lethal if systemically injected in mice (LD50 in the
426 low micromolar (*81*)). On the other hand, local administration of valinomycin is far less
427 toxic (*82, 83*) as confirmed here in zebrafish and mice. Hyperpolarizing agents may
428 therefore be preferentially used for local or topical applications, which is incidentally
429 the case for the clinically approved CPPs (*1, 2*).

430 Strategies to improve CPP delivery are becoming increasingly complex through the
431 use of nanoparticles (*84*), double-coated nanoparticles (*85*), liposome-polycation-DNA
432 complexes (*86*), branched peptides (*87*), etc. Our data provides a characterization at
433 molecular level that can be taken advantage of to i) improve or optimize old CPPs, ii)

434 design new CPPs, or iii) help explain the behaviors of newly discovered CPPs (*88-90*).
435 The present work indicates that the impact on megapolarization should be evaluated
436 when chemical modifications are performed on cationic CPPs to augment their delivery
437 capacities.

Author contributions

Conception and design of study: ET, GG, MH, NC, AD and CW

Acquisition of data: ET, GG, MH, NC, GD, YA, MS, SM and FO

Analysis and/or interpretation of data: ET, GG, MH, NC, MAD, MS, SM, GV, FO, JP, FA, AL, AD and CW

Funding acquisition: CW, NC and FA.

Resources: CW and FA

Drafting the manuscript: ET, GG and CW

Revising the manuscript and approval of the submitted version: all authors

Acknowledgements

The lab of CW is supported by grants from the Swiss National Science Foundation (n° CRSII3_154420, IZCSZ0-174639 and 158116, awarded to CW and NC respectively). The zebrafish work performed in the lab of FA was supported the Swiss National Science Foundation (n° 320030_170062, to FA). We are thankful to Prof. Denise Nardelli Haefliger and her group, especially to Sonia Domingos Pereira and Laurent Derre for helpful discussions. We are thankful to the Cellular Imaging Facility, Mouse Pathology Facility and Genomic Technologies Facility at the University of Lausanne for the resources provided and their technical help. We would like to thank Giacomo Nanni, for his technical help in running the molecular simulations. We are also thankful to the Swiss National Supercomputing Centre (CSCS).

Competing interests

Author declare no competing financial and non-financial interests.

462 ## Figure legends

463

464 **Fig. 1. TAT-RasGAP$_{317-326}$ enters cells via endocytosis and direct translocation,**
465 **but only direct translocation mediates its biological activity.**
466 **(A)** Depiction of the different modes of CPP entry into cells. Confocal microscopy was
467 performed on cells incubated for one hour with 40 μM (Raji and SKW6.4) and 80 μM
468 (HeLa) FITC-TAT-RasGAP$_{317-326}$ in RPMI with 10% FBS. Cells were washed with PBS
469 prior to visualization. Vesicular staining is indicative of CPP endocytosis while diffuse
470 staining is a consequence of CPP direct translocation into cells. Scale bar: 10 μm.
471 **(B)** Quantitation of staining types in function of time (FITC-TAT-RasGAP$_{317-326}$
472 continually present in the media). Types of staining were visually quantitated (n>150
473 cells per condition). Results correspond to the average of three independent
474 experiments.
475 **(C)** Representative flow cytometry histogram of HeLa cells incubated with 80 μM FITC-
476 TAT-RasGAP$_{317-326}$ in RPMI, 10% FBS for 60 minutes. The dotted line represents
477 cellular auto-fluorescence.
478 **(D)** Variation over time of the low and high intensity peak values. Peptide uptake was
479 assessed by flow cytometry. The results correspond to three independent experiments.
480 **(E)** Quantitation of the pattern of appearance of cells with low intensity peptide
481 fluorescence and vesicular staining. Peptide uptake was assessed by flow cytometry.
482 The percentage of cells with low and high CPP fluorescence was visually quantitated
483 (n>150 cells per condition). The results correspond to three independent experiments.
484 **(F)** Quantitation of the pattern of appearance of cells with high intensity peptide
485 fluorescence and diffuse staining. Peptide uptake was assessed by flow cytometry.
486 The percentage of cells with low and high CPP fluorescence was visually quantitated
487 (n>150 cells per condition). The results correspond to three independent experiments.
488 **(G)** Kinetics of FITC-TAT-RasGAP$_{317-326}$-induced death in the two populations
489 described in panel D. Cell death was assessed by propidium iodide (PI) staining. The
490 results correspond to one of three independent experiments.
491 **(H)** Representative flow cytometry histograms of Raji (left) or SKW6.4 (right) cells
492 incubated with 40 μM FITC-TAT-RasGAP$_{317-326}$ for different period of time. The results
493 correspond to one of three independent experiments.

494

495 **Fig. 2. Identification of potassium channels as mediators of direct translocation**
496 **of CPPs into cells.**
497 **(A)** Identification of genes implicated in TAT-RasGAP$_{317-326}$ uptake in Raji cells (upper
498 panel) and SKW6.4 cells (lower panel). The graphs depict the p-value (calculated using
499 the MAGeCK procedure; see Materials and Methods) for the difference in sgRNA
500 expression between peptide-treated and control cells for the ~20'000 genes targeted
501 by the CRISPR/Cas9 library.
502 **(B)** Quantitation of TAT-RasGAP$_{317-326}$ entry (top), and induced death (bottom) in wild-
503 type (WT) and knock-out (KO) cells. The WT and the corresponding potassium channel
504 KO versions of the indicated cell lines were pretreated or not for 30 minutes with XE-
505 991 or with TRAM-34 and then incubated (still in the presence of the inhibitors when
506 initially added) with, or without 40 μM (Raji and SKW6.4 cells) or 80 μM (HeLa cells)
507 TAT-RasGAP$_{317-326}$. Uptake was recorded after one hour and cell death after 16 hours
508 (Raji and SKW6.4) or 24 hours (HeLa). Results correspond to the average of three
509 independent experiments.
510 **(C)** Quantitation of the modalities of TAT-RasGAP$_{317-326}$ entry in wild-type and KCNQ5
511 knock-out Raji cells. Cells were incubated with FITC-TAT-RasGAP$_{317-326}$ for various
512 periods of time and peptide staining was visually quantitated on confocal images
513 (n>150 cells for each time-point). The increased percentage of cells with vesicular
514 staining in the KO cells is likely the result of unmasking from the disappearance of
515 strong diffuse staining. The results correspond to the average of three experiments.
516
517 **Fig. 3. Potassium channels maintain plasma membrane polarization that is**
518 **required for CPP entry into cells.**
519 **(A)** Assessment of the resting plasma membrane potential in the indicated cell lines
520 and the corresponding potassium channel knock-out (KO) clones in the presence or in
521 the absence of XE-991 or TRAM-34. The grey and white zones correspond to non-
522 treated cells and inhibitor-treated cells, respectively. NT, not treated. The p-values
523 correspond to the assessment of the significance of the differences with the control
524 wild-type condition using ANOVA multiple comparison analysis. Each dot in a given
525 condition represents an independent experiment.
526

527 **(B)** Effect of cellular depolarization (left of the grey zone) and hyperpolarization (right
528 of the grey zone) on peptide uptake. The indicated cell lines and the corresponding
529 channel knock-out (KO) clones were pretreated or not with depolarization agents (2
530 μg/ml gramicidin for 5 minutes or high extracellular potassium buffer for 30 minutes) or
531 with hyperpolarization inducer (10 μM valinomycin), followed by the addition of TAT-
532 RasGAP$_{317-326}$ for one hour. Alternatively, hyperpolarization was achieved by ectopic
533 expression of the KCNJ2 potassium channel. Membrane potential and peptide uptake
534 were then determined. The p-values correspond to the assessment of the significance
535 of the differences with the control wild-type condition using ANOVA multiple
536 comparison analysis. Each dot in a given condition represents an independent
537 experiment.
538 **(C)** Quantitation of CPP uptake in Raji cells by flow cytometry in depolarizing (top) or
539 hyperpolarizing (bottom) conditions. Data from a given independent experiment are
540 connected by lines. Comparison between two conditions was done using two-tailed
541 paired t-test.
542 **(D)** Uptake of various CPPs in the presence of different concentrations of potassium
543 chloride in the media. The thick grey lines correspond to the average of 3-5
544 independent experiments. Data for a given experiment are linked with thin blue lines.
545
546 **Fig. 4. Hyperpolarization favors the formation of ~2 nm-wide water pores used**
547 **by CPP to translocate into cells.**
548 **(A)** Visualization of *in silico* modelled, time dependent, TAT-RasGAP$_{317-326}$ penetration
549 and subsequent translocation across cellular membrane through a water pore. Water
550 molecules within membranes are depicted by red spheres (and by red dots outside the
551 membrane).
552 **(B)** Quantitation of CPP localization in hyperpolarized or depolarized conditions based
553 on coarse-grained molecular dynamics simulations. Membrane hyperpolarization was
554 achieved through a net charge difference of 30 positive ions between intracellular and
555 extracellular space in a double bilayer system (*50, 69-71*) obtaining a transmembrane
556 potential of 2.2 V.
557 **(C)** Quantitation of the percentage of cells with cytoplasmic staining after the indicated
558 treatment. The indicated compounds (32 μg/ml PI, 200 μg/ml dextran, 40 μM CPP,
559 except MAP, which was used at 20 μM) were incubated for 30 minutes on HeLa cells.

560 Depolarization was induced with 2 μg/ml gramicidin. The percentage of cells displaying
561 cytoplasmic uptake of the indicated molecules was then determined on confocal
562 images (n>200 cells; see Fig. S10B). Inset corresponds to an enlargement of the
563 percentage of cells positive for dextran in the presence of R9. The results correspond
564 to at least three independent experiments.
565 **(D)** Left: quantitation of PI uptake in wild type HeLa cells after 30 minutes of incubation
566 in normal, depolarizing (2 μg/ml gramicidin) or hyperpolarizing (10 μM valinomycin)
567 conditions in the presence or in the absence of 40 μM FITC-R9. Cytoplasmic uptake
568 was quantitated from confocal images using ImageJ (n>300 cells; see the methods).
569 Right: as in left panel, but using lower laser power to avoid saturation of the signal
570 obtained in saponin permeabilized cells. The p-values correspond to the assessment
571 of the significance of the differences with the not treated (NT) control condition using
572 ANOVA multiple comparison analysis. The results correspond to three independent
573 experiments.
574 **(E)** Relation between cytoplasmic PI uptake and membrane potential measured with
575 DiBac4(3) in HeLa cells. Each dot represents an independent experiment.
576 **(F)** The relation between PI uptake and membrane potential from panel E, was used
577 to calculate membrane potential based on PI fluorescence in HeLa cells. Each dot in
578 a given condition represents an independent experiment.
579
580 **Fig. 5.**
581 **Hyperpolarization improves CPP uptake *in vivo.***
582 **(A)** Assessment of CPP *in vivo* uptake in zebrafish embryos in normal and
583 hyperpolarized conditions. Forty-eight hour post fertilization, zebrafish embryos were
584 injected with 3.12 μM FITC-TAT-RasGAP$_{317-326}$(W317A) with or without 10 μM
585 valinomycin. Scale bar: 200 μm. Comparison between conditions in the presence or in
586 the absence of valinomycin was done using two-tailed paired t-test. The results
587 correspond to three independent experiments.
588 **(B)** Assessment of CPP *in vivo* uptake in C57BL/6N mice in normal and hyperpolarized
589 conditions. Mice were injected with 5 μM FITC-TAT-RasGAP$_{317-326}$(W317A) with or
590 without 10 μM valinomycin (n=11 injections per condition). Comparison between
591 conditions in the presence or in the absence of valinomycin was done using two-tailed
592 paired t-test.

593

594 **Fig. S1. Related to Fig. 1. Characteristics of CPP uptake.**

595 **(A)** Visual attribution of the various types of staining associated with FITC-CPP uptake
596 in wild-type Hela cells. Cells 1-4 display diffuse cytoplasmic staining; cells 5-9 mixed
597 staining of both vesicular and diffuse; cells 10-15 have acquired FITC-TAT-RasGAP$_{317-}$
598 $_{326}$ in vesicles. Scale bar: 20 μm.

599 **(B)** Representative confocal images of focal and homogenous entry of FITC-TAT-
600 RasGAP$_{317-326}$ direct translocation patterns in HeLa cells.

601 **(C)** Quantitation in Raji and HeLa cells of the patterns described in panel B. An
602 apparent homogenous type of entry could be focal if the entry point is outside of the
603 confocal plane. Focal diffusion is likely therefore to be underestimated. The results
604 correspond to three independent experiments.

605 **(D)** Quantitation of the cytosolic fluorescence intensity (left) and the percentage of cells
606 with cytosolic fluorescence (right). HeLa cells were incubated with 80 μM FITC-TAT-
607 RasGAP$_{317-326}$ for 30 minutes with the indicated frequency of laser exposures (n>130
608 cells per condition). FITC-TAT-RasGAP$_{317-326}$ translocation into cells occurred similarly
609 after 30 minutes whether the cells were illuminated once or 60 times over the 30
610 minutes period. Even if one argues that one illumination is sufficient to cause the
611 uptake seen after a 30 minute incubation period with CPP, then the uptake should be
612 the same whether the illumination is performed at 1 minute or at 30 minutes. This is
613 not what is observed: the uptake of the FITC-labelled CPP increases overtime
614 independently of the number of times the cells are illuminated. The results correspond
615 to three independent experiments.

616 **(E)** Quantitation of FITC-TAT-RasGAP$_{317-326}$ fluorescence within cells that had
617 acquired CPPs through direct translocation. The dotted line represents the
618 fluorescence in the cell culture media (i.e. outside of the cells).

619 **(F)** Quantitation of FITC-TAT-RasGAP$_{317-326}$ uptake at the indicated temperatures.
620 Cells were incubated on a thermoblock for one hour. Peptide uptake was measured by
621 flow cytometry. The results for each cell line correspond to three independent
622 experiments. The data was normalized to the fluorescence at 37°C.

623 **(G)** Quantitation, in the absence of cells, of the emitted FITC fluorescence at 525 nm
624 (excitation at 488 nm) of FITC-TAT-RasGAP$_{317-326}$ at indicated concentrations in PBS

625 in the presence or in the absence of 0.2% trypan blue. Fluorescence was recorded in
626 96 well plates using a CYTATION3 apparatus.
627 **(H)** Assessment of the contribution of surface bound FITC-TAT-RasGAP$_{317-326}$ to
628 overall cell-acquired fluorescence. HeLa cells were incubated with FITC-TAT-
629 RasGAP$_{317-326}$ for 60 minutes in 24 well plates in 0.5 ml RPMI, 10% FBS. Then, cells
630 were washed once with PBS (1 ml), trypsinized, and resuspended in 0.5 ml PBS
631 containing or not 0.2% trypan blue. Cell-associated fluorescence was recorded by flow
632 cytometry. Data were normalized to the fluorescence values of cells incubated with
633 FITC-TAT-RasGAP$_{317-326}$ in the absence of trypan blue. The results correspond to the
634 average of three independent experiments.
635
636 **Fig. S2. Related to Fig. 2. CRISPR/Cas9 screen and target gene identification.**
637 **(A)** Scheme of the CRISPR/Cas9 screening strategy to identify genes involved in TAT-
638 RasGAP$_{317-326}$ cellular entry. Raji and SKW6.4 cells were infected with a single guide
639 RNA (sgRNA) CRISPR/Cas9 lentiviral library in conditions favoring the expression of
640 only one specific sgRNA per cell (which is indicated by differentially colored cells). The
641 infected cells were then incubated in the presence or in the absence of 40 μM TAT-
642 RasGAP$_{317-326}$ for 8 days (Raji) or 17 days (SKW6.4). The expression of sgRNAs in
643 both populations was assessed by massive parallel sequencing to determine the
644 enrichment or depletion in specific sgRNAs in the peptide-treated population.
645 **(B)** Scatter-plot depicting the changes in sgRNA expression between the control and
646 treated cell populations. The most significantly modulated sgRNA sets are color-coded.
647
648 **Fig. S3. Related to Fig. 2. Validation of genes involved in the TAT-RasGAP$_{317-326}$**
649 **uptake identified through CRISPR/Cas9 screening.**
650 **(A-C)** Sequencing of the regions targeted by the sgRNAs disrupting KCNQ5, KCNK5
651 and KCNN4 potassium channels in Raji (panel A), SKW6.4 (panel B) or HeLa cells
652 (panel C). Mutations, insertions and deletions induced by the CRISPR/Cas9 system
653 are shown in red. Except the cases mentioned below, these mutations induce a frame
654 shift and early termination of the open reading frame. The sequences targeted by the
655 sgRNAs are highlighted in yellow. The sgRNA-induced mutations in the first allele of
656 clone Q5-2, in the first allele of SKW6.4 cells clone N4-2, and in the first allele of clone
657 K5-2 do not induce a frame-shift but are located in critical domains necessary for

658 potassium channel activity, such as the pore-forming region of KCNK5 (uniprot
659 accession number:O95279), region adjacent to the pore of KCNQ5 (uniprot accession
660 number: Q9NR82) or calcium recognition domain of KCNN4 (uniprot accession
661 number: O15554). Hence, these alleles presumably encode non-functional channels.
662 Clones Q5-1 in Raji, N4-1 and K5-1 in SKW6.4, and N4-1 in HeLa cells were those
663 that were used in subsequent experiments. The blue nucleotides correspond to silent
664 changes, aimed at reducing sgRNA-targeting, introduced in the KCNQ5-encoding
665 lentiviral vector (see panel E). PAM (protospacer adjacent motif) sequences are
666 italicized.
667 **(D)** The indicated wild-type (WT) and knock-out (KO) cells were tested for their ability
668 to be killed by TAT-RasGAP$_{317-326}$. Cell death was assessed after 16 hours. The results
669 correspond to the average of three independent experiments.
670 **(E)** Wild-type or KCNQ5 knock-out Raji cells were infected or not with a sgRNA-
671 resistant FLAG-KCNQ5-encoding lentivirus and treated with 40μTAT-RasGAP$_{317-326}$
672 for 16 hours. The results correspond to three independent experiments. Expression of
673 FLAG-KCNQ5 construct was detected by western blot using an anti-FLAG antibody.
674 **(F)** KCNN4 knock-out (KO) SKW6.4 and HeLa cells were infected or not with a KCNN4-
675 expressing lentivirus and then treated with TAT-RasGAP$_{317-326}$ for 16 hours (SKW6.4)
676 or 24 hours (HeLa). Expression of KCNN4-V5 construct was detected by western blot
677 using an anti-V5 antibody. Note that the Raji, SKW6.4 and HeLa knock-out cell lines
678 still express Cas9 and the sgRNAs targeting the potassium channels. Hence, the
679 ectopically expressed wild-type channel-encoding cDNAs can be targeted by the
680 CRISPR/Cas9 system but this nevertheless allows for a detectable expression of the
681 FLAG- or V5-tagged constructs although to much lower levels than in similarly infected
682 wild-type cells lacking Cas9 and sgRNAs (see Fig. S4). In Raji cells, the re-expressed
683 KCNQ5 channel contained 5 silent changes in the sgRNA recognition site (see panel
684 A) but this proved insufficient to allow for a strong ectopic expression (see Fig. S4A,
685 last two lanes). Cell death was assessed by flow cytometry of PI-stained cells.
686 The results correspond to the average of three independent experiments.
687
688 **Fig. S4. Related to Fig. 2 and S3. Uncropped western blots assessing the**
689 **expression of tagged potassium channels through lentiviral expression.**

690 **(A)** Wild-type and KCNQ5 knock-out Raji cells infected or not with FLAG-tagged
691 KCNQ5.
692 **(B)** Wild-type and KCNN4 knock-out SKW6.4 cells infected or not with V5-tagged
693 KCNN4.
694 **(C)** Wild-type and KCNN4 knock-out HeLa cells infected or not with V5-tagged KCNN4.
695 Dotted line corresponds to the cropped images shown in Fig. S3E-F.
696
697 **Fig. S5. Related to Fig. 2. Potassium channels modulate TAT-RasGAP$_{317-326}$**
698 **entry, but not the peptide-induced death.**
699 **(A)** Quantitation of concentration-dependent TAT-RasGAP$_{317-326}$ induced death in Raji,
700 SKW6.4 and HeLa wild-type cells in the presence or in the absence of serum. The
701 results correspond to the median three independent experiments.
702 **(B)** Quantitation of wild-type (WT) and knock-out (KO) cell death after incubation for
703 16 hours (Raji and SKW6.4) or 24 hours (HeLa) in serum-free RPMI media in the
704 presence of increasing concentrations of TAT-RasGAP$_{317-326}$. Arrows indicate the
705 chosen peptide concentration for experiments performed in the absence of serum. The
706 results correspond to the median three independent experiments.
707 **(C)** Cell death assessment in wild-type (WT) and knock-out (KO) Raji and HeLa cells
708 incubated in RPMI without serum, treated (+ pyrene butyrate) or not (NT) with 50 μM
709 pyrene butyrate for the indicated periods of time. DMSO (0.25% vol:vol) was used as
710 a vehicle control for the condition in the absence of pyrene butyrate. The results
711 correspond to the median of three independent experiments. The scheme on the right
712 depicts the structure of pyrene butyrate and how the molecule interacts with arginine
713 residues found in CPPs.
714 **(D)** Assessment of peptide-induced death at different time points in pyrene butyrate-
715 treated cells lacking or not specific potassium channel. Cells were incubated with 5μM
716 (Raji) or 10 μM (HeLa) of TAT-RasGAP$_{317-326}$, pre-incubated or not with 50 μM pyrene
717 butyrate for 30 minutes (in RPMI without serum). The results correspond to the median
718 of three independent experiments.
719
720 **Fig. S6. Related to Fig. 2. Potassium channels modulate direct CPP**
721 **translocation, but not endocytosis.**

722 **(A)** Same as Fig. 2C, but for wild-type and KCNN4 and KCNK5 SKW6.4 knock-out
723 cells. The results correspond to the average of three independent experiments.
724 **(B)** As in panel A, but for wild-type and KCNN4 knock-out HeLa cells. The results
725 correspond to the average of three independent experiments.
726 **(C)** Quantitation of TAT-RasGAP$_{317-326}$ cytosolic access resulting from direct
727 translocation (left, n=19) and endosomal escape (middle, n=16 and right. n=22) in the
728 presence or in the absence of 1 mM LLOME, a endosome/lysosome disruptor(*36*). In
729 direct translocation condition, the peptide was continuously present in the media, while
730 it was washed out after 30 minutes to assess endosomal escape. LLOME was used to
731 show that our experimental setup allows for the detection of cytoplasmic CPPs if they
732 are released from cellular vesicles. The results correspond to three independent
733 experiments.
734 **(D)** Quantitation by flow cytometry of 20 μg/ml AlexaFluor488-transferrin uptake in the
735 wild-type (WT) cell lines and the corresponding knock-out (KO) cells, pretreated or not
736 for 30 minutes with the XE-991 (10 μM) or TRAM-34 (10 μM) potassium channel
737 inhibitors. Transferrin uptake was allowed to proceed for 60 minutes (still in the
738 presence of inhibitors when these were used in the 30 minute pre-incubation period).
739 To quench membrane bound transferrin fluorescence, cells were incubated with 0.2%
740 trypan blue prior to flow cytometry analysis (see Fig. S1F-G). The independent
741 experiment replicates are color-coded.
742 **(E)** Assessment of FITC-TAT-RasGAP$_{317-326}$ binding to cellular membrane of wild-type
743 and KCNQ5 knock-out Raji cells after 60 seconds of incubation (top), as well as
744 associated peptide uptake after one hour of treatment (bottom). The results correspond
745 to at least five independent experiments.
746
747 **Fig. S7. Related to Fig. 2. Potassium channels regulate the cellular uptake of**
748 **various TAT-bound cargos.**
749 **(A)** TAT-PNA-induced luciferase activity in the indicated cell lines pretreated or not with
750 potassium channel inhibitors (XE-991 or TRAM-34) or genetically invalidated for
751 specific potassium channels. Results are normalized to non-stimulated cells (dashed
752 lines). The independent experiment replicates are color-coded. The p-values
753 correspond to the assessment of the significance of the differences with the control
754 wild-type condition using ANOVA multiple comparison analysis.

755 **(B)** Representative microscopy images of wild-type and KCNQ5 knock-out Raji cells
756 expressing loxP-RFP-STOP-loxP-GFP and treated or not with 20 μM TAT-Cre for 48
757 hours. The results correspond to one of three independent experiments.
758 **(C)** Uptake of FITC-D-JNKI1 in the indicated cell lines genetically invalidated (KO) or
759 not (WT) for specific potassium channels. The results correspond to the median of
760 three independent experiments.
761
762 **Fig. S8. Related to Fig. 3. Membrane potential modulation and CPP uptake.**
763 **(A)** Membrane potential measurement validation. Membrane potential of wild-type and
764 KCNQ5 knockout (KO) Raji cells was measured using DiBac4(3), a fluorescent
765 membrane potential sensor, or by performing perforated patch electrophysiology
766 recordings. Each dot in the figures reporting DiBac4(3) measurements corresponds to
767 the median of 10'000 cell recording. For perforated patch, each dot in the figures
768 corresponds to the membrane potential of one cell.
769 **(B)** Membrane potential measurement in wild-type Raji cells performed in the presence
770 or in the absence of serum. Membrane potential was assessed using DiBac4(3).
771 **(C)** Confocal microscopy quantitation of HeLa cells displaying the indicated types of
772 CPP uptake. The CPPs (40 μM, except for MAP 20 μM) were continuously present in
773 the media during the course of the experiment. The results correspond to the average
774 of three independent experiments.
775 **(D)** Sequences of the indicated CPPs and their net charge. Positively charged amino
776 acids (arginine and lysine) are color-coded.
777 **(E)** Setting membrane potential by varying extracellular potassium concentrations.
778 Assessment of membrane potential changes in Raji cells incubated in RPMI medium
779 containing the indicated concentrations of potassium chloride (isotonicity was
780 maintained by adapting the sodium chloride concentrations; see methods). Membrane
781 potential was measured with DiBac4(3). The results correspond to the median of 4-6
782 independent experiments.
783 **(F)** Assessment of FITC-CPP binding to cellular membrane of wild-type Raji cells in
784 normal or depolarized conditions after 60 seconds of incubation (top), as well as
785 associated peptide uptake after one hour of treatment with CPP (bottom). Cells were
786 preincubated for 30 minutes in the presence of RPMI-media containing 5.2 or 91.9 mM
787 potassium chloride and then treated with 40 μM of the indicated CPPs. The results

788 correspond to at least six independent experiments. Comparison between non-treated
789 or depolarized conditions was done using two-tailed paired t-test.
790 **(G)** Assessment of membrane potential (top) and FITC-TAT-RasGAP$_{317-326}$ uptake
791 (bottom) in control, depolarized (TEA-treated), and hyperpolarized (valinomycin-
792 treated) primary rat cortical neurons. The results correspond to the median of at least
793 three independent experiments.
794 **(H)** Quantitation of TMR-labelled TAT-RasGAP$_{317-326}$ uptake in wild-type Raji cells at
795 the indicated pH in depolarizing and hyperpolarizing conditions. These experiments
796 were performed in the presence of 10% FBS as acidification or alkalization were toxic
797 for the cells. Inset corresponds to TMR-RasGAP$_{317-326}$ uptake in cells incubated in
798 media at physiological pH 7.5. Cells were preincubated in media at the indicated pH in
799 presence or in the absence of 2 μg/ml gramicidin or 10 μM valinomycin, prior to addition
800 of 40 μM TMR-TAT-RasGAP$_{317-326}$ for one hour. Points linked by lines correspond to
801 independent experiments.
802
803 **Fig. S9. Related to Fig. 4. Visualization of water pore formation within**
804 **physiological cellular membrane.**
805 **(A)** Visual inspection of the molecular systems to estimate the water pore formation
806 kinetics. The static electric field (E_{ext}) ha s been highlighted with a green arrow.
807 **(B)** Water pore formation within polarized physiological cell membrane and closure due
808 to ion movement and progressive depolarization.
809 **C)** Assessment of the time necessary for water pore formation in the presence or in
810 the absence of the indicated CPPs at 37°C based on *in silico* modeling experiments.
811 The Pearson correlation coefficients of the fitting curves are R_{R9}=0.85, $R_{Penetratin}$=0.95,
812 R_{MAP}=0.92, $R_{TATRasGAP}$=0.91, $R_{Transportant}$=0.80, R_{NoCPP}=0.87.
813 **(D)** Assessment of the time necessary for water pore formation in presence of R9 at
814 37°C and 12°C. The Pearson correlation coefficients of the fitting curves are R_{R9-37C}=0.85, and R_{R9-12C}=0.93.
816 **(E)** *In vitro* membrane potential measurement at the indicated temperatures in wild-
817 type Raji and SKW6.4 cells using DiBac4(3). The results correspond to the median of
818 three independent experiments.

819 **(F)** Schematic description of the double-bilayer molecular system. The localization of
820 the CPPs (extracellular, penetration, and translocation) has been defined based on the
821 distance between each CPP and the membrane. The CPP is highlighted in yellow.

822

823 **Fig. S10. Related to Fig. 4. Water pore formation in cells occurs in hyperpolarized**
824 **membranes and is promoted by CPPs.**
825 **(A)** Representative images related to Fig. 4C. Wild-type HeLa cells were incubated in
826 the presence of 32 μg/ml in the presence or in the absence of 40 μM FITC-R9, or left
827 untreated for 30 minutes at 37°C in RPMI with 10% FBS. Depolarization was induced
828 with 2 μg/ml gramicidin. Images were obtained by confocal microscopy. As shown
829 below in panel D, the fluorescence produced by 32 μg/ml of PI is under the threshold
830 of detection. Hence, when PI fluorescence is detected in cells (see the example in
831 panel A), the corresponding PI concentration is higher than 32 μg/ml (see panel D). In
832 other words, cellular PI fluorescence is detected in cells because the cells are able to
833 concentrate this cationic dye in their cytoplasm, as they are able to do with cationic
834 CPP (see Fig. S1D).
835 **(B)** An example of visual quantitation performed in Fig. 4C, based on images in panel
836 A of this figure in wild-type HeLa cells. The percentage of cells positive for PI and cells
837 that have acquired FITC-R9 through direct translocation, have been assessed as
838 follows. Cells 1, 3-7 are considered as positive for PI (left) and cells 1-6 are counted
839 as those where direct translocation has occurred (right). The rest of the cells were
840 considered as negative. Scale bar: 20 μm.
841 **(C)** PI does not interact with R9. The potential binding between PI (6 mM) and R9 (0.6
842 mM) at 37°C was assessed by isothermal titration calorimetry. Representative power
843 and heat of injection are shown. This experiment was repeated three times with similar
844 results.
845 **(D)** PI fluorescence detection in media in the absence of cells. Wells containing the
846 indicated PI concentrations in RPMI were illuminated using the same settings as in Fig.
847 4C and D (left). Fluorescence intensity within the full region of the obtained images
848 was quantitated using ImageJ. The arrow indicates the PI concentration used for water
849 pore-related experiments (32 μg/ml).
850 **(E)** Assessment of colony formation potential after transient CPP and membrane
851 potential treatments. DMSO was used as a vehicle for gramicidin and valinomycin.

852 Wild type HeLa cells were incubated for one hour with the indicated treatment, washed
853 and plated on 10 cm dishes. Number of colonies were counted at day 14 after Giemsa
854 staining.
855
856 **Fig. S11. Related to Fig. 5. Zebrafish and mouse membrane potential modulation.**
857 **(A)** Eighteen hours post fertilization zebrafish embryos were incubated 40 minutes with
858 the indicated concentrations of valinomycin with 950 nM DiBac4(3). DiBac4(3)
859 fluorescence was then recorded and normalized to the non-treated control. The
860 decrease in DiBac4(3) fluorescence indicates membrane hyperpolarization.
861 Membrane potential values could not be calculated, as a standard curve would have
862 to be performed in zebrafish. DiBac4(3) uptake was assessed from confocal images
863 of the fish tail region.
864 **(B)** Eighteen hours post fertilization zebrafish embryos were incubated with or without
865 3.12 μM TAT-RasGAP$_{317-326}$ (W317A), a mutant version that is not toxic to cells, in the
866 presence of the indicated concentrations of valinomycin. Peptide uptake was assessed
867 from confocal images of the fish tail region.
868 **(C-D)** Eighteen hours post fertilization zebrafish embryos were incubated 1 hour with
869 the indicated concentrations of valinomycin, in the absence (panel C) or in the
870 presence (panel D) of 3.12 μM TAT-RasGAP$_{317-326}$ (W317A), then washed, and
871 incubated in Egg water. The viability of each fish was assessed over 52 hours at the
872 indicated time points.
873 **(E)** Representative images of zebrafish treated as described in panel C and D, washed,
874 and further incubated in Egg water. Images were taken with a CYTATION3 apparatus
875 at a 4x magnification.
876 **(F)** Survival of 48 hours post fertilization zebrafish embryos following intramuscular
877 injection of 3.12 μM TAT-RasGAP$_{317-326}$ (W317A) peptide in the presence or in the
878 absence of 10 μM valinomycin. Survival was visually assessed under a binocular
879 microscope by taking into consideration the embryo transparency (as dead embryos
880 appear opaque), development characteristics and motility.
881 **(G)** Mice were intradermally injected with DiBac4(3) in the presence or in the absence
882 of 10 μM valinomycin. DiBac4(3) fluorescence was then recorded and normalized to
883 the mean of non-treated (NT) control. DiBac4(3) fluorescence was assessed as in
884 panel A.

885

886 **Fig. S12. Related to Fig. 3-5. Model of CPP direct translocation through water**
887 **pores.**

888 Cationic CPP translocation across cellular membranes is favored by the opening of
889 potassium channels or by hyperpolarizing drugs, such as valinomycin. This sets a
890 sufficiently low membrane potential permissive for CPP direct translocation. When
891 positively charged CPPs bind to the membrane, they induce megapolarization (i.e. a
892 membrane potential of about -150 mV). This leads to the formation of water pores that
893 are then used by CPPs to enter cells.

894

895 **Movie S1. Related to Fig. 1. TAT-RasGAP$_{317-326}$ uptake in Raji cells over a 16-hour**
896 **period.**

897 Representative time-lapse recording of wild-type Raji cells incubated with 5 μM TAT-
898 RasGAP$_{317-326}$ for 16 hours in RPMI in the absence of serum. For the first 30 minutes
899 of the recording, images were taken every 30 seconds, then until the end of the
900 recording, images were taken every five minutes. Peptide was present in the media
901 throughout the recording. Yellow and pink arrows indicate cells experiencing direct
902 translocation and endocytosis, respectively. Cyan arrows point towards labelled
903 endosomes and green asterisks to dead cells. Scale bar: 20 μM. Time is displayed in
904 hours:minutes.

905

906 **Movie S2. Related to Fig. 1. Early peptide entry in wild-type Raji cells.**

907 Time-lapse recording of Raji cells incubated with 40 μM TAT-RasGAP$_{317-326}$ for 30
908 minutes in RPMI, 10% FBS. Peptide was present in the media throughout the recording
909 and images were taken for 30 minutes at 10 second intervals. Scale bar: 10 μM. In this
910 Movie, only the central right cell acquires the peptide. Time is displayed in
911 minutes:seconds.

912

913 **Movie S3. Related to Fig. 1. Early peptide entry in wild-type HeLa cells**.

914 Time-lapse recording of HeLa cells incubated with 80 μM FITC-TAT-RasGAP$_{317-326}$ in
915 RPMI, 10% FBS. Yellow and pink arrows indicate cells experiencing direct
916 translocation and endocytosis, respectively. Images were taken for 30 minutes at 10
917 second intervals. Scale bar: 20 μM. Time is displayed in minutes:seconds.
918

919 **Movie S4. Related to Fig. 1 and S6C. Distinction between endosomal escape and**
920 **direct translocation.**
921 Wild-type HeLa cells were preincubated with 80 μM FITC-TAT-RasGAP$_{317-326}$ for 30
922 minutes in RPMI, 10% FBS and then imaged every 5 minutes for 4 hours at 37°C, 5%
923 CO_2. Movie on the left was recorded in the continuous presence of the peptide. Movie
924 on the right was recorded after the peptide was washed three times with RPMI, 10%
925 FBS. Scale bar: 10 μM. Time is displayed in hours:minutes.
926

927 **Movie S5. Related to Fig. 4. *In silico* visualization of water pore formation in the**
928 **presence of constant electrical field across a membrane bilayer.**
929 This Movie shows water pore formation in an asymmetric multi-component bilayer in
930 the presence of a membrane potential. This *in silico* simulation was performed with
931 externally applied electric field using molecular dynamics MARTINI coarse-grained
932 approach.
933

934 **Movie S6. Related to Fig. 4. *In silico* visualization water pore formation in the**
935 **presence of the indicated CPPs across a polarized membrane bilayer.**
936 This Movie shows the translocation of the indicated CPPs across a plasma membrane
937 in the presence of a membrane potential. This simulation was performed by molecular
938 dynamics MARTINI coarse-grained approach using an asymmetric multi-component
939 bilayer in the presence of ion-imbalance to polarize the membrane.

940

941 **Movie S7. Related to Fig. 4. *In silico* visualization water pore formation in the**
942 **presence of the indicated CPPs across a non-polarized membrane bilayer.**
943 This Movie shows the translocation of the indicated CPPs across a plasma membrane
944 in the absence of a membrane potential. This simulation was performed by molecular

dynamics MARTINI coarse-grained approach using an asymmetric multi-component bilayer in the absence of ion-imbalance.

948 ## Materials and Methods

949 ### Chemicals

950 Puromycin 10 mg/ml (Thermo Fisher, ref. no. A11138-02) was aliquoted and stored at
951 -20 °C. Blasticidin (Applichem, ref. no. A3784) was dissolved at 1 mg/mL in water and
952 stored at -20 °C. XE-991 and TRAM-34 (Alomone labs, ref. no. X-100 and T-105
953 respectively) was dissolved in DMSO at 100 mM and stored at -20 °C. Cells were
954 preincubated with 10 μM of these inhibitors for 30 minutes and then kept throughout
955 the experiments. Pyrene butyrate (Sigma, ref. no. 257354) was dissolved in DMSO at
956 20 mM and stored at -20 °C. Live Hoechst 33342 (Sigma, ref. no. CDS023389) was
957 aliquoted and stored at -20°C. Trypan Blue 0.4% (Life technologies, ref. no. 15250061)
958 was stored at room temperature. AlexaFluor488-labeled human transferrin was
959 dissolved in PBS 5 at mg/ml and stored at 4°C (Thermo Fisher, ref. no. 13342).
960 TexasRed-labelled neutral 3'000 and 40'000 Da dextran was dissolved in PBS at 10
961 mg/ml and stored at -20°C (Thermo Fisher, ref. no. D3329 and D1829, respectively).
962 TMR-labelled 10'000 neutral dextran was dissolved in PBS at 10 mg/ml and stored at
963 -20°C (Thermo Fisher, ref. no. D1816).

964

965 ### Antibodies

966 The rabbit polyclonal anti-V5 (Bethyl, ref. no. A190-A120), mouse monoclonal anti-
967 FLAG antibody was from Sigma-Aldrich (ref. no. F1804), rabbit monoclonal anti-actin
968 (Cell signaling, ref. no. 4970) and rat monoclonal anti-γ-tubulin (Santa Cruz, ref. no.
969 sc-51715) antibodies were used for Western blotting.

970

971 ### Cell lines

972 All cell lines were culture in 5 % CO_2 at 37°C. Raji (kind gift from the laboratory of
973 Aimable Nahimana, ATCC: CCL-86), SKW6.4 (kind gift from the laboratory of Pascal
974 Schneider, ATCC: TIB-215) and HeLa (ATCC: CCL-2) cells were cultured in RPMI
975 (Invitrogen, Cat# 61870) supplemented with 10 % heat-inactivated fetal bovine serum
976 (FBS; Invitrogen, Cat# 10270-106). All cell lines were authenticated via Microsynth cell
977 authentication service.
978

979 **Zebrafish**

980 Zebrafish (*Danio rerio*) from AB line were bred and maintained in our animal facility
981 under standard conditions (*91*), more specifically at 28.5°C and on a 14:10 hours
982 light:dark cycle at the Zebrafish facility of the School of Biology and Medicine (cantonal
983 veterinary approval VD-H21). Zebrafish of 20 hours post fertilization were collected
984 and treated with 0.2 mM phenylthiourea (PTU, Sigma, St. Louis, MO) to suppress
985 pigmentation. Embryos were raised at 28.5°C in Eggwater (0.3 g sea salt/L reverse
986 osmosis water) until the age of 4 days post fertilization.
987

988 **Mice**

989 C57BL/6NCrl were acquired from Charles River laboratories, which were then housed
990 and bred in our animal facility. All experiments were performed according to the
991 principles of laboratory animal care and Swiss legislation under ethical approval (Swiss
992 Animal Protection Ordinance; permit number VD3374.a).
993

994 **Primary cortical neuronal culture**

995 Sprague-Dawley rat pups (from Janvier, France) were euthanized in accordance with
996 the Swiss Laws for the protection of animals, and the procedures were approved by

997 the Vaud Cantonal Veterinary Office. Primary neuronal cultures from cortices of 2-day-
998 old rats were prepared and maintained at 37 °C with a 5% CO_2-containing atmosphere
999 in neurobasal medium (Life Technologies, 21103-049) supplemented with 2% B27
1000 (Invitrogen, 17504044), 0.5 mM glutamine (Sigma, G7513) and 100 µg/ml penicillin-
1001 streptomycin (Invitrogen, 15140122) as described previously (*92*). Neurons were
1002 plated at a density of ~3×10^5 cells on 12-mm glass coverslips coated with 0.01% poly-
1003 L-lysine (Sigma, P4832). Half of the medium was changed every 3-4 days and
1004 experiments were performed at 12–13 days *in vitro*.
1005
1006 **Confocal microscopy**
1007 Confocal microscopy experiments were done on live cells. Cells were seeded onto
1008 glass bottom culture dishes (MatTek, corporation Cat# P35G-1.5-14-C) and treated as
1009 described in the Fig.s. For nuclear staining, 10 µg/ml live Hoechst 33342 (Molecular
1010 probes, Cat# H21492) was added in the culture medium 5 minutes before washing
1011 cells twice with PBS. After washing, cells were examined with a plan Apochromat 63x
1012 oil immersion objective mounted on a Zeiss LSM 780 laser scanning fluorescence
1013 confocal microscope equipped with gallium arsenide phosphide detectors and three
1014 lasers (a 405 nm diode laser, a 458-476-488-514 nm argon laser, and a 561 nm diode-
1015 pumped solid state laser). Time-lapse experiments were done using an incubation
1016 chamber set at 37°C, 5% CO_2 and visualized with a Zeiss LSM710 Quasar laser
1017 scanning fluorescence confocal microscope equipped with either Neofluar 63x, 1.2
1018 numerical aperture (NA) or plan Neofluar 100x, 1.3 NA plan oil immersion objective
1019 (and the same lasers as above). Visual segregation of cells based on type of CPP
1020 entry, associated either with vesicular or diffuse staining, was performed as shown in
1021 Fig. S1A.

1022

1023 **Flow cytometry**

1024 Flow cytometry experiments were performed using a Beckman Coulter FC500
1025 instrument. Cells were centrifuged and resuspended in PBS prior to flow cytometry.
1026 Data analysis was done with Kaluza Version 1.3 software (Beckman Coulter).

1027

1028 **Cell death and CPP uptake measurements**

1029 With the exception of neurons, cell death was quantitated with 8 μg/ml propidium iodide
1030 (Sigma, Cat# 81845). Unless otherwise indicated, cell death was assessed after 16
1031 hours of continuous incubation in Raji and SKW6.4 cells and 24 hours in HeLa cells.
1032 Cell death and peptide uptake were analyzed by flow cytometry. Uptake
1033 measurements were done after one hour of incubation. Peptide uptake in primary
1034 cortical neurons was assessed by confocal microscopy with LSM780. Cell-associated
1035 fluorescence was quantitated with ImageJ.

1036

1037 **Lentivirus production**

1038 Recombinant lentiviruses were produced as described (*93, 94*) with the following
1039 modification: the envelope plasmid pMD.G and the packaging vector pCMVΔR8.91
1040 were replaced by pMD2.G and psPAX2, respectively.

1041

1042 **Membrane potential measurements *in vitro***

1043 Two methods were used to assess cellular membrane potential *in vitro*. With the first
1044 method, the membrane potential was determined by incubating the cells for 40 minutes
1045 with 100 nM of the fluorescent probe DiBAC4(3) (Thermofisher, Cat# B438) and the

1046 median fluorescence intensity was then assessed by flow cytometry. Calculation of the
1047 actual membrane potential in mV based on the DiBAC4(3) signals was performed as
1048 described earlier(*95, 96*). The second method relied on electrophysiology recordings.
1049 To perform these, the bath solution composition was (in mM): 103.9 NaCl, 23.9
1050 $NaHCO_3$, 2 $CaCl_2$, 1.2 $MgCl_2$, 5.2 KCl, 1.2 NaH_2PO_4, 2 glucose and 1.7 ascorbic acid.
1051 The pipet solution was composed of (in mM): 140 $KMeSO_4$, 10 HEPES, 10 KCl, 0.1
1052 EGTA, 10 phosphocreatine and 4 MgATP. The patch pipets had a resistance of 2.4-
1053 3.6 MΩ. Perforated patch recordings were performed as previously described (*97*).
1054 Briefly, freshly prepared gramicidin D (Sigma, Cat# G5002), at 2.8 μM final
1055 concentration, was added to prefiltered patch pipet solution and then sonicated for
1056 three consecutive times during 10 seconds. Cell-attached configuration was achieved
1057 by applying negative pressure on patch pipet until seal resistance of over one Giga
1058 Ohm was reached. After gaining cell access through gramicidin created pores,
1059 membrane potential measurements were done in current clamp at 0 pA for at least
1060 three minutes. Since primary rat neurons are killed following full depolarization induced
1061 by gramicidin, the standard curve from membrane potential calculations (*95, 96*) were
1062 performed using gramicidin-treated Raji cells incubated with increasing concentrations
1063 of DiBac4(3) for 40 minutes. Images of the cells were then taken using a LSM780
1064 confocal microscope and the cell-associated fluorescence quantitated with ImageJ.
1065

1066 **Relative membrane potential assessment *in vivo***

1067 Zebrafish embryos in Egg water (see Zebrafish section) were incubated for 40 minutes
1068 in the presence or in the absence of various concentrations of valinomycin together
1069 with 950 nM DiBac4(3). The embryos were then fixed and visualized under a confocal
1070 LSM710 microscope (*98*). DiBac4(3)-associated fluorescence of a region of interest of

1071 about 0.0125 mm^2 in the tail region was quantitated with ImageJ. The values were
1072 normalized to the control condition (i.e. in the absence of valinomycin). Mice were
1073 intradermally injected with 10 μl of a 950 nM DiBac4(3) PBS solution containing or not
1074 10 μM valinomycin and sacrificed one hour later. The skin was excised, fixed in 4%
1075 formalin, paraffin-embedded and used to prepare serial histological slices. Pictures of
1076 the slices were taken with a CYTATION3 apparatus. The DiBac4(3)-associated
1077 fluorescence in the whole slice was quantitated with ImageJ. The slice in the series of
1078 slices prepared from a given skin sample displaying the highest fluorescence signal
1079 was considered as the one nearest to the injection site. The signals from such slices
1080 are those reported in the Fig.s.
1081
1082 **Experimental modulation of the plasma membrane potential**
1083 Raji, SKW6.4 or HeLa cells: two hundred thousand cells were plated on non-coated
1084 plates to avoid cell adherence in 500 μl RPMI, 10% FBS. Cellular depolarization was
1085 induced by preincubating the cells at 37°C with 2 μg/ml gramicidin for 5 minutes and/or
1086 by placing them in potassium-rich buffer (*28*) for 30 minutes (40 mM KCl, 100 mM
1087 potassium glutamate, 1 mM $MgCl_2$, 1 mM $CaCl_2$, 5 mM glucose, 20 mM HEPES,
1088 pH7.4). Cells were then treated with 40 μM of the indicated CPPs for one hour when
1089 peptide uptake is recorded or with 100 nM DiBac4(3) for 40 minutes when membrane
1090 potential is to be measured. Hyperpolarization in Raji cells was performed by treating
1091 the cells with 10 μM valinomycin for 20 minutes in RPMI without serum. Cells were
1092 then treated with 5 μM of the indicated CPPs for one hour or 100 nM DiBac4(3) for 40
1093 minutes. In the case of SKW6.4 and HeLa cells, hyperpolarization was induced by
1094 infection with a viral construct expressing KCNJ2 (see “virus production” section). Cells

1095 were then treated with 40 μM of indicated CPP for one hour or 100 nM DiBac4(3) for
1096 40 minutes.
1097 Neurons (12 days post-isolation) were preincubated 30 minutes with 5 mM TEA
1098 (tetraethylammonium, Sigma Aldrich, Cat#T2265; gramicidin is toxic in these neurons;
1099 see section "Membrane potential measurements *in vitro*") to induce depolarization or
1100 10 μM valinomycin to induce hyperpolarization in bicarbonate-buffered saline solution
1101 (116 mM NaCl, 5.4 mM KCl, 0.8 mM $MgSO_4$, 1 mM NaH_2PO4, 26.2 mM NaHCO3,
1102 0.01 mM glycine, 1.8 mM CaCl2, 4.5 mg/mL glucose) in a 37°C, 5% CO_2 incubator.
1103 The cells were then incubated one hour with 2 μM of FITC-labeled TAT-RasGAP$_{317-}$
1104 $_{326}$. The cells were finally washed thrice with PBS and images were acquired using a
1105 LSM780 confocal microscope. Cell-associated peptide fluorescence was quantitated
1106 using ImageJ.
1107
1108 **Setting membrane potential by changing potassium concentrations in the media**
1109 RPMI-like media made without potassium chloride and without sodium chloride was
1110 from Biowest (Table S1). Varying concentrations of potassium chloride were added to
1111 this medium containing 10% FBS. Sodium chloride was also added so that the sum of
1112 potassium and sodium chloride equaled 119 mM (taking into account the
1113 concentrations of sodium and potassium in FBS). Cells were preincubated in the media
1114 containing different concentrations of potassium for 20 minutes, then different CPPs at
1115 a 40 μM concentration were added and cells were incubated for one hour at 37°C in
1116 5% CO_2. Cells were washed once in PBS and CPP uptake was measured by flow
1117 cytometry. The corresponding membrane potential was measured with DiBac4(3).
1118 **Table S1: Media composition**
1119

CAS Number	Components	Quantity in g/l

13477-34-4	Calcium Nitrate Tetrahydrate	0.10000000
7487-88-9	Magnesium Sulfate Anhydrous	0.04884000
50-99-7	D-Glucose Anhydrous	2.00000000
56-40-6	Glycine	0.01000000
39537-23-0	L-Alanyl-L-Glutamine	0.44600000
74-79-3	L-Arginine Free Base	0.20000000
70-47-3	L-Asparagine Anhydrous	0.05000000
56-84-8	L-Aspartic acid	0.02000000
30925-07-6	L-Cystine Dihydrochloride	0.06520000
56-86-0	L-Glutamic Acid	0.02000000
71-00-1	L-Histidine	0.01500000
51-35-4	L-Hydroxy-L-Proline	0.02000000
73-32-5	L-Isoleucine	0.05000000
61-90-5	L-Leucine	0.05000000
657-27-2	L-Lysine Monohydrochloride	0.04000000
63-68-3	L-Methionine	0.01500000
63-91-2	L-Phenylalanine	0.01500000
147-85-3	L-Proline	0.02000000
56-45-1	L-Serine	0.03000000
72-19-5	L-Threonine	0.02000000
73-22-3	L-Tryptophan	0.00500000
69847-45-6	L-Tyrosine Disodium Salt Dihydrate	0.02883000
72-18-4	L-Valine	0.02000000
67-48-1	Choline Chloride	0.00300000
58-85-5	D-Biotin	0.00020000
137-08-6	D-Ca Pantothenate	0.00025000
59-30-3	Folic Acid	0.00100000
87-89-8	Myo-Inositol	0.03500000
98-92-0	Nicotinamide (Nicotinic acid amide)	0.00100000
150-13-0	P-Aminobenzoic Acid (PABA)	0.00100000
58-56-0	Pyridoxine Hydrochloride	0.00100000
83-88-5	Riboflavin	0.00020000
67-03-8	Thiamine Hydrochloride	0.00100000
68-19-9	Vitamine B12	0.00000500
70-18-8	L-Glutathione Reduced	0.00100000
34487-61-1	Phenol Red Sodium Salt	0.00530000
WATER		996.66117500

In silico pore formation kinetics though MARTINI coarse-grained simulations

The water pore formation kinetics has been investigated in this study by applying a constant electrostatic potential to the molecular system (*50-58*). An asymmetric multi-component membrane was constructed and solvated using CHARMM-GUI (*99, 100*). Each layer contained 100 lipids (Table S2), in a previously described composition (*49*).

1126 The membrane was solvated with 13500 water molecules, obtaining a molecular
1127 system of 45000 particles. The MARTINI (*101, 102*) force field was used to define
1128 phospholipids' topology through a coarse-grained (CG) approach. The polarizable
1129 water model has been used to assess the water topology (*103*). The CPP models have
1130 been obtained by PEPFOLD-3 server (*104*) , as done in previous studies in the field
1131 (*77, 105*) . The elastic network ELNEDYN (*106*) has been applied to reproduce the
1132 structural and dynamic properties of the CPPs.

1133 **Table S2. Phospholipid composition considered in the present study**

	Inner membrane		**Outer membrane**	
type	Number of lipids	%	Number of lipids	%
POPC	18	18	39	39
POPE	27	27	6	6
PSM	10	10	21	21
POPS	11	11	-	-
POPI	5	5	-	-
CHOL	29	29	34	34
total	100	100	100	100

1134 For each molecular system, one CPP was positioned 3 nm far from the membrane
1135 outer leaflet, in the water environment corresponding to the extracellular space. Then,
1136 the system was equilibrated through four MD simulations of 100ps, 200ps, 500 ps, and
1137 100 ns under the NPT ensemble. Position restraints were applied during the first three
1138 molecular dynamics (MD) simulations and gradually removed, from 200 kJ/mol*nm^2 to
1139 10 kJ/mol*nm^2. Velocity rescaling (*107*) temperature coupling algorithm and time
1140 constant of 1.0 ps were applied to keep the temperature at 310.00 K. Berendsen (*108*)
1141 semi-isotropic pressure coupling algorithm with reference pressure equal to 1 bar and
1142 time constant 5.0 ps was employed. Then, all systems were simulated for the
1143 production run in the NPT ensemble with the time step of 20 fs. Electrostatic
1144 interactions were calculated by applying the particle-mesh Ewald (PME) (*109*) method
1145 and van der Waals interactions were defined within a cut-off of 1.2 nm. Periodic
1146 boundary conditions were applied in all directions. Trajectories were collected every

1147 10 ps and the Visual Molecular Dynamics (VMD) (*110*) package was employed to
1148 visually inspect the simulated systems. GROMACS 2018 was used for simulations and
1149 data analysis (*111*). The relatively small size of the molecular system and the
1150 application of Coarse-Grained Martini forcefield, allowed us to study the pore formation
1151 kinetics, requiring many simulations at varying field strengths. In detail, 25 simulations
1152 were performed for each molecular system at different external electric field strengths
1153 from 0.0055 V/nm to 0.090 V/nm. In the MD simulations, an external electric field E_{ext}
1154 was applied parallel to the membrane normal *z*, i.e., perpendicular to the bilayer
1155 surface. This was achieved by including additional forces $F_i = q*E_{ext}$ acting on all
1156 charged particles *i.* All the MD simulations were performed until the water pore
1157 formation event was observed. In order to determine the effective electric field in
1158 simulations, we applied a computational procedure reported in literature, that has
1159 demonstrated to provide computational estimation of water pore formation kinetics in
1160 line with experimental results (*53*). It is worth mentioning that molecular simulations
1161 have been performed to elucidate the impact of CPPs' physico-chemical properties on
1162 the pore formation kinetics, as this will have a more general meaning than the absolute
1163 poration time, which is not easily predictable by MARTINI coarse-grained forcefield
1164 (*48*).
1165

1166 ***In silico* cell membrane hyperpolarization modeling through ion-imbalance in**
1167 **MARTINI coarse-grained simulations**

1168 The translocation mechanism of each CPP has been studied by ion-imbalance in a
1169 double bilayer system (*50, 69-71*). The same asymmetric membrane considered to
1170 perform the single-bilayer simulations (Table S2) was used to build up the double-
1171 bilayer system. The double-membrane system was solvated with 4300 water

1172 molecules, obtaining a molecular system of 20000 particles. The MARTINI (*101, 102*)
1173 force field was used to define phospholipids' topology through a coarse-grained (CG)
1174 approach. The polarizable water model has been used to model the water topology
1175 (*103*). The elastic network ELNEDYN (*106*) has been applied to reproduce the
1176 structural and dynamic properties of the CPPs.
1177 For each molecular system, one CPP was positioned in the middle of the double bilayer
1178 system, 2nm far from the membrane outer leaflets, in the water environment
1179 corresponding to the extracellular space. Then, the system was equilibrated through
1180 four MD simulations of 100ps, 200ps, 500 ps, and 100 ns under the NPT ensemble.
1181 Position restraints were applied during the first three MD simulations ang gradually
1182 removed, from 200 kJ/mol*nm^2 to 10 kJ/mol*nm^2. Velocity rescaling (*107*) temperature
1183 coupling algorithm and time constant of 1.0 ps were applied to keep the temperature
1184 at 310.00 K. Berendsen (*108*) semi-isotropic pressure coupling algorithm with
1185 reference pressure equal to 1 bar and time constant 5.0 ps was employed. Then, all
1186 systems were simulated for the production run in the NPT ensemble with the time step
1187 of 20 fs with Parrinello-Rahman pressure coupling (*112*). Membrane hyperpolarization
1188 was achieved through a net charge difference of 30 positive ions between intracellular
1189 and extracellular space, taking into account all charged ions of the system and fulfilling
1190 the full system electroneutrality. Ten different replicas of each molecular simulation
1191 have been performed until the water pore formation and closure events have been
1192 observed. The visual inspection of the simulated molecular systems is reported in Fig.
1193 S9F.
1194 Electrostatic interactions were calculated by applying the particle-mesh Ewald (PME)
1195 (*109*) method and van der Waals interactions were defined within a cut-off of 1.2 nm.
1196 Periodic boundary conditions were applied in all directions. Trajectories were collected

1197 every 1 ps and the Visual Molecular Dynamics (VMD) (*110*) package was employed to
1198 visually inspect the simulated systems. GROMACS 2018 was used for simulations and
1199 data analysis (*111*).
1200 To analyse whether the CPPs were able to cross the membrane and reach the
1201 intracellular compartment, their trajectories were studied in the last five nanoseconds
1202 of each simulation replica. Considering the CPP position with respect the membrane
1203 bilayers, three different compartments were defined: intracellular space, lipid bilayer
1204 (cell membrane) and extracellular space. The radius of the water pores within the
1205 membrane was calculated as previously done in literature (*69, 113*). We assumed that
1206 the central part of the cylindrical water pore contains N water molecules at the same
1207 density as outside of the water flux.

1208

1209 ***In vitro* assessment of water pores**

1210 Three hundred thousand wild-type HeLa cells were incubated with 32 ug/ml PI (0.8-
1211 1.5 nm diameter (*72*)) or 200 μg/ml dextran of different size in the presence or in the
1212 absence of indicated CPP in normal, depolarizing (2 μg/ml gramicidin) or
1213 hyperpolarizing (10 μM valinomycin) conditions. Time-lapse images were acquired by
1214 confocal microscopy every 10 seconds. The percentage of cells where direct CPP
1215 translocation has occurred, as well as the percentage of cells positively stained for PI,
1216 were manually quantitated using ImageJ based on snap shot images taken after 30
1217 minutes of incubation, as shown in Fig. S10B. Quantitation of cell percentage was not
1218 selective in terms of fluorescence intensity. Cytoplasmic PI fluorescence was
1219 assessed with ImageJ, by selecting a region within the cell cytoplasm devoid of
1220 endosomes. Saponin 0.1% (Sigma, Cat# 4706, diluted in PBS weight:volume) was

1221 used as a permeabilizing agent that leads to cell death to differentiate signal intensity
1222 between live cells with water pores and dead cells. As, the signal of PI uptake in
1223 saponin treated cells was saturated, lower laser settings were used to look at dead
1224 cells than at cells with water pores. Three fitting models were obtained: exponential
1225 decline: $y = 2568.704351e^{-\frac{x}{54.2680}}$, exponential $y = 2568.7044e^{-0.01842x}$ and modified
1226 power $y = 2568.70443 * 0.98142^{x}$, yielding virtually identical results. In Fig. 4F the
1227 exponential decline formula was used.
1228

1229 **Zebrafish viability**

1230 FITC-TAT-RasGAP$_{317\text{-}326}$(W317A) uptake in zebrafish was assessed either by adding
1231 the peptide directly in Egg water or by injection. Experiments in which the peptide was
1232 added in the water were performed on fish between four and 24 hours post fertilization.
1233 Viability assays were done on embryos of four, six and 24 hours post fertilization to
1234 determine a maximal nonlethal dose of the peptide that can be used. Different
1235 concentrations of the peptide were added to 500 μl water per well in 24-well plate, with
1236 between eight and eleven embryo per well. Fish viability was visually assessed at 20
1237 hours post incubation with the peptide. Hyperpolarization associated viability was
1238 visually assessed at different time points in presence or in the absence of the peptide
1239 and in presence or in the absence of different concentration of valinomycin. Zebrafish
1240 were visualized with binocular microscope and CYTATION3 apparatus. Survival was
1241 visually assessed under a binocular microscope by taking into consideration the
1242 embryo transparency (as dead embryos appear opaque), general development
1243 characteristics and motility.
1244

1245 **CPP uptake *in vivo***

1246 To assess peptide uptake in zebrafish, two methods were used: 1) addition of the
1247 peptide directly in 500 μl of Egg water in 24-well plates containing between eight and
1248 twelve embryos per well or 2) intramuscular injections. In the case of the first method,
1249 after the indicated treatments, zebrafish were washed, fixed in 4% PFA/PBS for one
1250 hour at room temperature. Whole embryos were mounted on slides with Fluoromount-
1251 G (cBioscience, Cat# 00-4958-02). Zebrafish were then visualized under a LSM710
1252 confocal microscope. Experiments where the peptide was added directly to the water
1253 were performed on zebrafish at 18 hours post fertilization to limit cuticle development
1254 that would hinder peptide access to the cells. In the case of the second method, 8 nl
1255 injections (containing the various combinations of peptide and valinomycin and 0.05 %
1256 (vol:vol) phenol red as an injection site labelling agent) were done on 48 hours post
1257 fertilization embryos into the tail muscle around the extremity of yolk extension, after
1258 chorion removal and anesthesia with 0.02% (w:vol) tricaine (*114*) buffered in sodium
1259 bicarbonate to pH7.3. At this age, zebrafish already have well developed tissues that
1260 can be easily visually distinguished. Injections were done with an Eppendorf
1261 Microinjections FemtoJet 4i apparatus. After the indicated treatments, embryos were
1262 fixed in 4% PFA/PBS and visualized under a confocal microscope. Some embryos
1263 were kept alive for viability evaluation post injection until the age of 4 days.

1264 Experiments with mice were performed in 10-14 weeks old C57BL/6NCrl mice
1265 anaesthetized with ketasol/xylasol (9.09 mg/ml ketasol and 1.82 mg/ml xylasol in
1266 water; injection: 10 μl per g of body weight). The back of the mice was shaved and
1267 intradermic injections were performed (a total of 10 μl was injected). Mice were kept
1268 under anesthesia for one hour and Artificial tears (Lacryvisc) were used to avoid eye
1269 dryness. Mice were then sacrificed by CO_2 inhalation, skin was cut at injection sites,

1270 fixed in 4% formalin and paraffin embedded for histology analysis. For each sample,
1271 10 to 15 slides were prepared and peptide uptake was visualized with a CYTATION3
1272 apparatus. Fluorescence intensity was quantitated with ImageJ. The slices displaying
1273 the highest fluorescence signal were considered as those nearest to the injection site
1274 and the fluorescent values from these slides were used in Fig. 5B.

1275

1276 **Temperature dependent uptake**

1277 Two hundred thousand cells were incubated with 40 μM (Raji and SKW6.4) or 80 μM
1278 (HeLa) of FITC-labelled TAT-RasGAP$_{317-326}$ for one hour in Eppendorf tubes in RPMI
1279 media supplemented with 10% serum and 10 mM Hepes on a thermoblock at different
1280 temperatures. Peptide uptake was measured by flow cytometry after PBS wash and
1281 addition of 0.2% trypan blue (in PBS) to quench extracellular fluorescence.

1282

1283 **Pyrene butyrate treatment**

1284 Cells were washed twice with serum-free medium and treated for 10 minutes with 50
1285 μM pyrene butyrate or 0.25% (vol:vol) DMSO as vehicle control at 37°C in 5% CO_2.
1286 Then cells were treated with TAT-RasGAP$_{317-326}$ for the indicated period of time.

1287

1288 **Assessment of endosomal escape and direct translocation**

1289 Quantitation of cytoplasmic fluorescence was performed within live HeLa cells pre-
1290 incubated with 80 μM TAT-RasGAP$_{317-326}$ for 30 minutes at 37°C and then incubated
1291 for the indicated periods of time in the presence (i.e. no wash after the pre-incubation)
1292 or in the absence (i.e. following three consecutive washes with RPMI supplemented
1293 with 10% FBS) of extracellular labelled peptide. Endosomal escape from lysosomes

1294 was induced in presence of 1 mM LLOME (L-Leucyl-L-Leucine methyl ester) (*36*),
1295 added in the media 30 minutes after CPP was washed out and persisted throughout
1296 the experiment). Confocal images were taken every five minutes after the 30-minute
1297 pre-incubation. For each cell, the fluorescence intensity of one region of interest (ROI)
1298 devoid of labelled endosomes throughout the experiment was quantitated over time
1299 using ImageJ Time Series Analyzer V3. The surface of the ROI was identical for all
1300 cells. Only cells displaying labelled endosomes after the 30-minute pre-incubation
1301 were analyzed. Note that the washing steps, for reasons unclear at this time, induced
1302 a slightly higher initial ROI intensity signal.
1303
1304 **Transferrin uptake quantitation**
1305 HeLa wild-type cells were plated in 12-well plates (200'000 cells per well) for 16 hours
1306 in 1 ml RPMI (Invitrogen, Cat# 61870), supplemented with 10 % heat-inactivated fetal
1307 bovine serum (FBS; Invitrogen, Cat# 10270-106). Cells were then incubated in
1308 presence of 20 μg/ml AlexaFluor-488 conjugated transferrin for 20 minutes at 37°C in
1309 5% CO_2. Cells were washed with PBS and pelleted after trypsinization. To quench
1310 membrane bound transferrin fluorescence, cells were resuspended in 0.2% trypan blue
1311 diluted in PBS. Transferrin uptake was quantified by flow cytometry using Beckman
1312 Coulter FC500 instrument. Data analysis was done with Kaluza Version 1.3 software
1313 (Beckman Coulter).
1314
1315 **TAT-PNA-induced luciferase activity**
1316 The LeGOiG2-LUC705 lentiviral construct encodes a luciferase gene interrupted by a
1317 mutated human beta globin intron 2. This mutation creates a new aberrant splicing site
1318 at position 705 that when used produced an mRNA that encodes a truncated non-

1319 functional luciferase. In the presence of the TAT-peptide nucleic acid (TAT-PNA) CPP
1320 described below, the aberrant splice site is masked allowing the production of a
1321 functional luciferase enzyme. Lentiviruses produced using this construct were
1322 employed to infect cells. The doses used resulted in >90% cells infected (based on
1323 GFP expression from the lentiviral vector). The infected cells (200'000 cells in 12 well
1324 plates containing 1 ml of RPMI, 10% FBS) were treated or not with 5 µM TAT-PNA
1325 (GRKKRRQRRR-CCTCCTACCTCAGTTACA). TAT-PNA is made of TAT_{48-57} and an
1326 an oligonucleotide complimentary to a sequence containing the aberrant splice site.
1327 After 16 hours incubation, cells were washed twice in HKR buffer (119 mM NaCl, 2.5
1328 mM KCl, 1 mM NaH_2PO_4, 2.5 mM $CaCl_2$, 1.3 mM $MgCl_2$, 20 mM HEPES, 11 mM
1329 dextrose, pH 7.4) and lysed in 40 µl HKR containing 0.1 % Triton X-100 for 15 minutes
1330 at room temperature. Luciferase activity was measured with a GLOMAXTM 96
1331 Microplate Luminometer (Promega) using a Dual-Luciferase Reporter Assay
1332 (Promega) and normalized to the protein content. Results are displayed as the ratio
1333 between the protein-normalized luciferase signal obtained in TAT-PNA-treated cells
1334 and the signal obtained in control untreated cells.
1335

1336 **TAT-Cre recombinase production, purification and recombination assay**

1337 Raji cells were infected with a lentivirus encoding a Cre-reporter gene construct (*39*).
1338 TAT-Cre recombinase was produced as described (*40*). Briefly, *E. coli* BL21
1339 transformed with the pTAT-Cre plasmid were grown for 16 hours in LB containing 100
1340 µg/mL kanamycin. Protein production was induced at OD_{600} of 0.6 with 500 µM IPTG
1341 (isopropyl β-D-1-thiogalactopyranoside) for three hours. Bacteria were collected by
1342 centrifugation at 5000 x g and kept at -20°C. Purification was performed on Äkta prime
1343 (GE, Healthcare, USA) equipped with a 1 ml HisTrap FF column equilibrated with

1344 binding buffer (20 mM sodium phosphate, 500 mM NaCl, 5 mM imidazole pH 7.4). The
1345 day of the purification, bacterial pellet was resuspended in lysis buffer (binding buffer
1346 with protease inhibitors (Roche, Cat# 4693132001; one tablet per 50 ml), 0.025 mg/ml
1347 DNase I (Roche, Cat# 04716728001), and 2 mg/ml lysozyme (Roche, Cat# 10 837 059
1348 001) and sonicated six times for 30 seconds. After 20 minutes centrifugation at 5'000
1349 x g, the supernatant was filtered through Steriflip 0.45 μm and loaded on the column.
1350 Elution buffer (20 mM sodium phosphate, 500 mM NaCl, 500 mM imidazole pH 7.4)
1351 was used to detach His-tagged proteins from the column. Imidazole was removed from
1352 collected fractions by overnight dialysis using 10K MWCO cassette (Thermo Scientific,
1353 Cat# 66807) in PBS. Raji cells encoding the Cre-reporter were treated for 48 hours
1354 with 20 μM TAT-Cre-recombinase. Fluorescence was imaged using a Nikon Eclipse
1355 TS100 microscope.
1356
1357 **Extracellular pH manipulation**
1358 Two hundred thousand wild-type Raji cells were incubated in 500 μl RPMI media,
1359 supplemented with 10% FBS, set at the indicated pH for 20 minutes at 37°C in 5%
1360 CO_2, with or without 10 μM valinomycin or 2 μg/ml gramicidin to induce
1361 hyperpolarization or depolarization respectively. Changes to the extracellular pH were
1362 done by adding NaOH or HCl to the RMPI media. The pH was measured with a pH
1363 meter (Metrohm, 744 pH Meter). TMR-TAT-RasGAP$_{317-326}$ 40 μM was then added to
1364 cells for one hour. Peptide uptake was assessed by flow cytometry. These experiments
1365 were performed in the presence of FBS because in its absence, cells are too sensitive
1366 to acidification or alkalization. In addition, TMR-labelled peptide was used to avoid
1367 FITC-quenching at acidic pH.
1368

1369 **Assessment of CPP binding to plasma membranes**

1370 Two hundred thousand cells were incubated for 60 seconds in RPMI supplemented
1371 with 10% FBS and 10 mM HEPES in Eppendorf tubes at 37°C in the presence of
1372 increasing concentrations of FITC-TAT-RasGAP$_{317-326}$. Half of the cells were then
1373 immediately placed on ice, pelleted at 4°C, and resuspended in one ml of ice-cold PBS
1374 and then split into two tubes, one of which receiving a final concentration of 0.2% (w:w)
1375 trypan blue to quench surface-associated FITC signals. The cells (still kept at 4°C)
1376 were then analyzed by flow cytometry. The surface associated peptide signal was
1377 calculated by subtracting total fluorescence measured in PBS and fluorescence
1378 measured after trypan blue quenching. The other half of the cells after the 60 second
1379 peptide incubation was incubated at 37°C for one hour at which time the cellular uptake
1380 of the labelled peptide was assessed by flow cytometry.

1381

1382 **Transient calcium phosphate transfection in HeLa**

1383 Calcium phosphate based transfection of HeLa cells was performed as previously
1384 described(*115*). Briefly, cells were plated overnight in DMEM (Invitrogen, Cat# 61965)
1385 medium supplemented with 10 % heat-inactivated FBS (Invitrogen, Cat# 10270-106),
1386 2.5 ug of total plasmid DNA of interest was diluted in water, $CaCl_2$ was added and the
1387 mixture was incubated in presence of HEPES 2x for 60 seconds before adding the
1388 total mixture drop by drop to the cells. Media was changed 10 hours after.

1389

1390 **Isothermal titration calorimetry (ITC)**

1391 ITC was performed using MicroCal ITC200 (Malvern Panalytical) at 37°C with 600 μM
1392 FITC-R9 in the cell (total volume 300 μl) and consecutive injections (2.5 μl/injection,
1393 except for the first injection of 0.4 μl) of 6 mM PI from the syringe (total volume 40 μl)

1394 with 2 minutes delay between injections and 800 rotations/minute rotation speed.
1395 Differential power was set to 7, as we had no prior knowledge of the expected reaction
1396 thermodynamics.
1397

1398 **Colony formation assay**

1399 Wild-type HeLa cells were plated overnight in RPMI with 10% FBS in 12-well plates.
1400 Cells were then treated for one hour in the presence of indicated concentrations of
1401 CPP, PI and membrane potential modulating agents (gramicidin or valinomycin). As
1402 control, cells were either left untreated or incubated in presence of DMSO used as
1403 vehicle for gramicidin and valinomycin. Cells were then washed, trypsinized and plated
1404 on 10 cm dishes at a density of 300 cells per condition. Colonies were counted at day
1405 14 after 100% ethanol fixation for 10 minutes and Giemsa staining. Washes were done
1406 with PBS.
1407

1408 **Genome-scale CRISPR/Cas9 Knockout screening**

1409 The human GeCKO v2 library (2 plasmid system) (Addgene plasmid #1000000049)
1410 was amplified by electroporation using a Bio-Rad Gene Pulser II electroporation
1411 apparatus (Bio-Rad #165-2105) and the Lucigen Endura bacteria (Lucigen Cat#
1412 60242). Cells were plated on LB Agar plates containing 100 µg/mL ampicillin. After 14
1413 hours at 32°C, colonies were scrapped and plasmids recovered with the Plasmid Maxi
1414 kit (Qiagen, Cat# 12162). To produced lentivirus library, 12 T-225 flasks were seeded
1415 with $12x10^6$ HEK293T cells per flask in 40 ml DMEM, 10% FBS. The day after, 10 µg
1416 pMD2.G, 30 µg psPAX2 and 25 µg GeCKO plasmid library in 1.8 ml H_2O were mixed
1417 with 0.2 ml 2.5 M $CaCl_2$ (final calcium concentration: 250 mM). This solution was mixed
1418 (v/v) with 2x HEPES buffer (280 mM NaCl, 10 mM KCl, 1.5 mM Na_2HPO_4, 12 mM D-

1419 glucose, 50 mM HEPES), incubated for one minute at room temperature, added to the
1420 culture medium, and the cells placed back in a 37°C, 5% CO_2 incubator for seven
1421 hours. The culture medium was then removed and replaced by DMEM supplemented
1422 with 10 % FBS containing 100 U/ml penicillin and 100 μg/ml streptomycin. Forty eight
1423 hours later, the medium was collected and centrifuged 5 min at 2'000 g to pellet the
1424 cells. The remaining cell-free medium (12 x 40 ml) was then filtered through a 0.45 µm
1425 HV/PVDF (Millipore, Cat# SE1M003M00) and concentrated ~100 times by
1426 resuspending the viral pellet obtained by ultracentrifugation at 70'000 g for two hours
1427 at 4°C in ~5 ml ice-cold PBS. The concentrated viruses were aliquoted in 500 μl
1428 samples and stored at -80°C.
1429 To express the Cas9 endonuclease, cells (e.g. Raji or SKW6.4) were infected with
1430 Cas9 expressing viruses that were produced in HEK293T cells transfected with the
1431 lentiCas9-Blast (#849, Addgene plasmid #52962), pMD2.G, and psPAX2 plasmids as
1432 described in the main method under "Lentivirus production". The infected cells were
1433 selected with 10 µg/mL blasticidin for a week. The multiplicity of infection (MOI) of the
1434 GeCKO virus library was determined as follow. Different volumes of the virus library
1435 were added to $3x10^6$ Cas9-expressing cells plated in 12-well plates. Twenty four hours
1436 later, the cells were split in two wells of 12-well plates. One well per pair was treated
1437 with 10 µg/mL puromycin for 3 days (the other cultured in normal medium). Cell viability
1438 was determined by trypan blue exclusion and MOI was calculated as the number of
1439 cells in the well treated with puromycin divided by the number of cells in the control
1440 well. The virus volume yielding to a MOI ~0.4 was chosen to perform large-scale
1441 infection of $12x10^7$ cells that was carried out in 12-well plates with $3x10^6$ cells per well.
1442 After 24 hours, the infected cells were collected and pooled in a T-225 flask and
1443 selected with 10 µg/mL puromycin for a week. Thirty millions of these were frozen

1444 (control untreated cells) and 60 million others were treated with 40 µM TAT-
1445 RasGAP$_{317-326}$ for 8 days (Raji) or for 17 days (SKW6.4) with a medium and peptide
1446 renewal every 2-3 days. Thirty millions of the peptide-treated cells were then also
1447 frozen. Genomic DNA was extracted from the control and the peptide-treated frozen
1448 cells using the Blood & Cell Culture DNA Midi Kit according to manufacturer's
1449 instructions (Qiagen, Cat# 13343). A first PCR was performed to amplify the
1450 lentiCRISPR sgRNA region using the following primers:

1451 F1: 5'-AATGGACTATCATATGCTTACCGTAACTTGAAAGTATTTCG-3'

1452 R1: 5'-CTTTAGTTTGTATGTCTGTTGCTATTATGTCTACTATTCTTTCC-3

1453 A second PCR (see Table S3 for the primers used) was performed on 5 µl of the first
1454 PCR reaction to attach Illumina adaptors with barcodes (nucleotides highlighted in
1455 green) and to increase library complexity (using the sequences highlighted in red) to
1456 prevent signal saturation when the sequencing is performed. The blue sequences are
1457 complementary to the extremities of the first PCR fragments.

1458 **Table S3. Primer sequences for the second PCR**

F2a	AATGATACGGCGACCACCGAGATCTACACTCTTTCCCTACACGACGCTCTTCCGATCTTCTTGTGGAAAGGACGAAACACCG
F2b	AATGATACGGCGACCACCGAGATCTACACTCTTTCCCTACACGACGCTCTTCCGATCTAGCTCTTGTGGAAAGGACGAAACACCG
F2c	AATGATACGGCGACCACCGAGATCTACACTCTTTCCCTACACGACGCTCTTCCGATCTCGAGCTCTTGTGGAAAGGACGAAACACCG
F2d	AATGATACGGCGACCACCGAGATCTACACTCTTTCCCTACACGACGCTCTTCCGATCTCATAACCTCTTGTGGAAAGGACGAAACACCG
F2e	AATGATACGGCGACCACCGAGATCTACACTCTTTCCCTACACGACGCTCTTCCGATCTGTGCTAACGTCTTGTGGAAAGGACGAAACACCG
R2_iC_26	CAAGCAGAAGACGGCATACGAGAT**GCTCAT**GTGACTGGAGTTCAGACGTGTGCTCTTCCGATCTTCTACTATTCTTTCCCCTGCACTGT
R2_iA_12	CAAGCAGAAGACGGCATACGAGAT**TACAAG**GTGACTGGAGTTCAGACGTGTGCTCTTCCGATCTTCTACTATTCTTTCCCCTGCACTGT

1459

1460 Both PCRs were performed in 100 µl with the 2 µl of the Herculase II Fusion DNA
1461 Polymerase from Agilent (Cat# 600675) according the manufacturer's instructions.
1462 Amplicons were gel extracted, quantitated, mixed and sequenced with a MiSeq
1463 (Illumina). Raw FASTQ files were demultiplexed and processed to contain only unique

1464 sgRNA sequences. The number of reads of each sgRNA was normalized as
1465 described(*116*). The MAGeCK algorithm(*117*) was used to rank screening hits by the
1466 consistent enrichment among multiple sgRNAs targeting the same gene.
1467

1468 **CRISPR/Cas9-based genome editing**

1469 Single guide RNAs targeting the early exon of the protein of interest were chosen in
1470 the sgRNA library(*116*) and are listed in table I below (Table S4). LentiCRISPR
1471 plasmids specific for a gene were created according to the provided instructions(*118*).
1472 Briefly, oligos were designed as follow: Forward 5'-CACCGnnnnnnnnnnnnnnnnnnnn-
1473 3'; Reverse-3'-CnnnnnnnnnnnnnnnnnnnnCAA-5', where nnnnnnnnnnnnnnnnnnnn in
1474 the forward oligo corresponds to the 20 bp sgRNA. Oligos were synthetized, then
1475 phosphorylated and annealed to form oligo complex. LentiCRISPR vector was BsmBI
1476 digested and dephosphorylated. Linearized vector was purified and gel extracted and
1477 ligated to oligo complex. The lentiCRISPR vector containing the sgRNA was then used
1478 for virus production. Recombinant lentiviruses were produced as described (*94*) with
1479 the following modification: pMD.G and pCMVDR8.91 were replaced by pMD2.G and
1480 psPAX2 respectively. Cells were infected and selected with the appropriate dose of
1481 puromycin (2 µg/ml for HeLa). Clone isolation was performed by limiting dilution in 96
1482 well-plate.

1483 **Table S4. List of sgRNAs used to disrupt target genes**

Target gene	sgRNA name	sgRNA sequence
KCNN4	sgKCNN4.1	CTGCCCGAGTGCTACAAGAA
KCNN4	sgKCNN4.2	CATGGTGCCCGGCACCACGT
KCNK5	sgKCNK5.1	ATGGTGGTAATGACGGTCGC
KCNK5	sgKCNK5.2	CTCTGCCTGACGTGGATCAG
KCNQ5	sgKCNQ5.1	TCTAGGAATTAATTCACAGC

KCNQ5	sgKCNQ5.2	ACAGATCCTCCGCATGGTCG

1484

1485 **TA cloning**

1486 TA cloning kit (Life technologies, Cat# K202020) was used according to manufacturer's
1487 instructions to sequence DNA fragment containing the region where Cas9 was guided
1488 by a sgRNA.

1489

1490 **Plasmid constructs**

1491 The hKCNN4-V5.lti (#953) lentiviral plasmid encoding a V5-labeled version of the
1492 KCNN4 potassium channel was from DNASU (ref. n° HsCD00441560). The hKCNK5-
1493 FLAG.dn3 (#979) plasmid encoding the human KCNK5 potassium channel (NCBI
1494 reference sequence NM_003740.3), Flag-tagged at the C-terminus, was purchased
1495 from GenScript (ref. n° OHu13506). The Myc-mKCNJ2-T2A-IRES-tdTomato.lti (#978)
1496 lentiviral vector encoding the mouse Kir2.1 (KCNJ2) potassium channel and tdTomato
1497 (separated by an IRES) was generated by subcloning myc-mKCNJ2-T2A-
1498 Tomato.pCAG plasmid (#974), a gift from Dr. Massimo Scanziani**(*44*)** (Addgene
1499 plasmid #60598) into a lentiviral backbone LeGo-iT2 (#809), a gift from Boris Fehse
1500 (Addgene plasmid #27343), through ligation of both plasmids after digestion with
1501 BamHI (NEB, reg. no. R313614). The pMD2.G plasmid (#554, Addgene plasmid
1502 #12259) encodes the envelope of lentivirus. The psPAX2 plasmid (#842, Addgene
1503 plasmid #12260) encodes the packaging system. Both pMD2.G and psPAX2 plasmids
1504 were used for lentiviral production. The Flag-hKCNQ5(G278S)-IRES-NeoR plasmid
1505 (#938) codes for the N-terminal Flag-tagged G278S human KCNQ5 inactive mutant
1506 and a neomycin resistant gene separated by an IRES sequence. It was generated by
1507 subcloning a BamHI/XmaI digested PCR fragment obtained by amplification of

1508 pShuttle-Flag-hKCNQ5(G278S)-IRES-hrGFP2 (#937, kind gift from Dr. Kenneth L.
1509 Byron) using forward primer #1397 (CAT CGG GAT CCG CTA TAC CGG CCA CCA
1510 TGG ATT ACA AGG A) and reverse primer #1398 (CAT CGC CCG GGG CTA TAC
1511 CGT ACC GTC GAC TGC AGA ATT C) into the lentiviral vector TRIP-PGK-IRES-Neo
1512 (#350) opened with the same enzyme. The Flag-hKCNQ5(SM,G278S)-IRES-Neo
1513 (#939) plasmid is identical to Flag-hKCNQ5(G278S)-IRES-NeoR except that the
1514 sequence targeted by the sgKCNQ5.1 sgRNA (Table S4) was mutated with the aim to
1515 decrease Cas9-mediated degradation. Silent mutations (SM), at the protein level, were
1516 introduced using the QuikChange II XL Site-Directed Mutagenesis Kit (Cat# 200522)
1517 according to manufacturer's instructions using forward primer #1460 (AAA TAA GAA
1518 CCA AAA ATC CTA TGT ACC ATG CCG TTA TCA GCT CCT TGC TGT GAG CAT
1519 AAA CCA CTG AAC CCA G) and reverse primer #1461 (CTG GGT TCA GTG GTT
1520 TAT GCT CAC AGC AAG GAG CTG ATA ACG GCA TGG TAC ATA GGA TTT TTG
1521 GTT CTT ATT T).

1522 The Flag-hKCNQ5(SM)-IRES-NeoR (#940) lentiviral construct codes for a Flag-tagged
1523 wild-type version of human KCNQ5. It was made by reverting the G278S mutation in
1524 Flag-hKCNQ5(SM,G278S)-IRES-Neo (#939) using the QuikChange II XL Site-
1525 Directed Mutagenesis Kit with the #1462 forward primer (TTT TGT CTC CAT AGC
1526 CAA TAG TTG TCA ATG TAA TTG TGC CCC) and the #1463 reverse primer (GGG
1527 GCA CAA TTA CAT TGA CAA CTA TTG GCT ATG GAG ACA AAA). The
1528 pLUC705(*37*) (#876, gift from Dr. Bing Yang) plasmid encodes a luciferase gene
1529 interrupted by a mutated human beta globin intron 2. This mutation creates a new
1530 aberrant splicing site at position 705 that when used produced an mRNA that encodes
1531 a truncated non-functional luciferase(*37*). To introduce this construct into a lentiviral
1532 vector, the pLUC705 plasmid was digested with HindIII/XhoI, blunted with T4 DNA

1533 polymerase, and ligated into StuI-digested and dephosphorylated LeGO-iG2 (#807,
1534 Addgene plasmid #27341), resulting in plasmid pLUC705.LeGO-iG2 (#875). The
1535 pTAT-Cre (#917, Addgene plasmid #35619) bacterial plasmid encodes a histidine-
1536 tagged TAT-Cre recombinase. The Cre reporter lentiviral vector (#918, Addgene
1537 plasmid #62732) encodes a LOXP-RFP-STOP-LOXP-GFP gene construct. Cells
1538 expressing this plasmid appear red but once recombination has occurred when TAT-
1539 Cre is translocated into cells the RFP-STOP fragment will be excised, GFP but not
1540 RFP will now be produced, and cells will appear green.

1541 **Peptides**

1542 TAT-RasGAP$_{317\text{-}326}$ is a retro-inverso peptide (i.e. synthesized with D-amino-acids in
1543 the opposite direction compared to the natural sequence) labeled or not with FITC or
1544 TMR. The TAT moiety corresponds to amino-acids 48–57 of the HIV TAT protein
1545 (RRRQRRKKRG) and the RasGAP$_{317–326}$ moiety corresponds to amino-acids from 317
1546 to 326 of the human RasGAP protein (DTRLNTVWMW). These two moieties are
1547 separated by two glycine linker residues in the TAT-Ras-GAP$_{317–326}$ peptide. FITC-
1548 bound peptides without cargo: TAT, MAP (KLALKLALKALKAALKLA), Penetratin
1549 (RQIKWFQNRRMKWKK), Transportan (GWTLNSAGYLLGKINLKALAALAKKIL), R9
1550 (RRRRRRRRR), K9 (KKKKKKKKK) and (RE)9 (RERERERERERERERERE) were
1551 synthesized in D-amino-acid conformation. All peptides were synthesized in retro-
1552 inverso conformation (over the years different suppliers were used with routine checks
1553 for activity of TAT-RasGAP$_{317\text{-}326}$ derived peptides, see Key Resources Table) and
1554 resuspended to 1 mM in water.

1555

1556 **Statistical analysis**

1557 Statistical analysis was performed on non-normalized data, using GraphPad Prism 7.
1558 ANOVA multiple comparison analysis to wild-type condition was done using Dunnett's
1559 correction for analyses related to membrane potential measurements in Fig. 3B and PI
1560 uptake in Fig. 4D, as well as TAT-PNA uptake in Fig. S7. Comparison between two
1561 conditions was done using two-tailed paired t-tests for the CPP uptake experiments
1562 described in Fig. 3C, Fig. 5A-B and Fig. S8F. All measurements were from biological
1563 replicates. Unless otherwise stated, the horizontal bars in the graph represent the
1564 median, the height of columns correspond to averages, and the dots in the Figures
1565 correspond to values derived from independent experiments.

1566

1567 **Data availability**

1568 DNA sequencing data from the CRISPR/Cas9-based screens are available through
1569 the following link: https://www.ncbi.nlm.nih.gov/sra/SRP161445.

1570

1571

1572

1573

1574

1575 # References and notes

1576 1. G. Guidotti, L. Brambilla, D. Rossi, Cell-Penetrating Peptides: From Basic Research to Clinics.
1577 *Trends Pharmacol Sci* **38**, 406-424 (2017).
1578 2. L. Vasconcelos, K. Parn, U. Langel, Therapeutic potential of cell-penetrating peptides. *Ther*
1579 *Deliv* **4**, 573-591 (2013).
1580 3. C. Bechara, S. Sagan, Cell-penetrating peptides: 20 years later, where do we stand? *FEBS Lett*
1581 **587**, 1693-1702 (2013).
1582 4. S. Trabulo, A. L. Cardoso, M. Mano, M. C. De Lima, Cell-Penetrating Peptides-Mechanisms of
1583 Cellular Uptake and Generation of Delivery Systems. *Pharmaceuticals (Basel)* **3**, 961-993
1584 (2010).
1585 5. S. Futaki, H. Hirose, I. Nakase, Arginine-rich peptides: methods of translocation through
1586 biological membranes. *Curr Pharm Des* **19**, 2863-2868 (2013).
1587 6. A. T. Jones, E. J. Sayers, Cell entry of cell penetrating peptides: tales of tails wagging dogs. *J*
1588 *Control Release* **161**, 582-591 (2012).
1589 7. F. Madani, S. Lindberg, U. Langel, S. Futaki, A. Graslund, Mechanisms of cellular uptake of
1590 cell-penetrating peptides. *J Biophys* **2011**, 414729 (2011).
1591 8. E. Koren, V. P. Torchilin, Cell-penetrating peptides: breaking through to the other side. *Trends*
1592 *Mol Med* **18**, 385-393 (2012).
1593 9. F. Illien *et al.*, Quantitative fluorescence spectroscopy and flow cytometry analyses of cell-
1594 penetrating peptides internalization pathways: optimization, pitfalls, comparison with mass
1595 spectrometry quantification. *Sci Rep* **6**, 36938 (2016).
1596 10. J. Mueller, I. Kretzschmar, R. Volkmer, P. Boisguerin, Comparison of cellular uptake using 22
1597 CPPs in 4 different cell lines. *Bioconjug Chem* **19**, 2363-2374 (2008).
1598 11. A. D. Frankel, C. O. Pabo, Cellular uptake of the tat protein from human immunodeficiency
1599 virus. *Cell* **55**, 1189-1193 (1988).
1600 12. M. Green, P. M. Loewenstein, Autonomous functional domains of chemically synthesized
1601 human immunodeficiency virus tat trans-activator protein. *Cell* **55**, 1179-1188 (1988).
1602 13. A. Joliot, C. Pernelle, H. Deagostini-Bazin, A. Prochiantz, Antennapedia homeobox peptide
1603 regulates neural morphogenesis. *Proc Natl Acad Sci U S A* **88**, 1864-1868 (1991).
1604 14. J. Oehlke *et al.*, Cellular uptake of an alpha-helical amphipathic model peptide with the
1605 potential to deliver polar compounds into the cell interior non-endocytically. *Biochim Biophys*
1606 *Acta* **1414**, 127-139 (1998).
1607 15. D. Michod, J. Y. Yang, J. Chen, C. Bonny, C. Widmann, A RasGAP-derived cell permeable
1608 peptide potently enhances genotoxin-induced cytotoxicity in tumor cells. *Oncogene* **23**,
1609 8971-8978 (2004).
1610 16. D. Michod *et al.*, Effect of RasGAP N2 fragment-derived peptide on tumor growth in mice. *J*
1611 *Natl Cancer Inst* **101**, 828-832 (2009).
1612 17. O. Pittet *et al.*, Effect of the TAT-RasGAP(317-326) peptide on apoptosis of human malignant
1613 mesothelioma cells and fibroblasts exposed to meso-tetra-hydroxyphenyl-chlorin and light. *J*
1614 *Photochem Photobiol B* **88**, 29-35 (2007).
1615 18. P. Tsoutsou *et al.*, TAT-RasGAP317-326 Enhances Radiosensitivity of Human Carcinoma Cell
1616 Lines In Vitro and In Vivo through Promotion of Delayed Mitotic Cell Death. *Radiat Res* **187**,
1617 562-569 (2017).
1618 19. N. Chevalier, N. Gross, C. Widmann, Assessment of the chemosensitizing activity of TAT-
1619 RasGAP317-326 in childhood cancers. *PLoS One* **10**, e0120487 (2015).
1620 20. D. Barras *et al.*, Fragment N2, a caspase-3-generated RasGAP fragment, inhibits breast cancer
1621 metastatic progression. *Int J Cancer* **135**, 242-247 (2014).
1622 21. D. Barras, G. Lorusso, C. Ruegg, C. Widmann, Inhibition of cell migration and invasion
1623 mediated by the TAT-RasGAP317-326 peptide requires the DLC1 tumor suppressor.
1624 *Oncogene* **33**, 5163-5172 (2014).

1625 22. M. Heulot *et al.*, The TAT-RasGAP317-326 anti-cancer peptide can kill in a caspase-,
1626 apoptosis-, and necroptosis-independent manner. *Oncotarget* **7**, 64342-64359 (2016).
1627 23. Q. Zheng, S. Jockusch, Z. Zhou, S. C. Blanchard, The contribution of reactive oxygen species to
1628 the photobleaching of organic fluorophores. *Photochem Photobiol* **90**, 448-454 (2014).
1629 24. T. Ha, P. Tinnefeld, Photophysics of fluorescent probes for single-molecule biophysics and
1630 super-resolution imaging. *Annu Rev Phys Chem* **63**, 595-617 (2012).
1631 25. R. Dixit, R. Cyr, Cell damage and reactive oxygen species production induced by fluorescence
1632 microscopy: effect on mitosis and guidelines for non-invasive fluorescence microscopy. *Plant*
1633 *J* **36**, 280-290 (2003).
1634 26. M. Levitus, S. Ranjit, Cyanine dyes in biophysical research: the photophysics of polymethine
1635 fluorescent dyes in biomolecular environments. *Q Rev Biophys* **44**, 123-151 (2011).
1636 27. W. P. Verdurmen, M. Thanos, I. R. Ruttekolk, E. Gulbins, R. Brock, Cationic cell-penetrating
1637 peptides induce ceramide formation via acid sphingomyelinase: implications for uptake. *J*
1638 *Control Release* **147**, 171-179 (2010).
1639 28. H. Hirose *et al.*, Transient focal membrane deformation induced by arginine-rich peptides
1640 leads to their direct penetration into cells. *Mol Ther* **20**, 984-993 (2012).
1641 29. K. Melikov *et al.*, Efficient entry of cell-penetrating peptide nona-arginine into adherent cells
1642 involves a transient increase in intracellular calcium. *Biochem J* **471**, 221-230 (2015).
1643 30. B. C. Suh, B. Hille, PIP2 is a necessary cofactor for ion channel function: how and why? *Annu*
1644 *Rev Biophys* **37**, 175-195 (2008).
1645 31. C. C. Shieh, M. Coghlan, J. P. Sullivan, M. Gopalakrishnan, Potassium channels: molecular
1646 defects, diseases, and therapeutic opportunities. *Pharmacol Rev* **52**, 557-594 (2000).
1647 32. B. C. Schroeder, M. Hechenberger, F. Weinreich, C. Kubisch, T. J. Jentsch, KCNQ5, a novel
1648 potassium channel broadly expressed in brain, mediates M-type currents. *J Biol Chem* **275**,
1649 24089-24095 (2000).
1650 33. H. Wulff *et al.*, Design of a potent and selective inhibitor of the intermediate-conductance
1651 Ca2+-activated K+ channel, IKCa1: a potential immunosuppressant. *Proc Natl Acad Sci U S A*
1652 **97**, 8151-8156 (2000).
1653 34. H. Wulff, G. A. Gutman, M. D. Cahalan, K. G. Chandy, Delineation of the clotrimazole/TRAM-
1654 34 binding site on the intermediate conductance calcium-activated potassium channel,
1655 IKCa1. *J Biol Chem* **276**, 32040-32045 (2001).
1656 35. S. Katayama *et al.*, Effects of pyrenebutyrate on the translocation of arginine-rich cell-
1657 penetrating peptides through artificial membranes: recruiting peptides to the membranes,
1658 dissipating liquid-ordered phases, and inducing curvature. *Biochim Biophys Acta* **1828**, 2134-
1659 2142 (2013).
1660 36. U. Repnik *et al.*, L-leucyl-L-leucine methyl ester does not release cysteine cathepsins to the
1661 cytosol but inactivates them in transiently permeabilized lysosomes. *J Cell Sci* **130**, 3124-3140
1662 (2017).
1663 37. S. H. Kang, M. J. Cho, R. Kole, Up-regulation of luciferase gene expression with antisense
1664 oligonucleotides: implications and applications in functional assay development.
1665 *Biochemistry* **37**, 6235-6239 (1998).
1666 38. S. Abes *et al.*, Efficient splicing correction by PNA conjugation to an R6-Penetratin delivery
1667 peptide. *Nucleic Acids Res* **35**, 4495-4502 (2007).
1668 39. D. S. D'Astolfo *et al.*, Efficient intracellular delivery of native proteins. *Cell* **161**, 674-690
1669 (2015).
1670 40. J. S. Wadia, R. V. Stan, S. F. Dowdy, Transducible TAT-HA fusogenic peptide enhances escape
1671 of TAT-fusion proteins after lipid raft macropinocytosis. *Nat Med* **10**, 310-315 (2004).
1672 41. G. Eisenman, J. Sandblom, E. Neher, Interactions in cation permeation through the
1673 gramicidin channel. Cs, Rb, K, Na, Li, Tl, H, and effects of anion binding. *Biophys J* **22**, 307-340
1674 (1978).

42. D. A. Kelkar, A. Chattopadhyay, The gramicidin ion channel: a model membrane protein. *Biochim Biophys Acta* **1768**, 2011-2025 (2007).
43. T. S. Rimmele, J. Y. Chatton, A novel optical intracellular imaging approach for potassium dynamics in astrocytes. *PLoS One* **9**, e109243 (2014).
44. M. Xue, B. V. Atallah, M. Scanziani, Equalizing excitation-inhibition ratios across visual cortical neurons. *Nature* **511**, 596-600 (2014).
45. J. B. Rothbard, T. C. Jessop, R. S. Lewis, B. A. Murray, P. A. Wender, Role of membrane potential and hydrogen bonding in the mechanism of translocation of guanidinium-rich peptides into cells. *J Am Chem Soc* **126**, 9506-9507 (2004).
46. H. D. Herce, A. E. Garcia, M. C. Cardoso, Fundamental molecular mechanism for the cellular uptake of guanidinium-rich molecules. *J Am Chem Soc* **136**, 17459-17467 (2014).
47. S. J. Marrink, H. J. Risselada, S. Yefimov, D. P. Tieleman, A. H. de Vries, The MARTINI force field: coarse grained model for biomolecular simulations. *J Phys Chem B* **111**, 7812-7824 (2007).
48. S. J. Marrink, D. P. Tieleman, Perspective on the Martini model. *Chem Soc Rev* **42**, 6801-6822 (2013).
49. H. I. Ingolfsson *et al.*, Lipid organization of the plasma membrane. *J Am Chem Soc* **136**, 14554-14559 (2014).
50. X. Gao *et al.*, Membrane potential drives direct translocation of cell-penetrating peptides. *Nanoscale* **11**, 1949-1958 (2019).
51. D. P. Tieleman, The molecular basis of electroporation. *BMC Biochem* **5**, 10 (2004).
52. A. A. Gurtovenko, A. S. Lyulina, Electroporation of asymmetric phospholipid membranes. *J Phys Chem B* **118**, 9909-9918 (2014).
53. R. A. Bockmann, B. L. de Groot, S. Kakorin, E. Neumann, H. Grubmuller, Kinetics, statistics, and energetics of lipid membrane electroporation studied by molecular dynamics simulations. *Biophys J* **95**, 1837-1850 (2008).
54. M. L. Fernandez, G. Marshall, F. Sagues, R. Reigada, Structural and kinetic molecular dynamics study of electroporation in cholesterol-containing bilayers. *J Phys Chem B* **114**, 6855-6865 (2010).
55. M. J. Ziegler, P. T. Vernier, Interface water dynamics and porating electric fields for phospholipid bilayers. *J Phys Chem B* **112**, 13588-13596 (2008).
56. T. Kotnik, L. Rems, M. Tarek, D. Miklavcic, Membrane Electroporation and Electropermeabilization: Mechanisms and Models. *Annu Rev Biophys* **48**, 63-91 (2019).
57. J. Gumbart, F. Khalili-Araghi, M. Sotomayor, B. Roux, Constant electric field simulations of the membrane potential illustrated with simple systems. *Biochim Biophys Acta* **1818**, 294-302 (2012).
58. S. A. Kirsch, R. A. Bockmann, Membrane pore formation in atomistic and coarse-grained simulations. *Biochim Biophys Acta* **1858**, 2266-2277 (2016).
59. M. A. Via, J. Klug, N. Wilke, L. S. Mayorga, M. G. Del Popolo, The interfacial electrostatic potential modulates the insertion of cell-penetrating peptides into lipid bilayers. *Phys Chem Chem Phys* **20**, 5180-5189 (2018).
60. J. Lin, A. Alexander-Katz, Cell membranes open "doors" for cationic nanoparticles/biomolecules: insights into uptake kinetics. *ACS Nano* **7**, 10799-10808 (2013).
61. H. D. Herce *et al.*, Arginine-rich peptides destabilize the plasma membrane, consistent with a pore formation translocation mechanism of cell-penetrating peptides. *Biophys J* **97**, 1917-1925 (2009).
62. M. M. R. Moghal, M. Z. Islam, F. Hossain, S. K. Saha, M. Yamazaki, Role of Membrane Potential on Entry of Cell-Penetrating Peptide Transportan 10 into Single Vesicles. *Biophys J* **118**, 57-69 (2020).
63. X. Zhang *et al.*, Endocytosis and membrane potential are required for HeLa cell uptake of R.I.-CKTat9, a retro-inverso Tat cell penetrating peptide. *Mol Pharm* **6**, 836-848 (2009).

64. Z. A. Levine, P. T. Vernier, Life cycle of an electropore: field-dependent and field-independent steps in pore creation and annihilation. *J Membr Biol* **236**, 27-36 (2010).
65. M. Tarek, Membrane electroporation: a molecular dynamics simulation. *Biophys J* **88**, 4045-4053 (2005).
66. M. Tokman *et al.*, Electric field-driven water dipoles: nanoscale architecture of electroporation. *PLoS One* **8**, e61111 (2013).
67. M. Casciola *et al.*, Properties of lipid electropores I: Molecular dynamics simulations of stabilized pores by constant charge imbalance. *Bioelectrochemistry* **109**, 108-116 (2016).
68. D. A. Los, N. Murata, Membrane fluidity and its roles in the perception of environmental signals. *Biochim Biophys Acta* **1666**, 142-157 (2004).
69. A. A. Gurtovenko, I. Vattulainen, Ion leakage through transient water pores in protein-free lipid membranes driven by transmembrane ionic charge imbalance. *Biophys J* **92**, 1878-1890 (2007).
70. L. Delemotte, F. Dehez, W. Treptow, M. Tarek, Modeling membranes under a transmembrane potential. *J Phys Chem B* **112**, 5547-5550 (2008).
71. F. E. Herrera, S. Pantano, Salt induced asymmetry in membrane simulations by partial restriction of ionic motion. *J Chem Phys* **130**, 195105 (2009).
72. A. M. Bowman, O. M. Nesin, O. N. Pakhomova, A. G. Pakhomov, Analysis of plasma membrane integrity by fluorescent detection of Tl(+) uptake. *J Membr Biol* **236**, 15-26 (2010).
73. R. G. Thorne, C. Nicholson, In vivo diffusion analysis with quantum dots and dextrans predicts the width of brain extracellular space. *Proceedings of the National Academy of Sciences* **103**, 5567-5572 (2006).
74. D. J. Mitchell, D. T. Kim, L. Steinman, C. G. Fathman, J. B. Rothbard, Polyarginine enters cells more efficiently than other polycationic homopolymers. *J Pept Res* **56**, 318-325 (2000).
75. R. Wallbrecher *et al.*, Membrane permeation of arginine-rich cell-penetrating peptides independent of transmembrane potential as a function of lipid composition and membrane fluidity. *J Control Release* **256**, 68-78 (2017).
76. Y. Rao, S. J. Kwok, J. Lombardi, N. J. Turro, K. B. Eisenthal, Label-free probe of HIV-1 TAT peptide binding to mimetic membranes. *Proc Natl Acad Sci U S A* **111**, 12684-12688 (2014).
77. G. Grasso *et al.*, Cell penetrating peptide modulation of membrane biomechanics by Molecular dynamics. *J Biomech* **73**, 137-144 (2018).
78. H. L. Amand *et al.*, Cell surface binding and uptake of arginine- and lysine-rich penetratin peptides in absence and presence of proteoglycans. *Biochim Biophys Acta* **1818**, 2669-2678 (2012).
79. L. Li, I. Vorobyov, T. W. Allen, The different interactions of lysine and arginine side chains with lipid membranes. *J Phys Chem B* **117**, 11906-11920 (2013).
80. C. T. Armstrong, P. E. Mason, J. L. Anderson, C. E. Dempsey, Arginine side chain interactions and the role of arginine as a gating charge carrier in voltage sensitive ion channels. *Sci Rep* **6**, 21759 (2016).
81. S. S. Daoud, R. L. Juliano, Reduced toxicity and enhanced antitumor effects in mice of the ionophoric drug valinomycin when incorporated in liposomes. *Cancer Res* **46**, 5518-5523 (1986).
82. S. C. Gad, C. Reilly, K. Siino, F. A. Gavigan, G. Witz, Thirteen cationic ionophores: their acute toxicity, neurobehavioral and membrane effects. *Drug Chem Toxicol* **8**, 451-468 (1985).
83. *Antibiotics and Chemotherapy* **12**, 482 (1962).
84. K. Bansal *et al.*, A Facile Approach for Synthesis and Intracellular Delivery of Size Tunable Cationic Peptide Functionalized Gold Nanohybrids in Cancer Cells. *Bioconjug Chem* **29**, 1102-1110 (2018).
85. I. A. Khalil, S. Kimura, Y. Sato, H. Harashima, Synergism between a cell penetrating peptide and a pH-sensitive cationic lipid in efficient gene delivery based on double-coated nanoparticles. *J Control Release* **275**, 107-116 (2018).

86. Y. Wu, J. Sun, A. Li, D. Chen, The promoted delivery of RRM2 siRNA to vascular smooth muscle cells through liposome-polycation-DNA complex conjugated with cell penetrating peptides. *Biomed Pharmacother* **103**, 982-988 (2018).
87. C. Jeong, J. Yoo, D. Lee, Y. C. Kim, A branched TAT cell-penetrating peptide as a novel delivery carrier for the efficient gene transfection. *Biomater Res* **20**, 28 (2016).
88. K. M. Kauffman *et al.*, A major lineage of non-tailed dsDNA viruses as unrecognized killers of marine bacteria. *Nature* **554**, 118-122 (2018).
89. H. Yin *et al.*, A fusion peptide directs enhanced systemic dystrophin exon skipping and functional restoration in dystrophin-deficient mdx mice. *Hum Mol Genet* **18**, 4405-4414 (2009).
90. L. Du *et al.*, Arginine-rich cell-penetrating peptide dramatically enhances AMO-mediated ATM aberrant splicing correction and enables delivery to brain and cerebellum. *Hum Mol Genet* **20**, 3151-3160 (2011).
91. M. Westerfield, The Zebrafish Book. A Guide for the Laboratory Use of Zebrafish (Danio rerio), 4th Edition. *University of Oregon Press, Eugene.*

, (2000).
92. A. Vaslin, J. Puyal, T. Borsello, P. G. Clarke, Excitotoxicity-related endocytosis in cortical neurons. *J Neurochem* **102**, 789-800 (2007).
93. K. Weber, U. Bartsch, C. Stocking, B. Fehse, A multicolor panel of novel lentiviral "gene ontology" (LeGO) vectors for functional gene analysis. *Mol Ther* **16**, 698-706 (2008).
94. A. Annibaldi, A. Dousse, S. Martin, J. Tazi, C. Widmann, Revisiting G3BP1 as a RasGAP Binding Protein: Sensitization of Tumor Cells to Chemotherapy by the RasGAP 317-326 Sequence Does Not Involve G3BP1. *PLoS One* **6**, (2011).
95. Z. Krasznai, T. Marian, L. Balkay, M. Emri, L. Tron, Flow cytometric determination of absolute membrane potential of cells. *J Photochem Photobiol B* **28**, 93-99 (1995).
96. T. Klapperstuck, D. Glanz, M. Klapperstuck, J. Wohlrab, Methodological aspects of measuring absolute values of membrane potential in human cells by flow cytometry. *Cytometry A* **75**, 593-608 (2009).
97. L. Cueni *et al.*, T-type Ca2+ channels, SK2 channels and SERCAs gate sleep-related oscillations in thalamic dendrites. *Nat Neurosci* **11**, 683-692 (2008).
98. D. S. Adams, M. Levin, Measuring resting membrane potential using the fluorescent voltage reporters DiBAC4(3) and CC2-DMPE. *Cold Spring Harb Protoc* **2012**, 459-464 (2012).
99. Y. Qi *et al.*, CHARMM-GUI Martini Maker for Coarse-Grained Simulations with the Martini Force Field. *J Chem Theory Comput* **11**, 4486-4494 (2015).
100. S. Jo, T. Kim, V. G. Iyer, W. Im, CHARMM-GUI: a web-based graphical user interface for CHARMM. *J Comput Chem* **29**, 1859-1865 (2008).
101. T. A. Wassenaar, H. I. Ingolfsson, R. A. Bockmann, D. P. Tieleman, S. J. Marrink, Computational Lipidomics with insane: A Versatile Tool for Generating Custom Membranes for Molecular Simulations. *J Chem Theory Comput* **11**, 2144-2155 (2015).
102. S. J. Marrink, A. H. de Vries, A. E. Mark, Coarse Grained Model for Semiquantitative Lipid Simulations. *The Journal of Physical Chemistry B* **108**, 750-760 (2004).
103. S. O. Yesylevskyy, L. V. Schafer, D. Sengupta, S. J. Marrink, Polarizable water model for the coarse-grained MARTINI force field. *PLoS Comput Biol* **6**, e1000810 (2010).
104. A. Lamiable *et al.*, PEP-FOLD3: faster de novo structure prediction for linear peptides in solution and in complex. *Nucleic Acids Res* **44**, W449-454 (2016).
105. G. Grasso *et al.*, Cell Penetrating Peptide Adsorption on Magnetite and Silica Surfaces: A Computational Investigation. *J Phys Chem B* **119**, 8239-8246 (2015).
106. X. Periole, M. Cavalli, S. J. Marrink, M. A. Ceruso, Combining an Elastic Network With a Coarse-Grained Molecular Force Field: Structure, Dynamics, and Intermolecular Recognition. *J Chem Theory Comput* **5**, 2531-2543 (2009).

107. G. Bussi, D. Donadio, M. Parrinello, Canonical sampling through velocity rescaling. *J Chem Phys* **126**, 014101 (2007).
108. H. J. C. Berendsen, Postma, J.P.M, van Gunsteren, W.F., DiNola, A. and Haak, J.R.. Molecular dynamics with coupling to an external bath. *The Journal of Chemical Physics* **81**, 3684-3690 (1984).
109. T. Darden, York, D. & Pedersen, L., Particle mesh Ewald: An N ·log(N) method for Ewald sums in large systems. *J. Chem. Phys.* **98**, 10089-10092 (1993).
110. W. Humphrey, A. Dalke, K. Schulten, VMD: visual molecular dynamics. *J Mol Graph* **14**, 33-38, 27-38 (1996).
111. M. J. Abraham *et al.*, GROMACS: High performance molecular simulations through multi-level parallelism from laptops to supercomputers. *SoftwareX* **1-2**, 19-25 (2015).
112. M. a. R. Parrinello, A., Polymorphic Transitions in Single Crystals: A New Molecular Dynamics Method. *Journal of Applied Physics* **52**, 7182-7190 (1981).
113. H. Leontiadou, A. E. Mark, S. J. Marrink, Molecular dynamics simulations of hydrophilic pores in lipid bilayers. *Biophys J* **86**, 2156-2164 (2004).
114. M. Matthews, Z. M. Varga, Anesthesia and euthanasia in zebrafish. *ILAR J* **53**, 192-204 (2012).
115. M. Jordan, A. Schallhorn, F. M. Wurm, Transfecting mammalian cells: optimization of critical parameters affecting calcium-phosphate precipitate formation. *Nucleic Acids Res* **24**, 596-601 (1996).
116. O. Shalem *et al.*, Genome-scale CRISPR-Cas9 knockout screening in human cells. *Science* **343**, 84-87 (2014).
117. W. Li *et al.*, MAGeCK enables robust identification of essential genes from genome-scale CRISPR/Cas9 knockout screens. *Genome Biol* **15**, 554 (2014).
118. F. A. Ran *et al.*, Genome engineering using the CRISPR-Cas9 system. *Nat Protoc* **8**, 2281-2308 (2013).

Figure 1

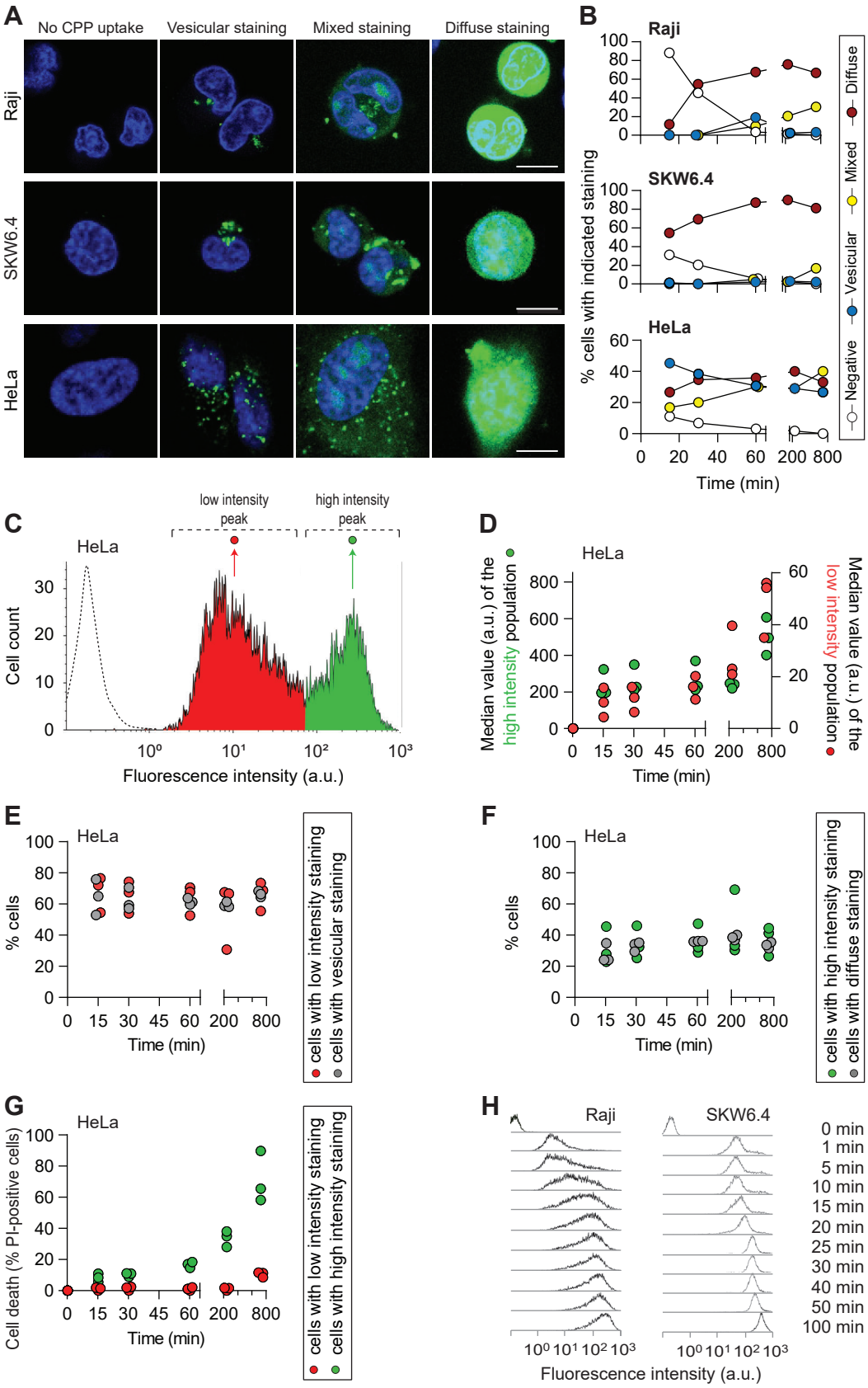
A
No CPP uptake
Vesicular staining
Mixed staining
Diffuse staining
Raji
SKW6.4
HeLa
B
Raji
SKW6.4
HeLa
% cells with indicated staining
Time (min)
Diffuse
Mixed
Vesicular
Negative
C
HeLa
low intensity peak
high intensity peak
Cell count
Fluorescence intensity (a.u.)
D
HeLa
Median value (a.u.) of the high intensity population
Median value (a.u.) of the low intensity population
Time (min)
E
HeLa
% cells
Time (min)
cells with low intensity staining
cells with vesicular staining
F
HeLa
% cells
Time (min)
cells with high intensity staining
cells with diffuse staining
G
HeLa
Cell death (% PI-positive cells)
Time (min)
cells with low intensity staining
cells with high intensity staining
H
Raji
SKW6.4
0 min
1 min
5 min
10 min
15 min
20 min
25 min
30 min
40 min
50 min
100 min
Fluorescence intensity (a.u.)

Figure 2

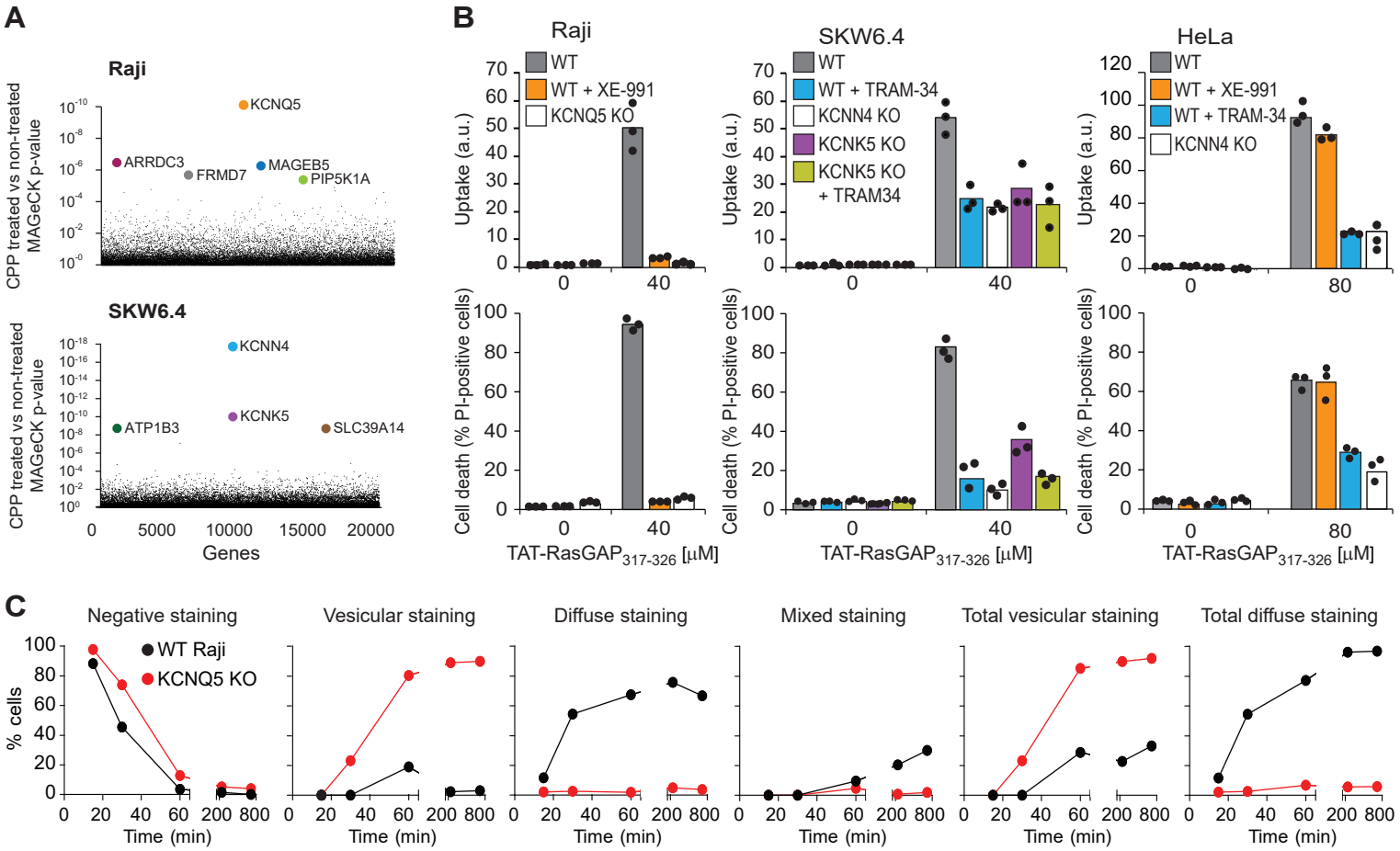
A
Raji
KCNQ5
ARRDC3
FRMD7
MAGEB5
PIP5K1A
CPP treated vs non-treated MAGeCK p-value
SKW6.4
KCNN4
KCNK5
ATP1B3
SLC39A14
Genes
B
Raji
SKW6.4
HeLa
WT
WT + XE-991
KCNQ5 KO
WT + TRAM-34
KCNN4 KO
KCNK5 KO
KCNK5 KO + TRAM34
Uptake (a.u.)
Cell death (% PI-positive cells)
TAT-RasGAP317-326 [µM]
C
Negative staining
Vesicular staining
Diffuse staining
Mixed staining
Total vesicular staining
Total diffuse staining
WT Raji
KCNQ5 KO
% cells
Time (min)

Figure 3

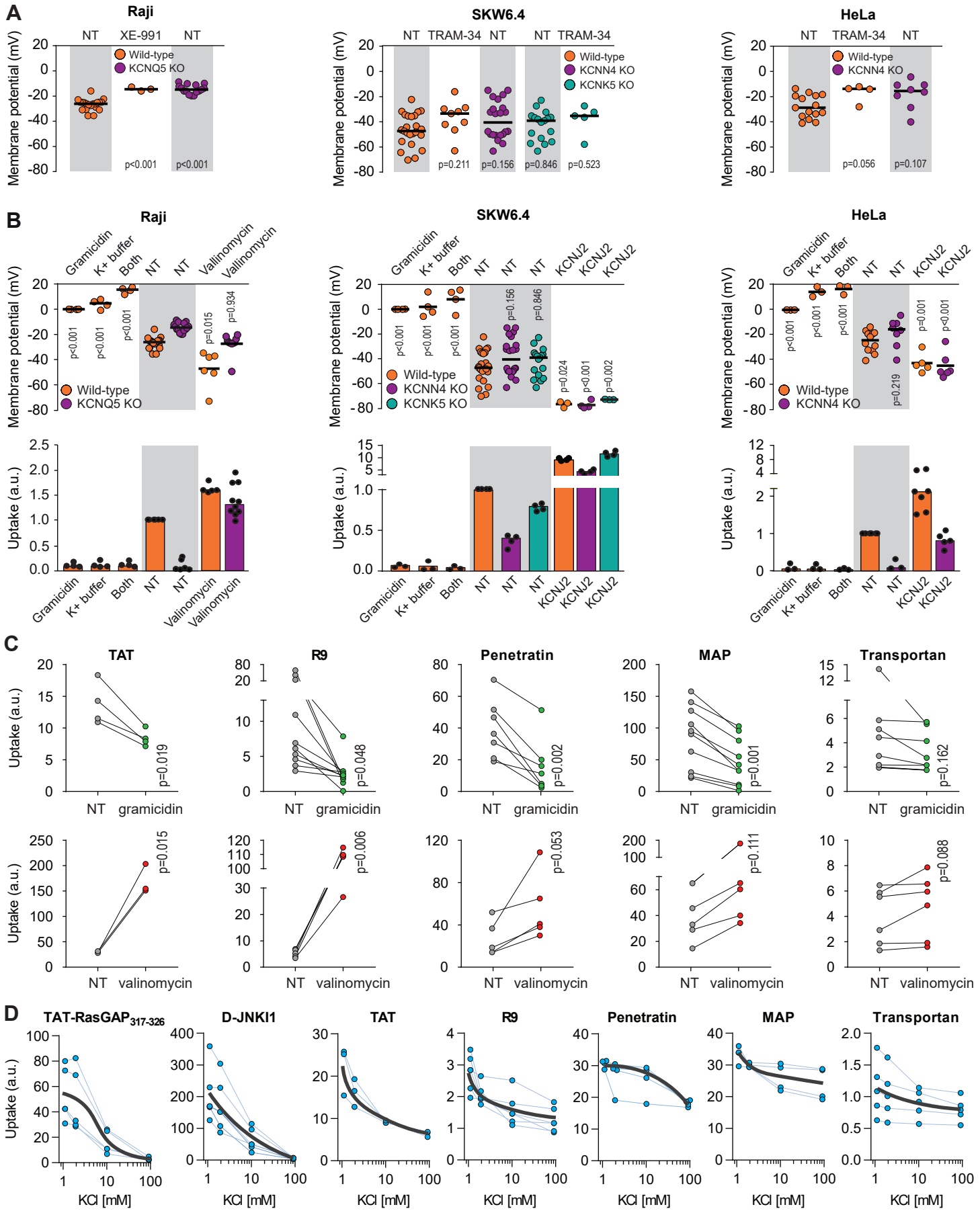
A
Raji
SKW6.4
HeLa
NT
XE-991
TRAM-34
Membrane potential (mV)
Wild-type
KCNQ5 KO
KCNN4 KO
KCNK5 KO
p<0.001
p=0.211
p=0.156
p=0.846
p=0.523
p=0.056
p=0.107
B
Gramicidin
K+ buffer
Both
Valinomycin
KCNJ2
Uptake (a.u.)
p=0.015
p=0.934
p=0.024
p=0.002
p=0.219
p=0.001
C
TAT
R9
Penetratin
MAP
Transportan
gramicidin
valinomycin
p=0.019
p=0.048
p=0.002
p=0.001
p=0.162
p=0.015
p=0.006
p=0.053
p=0.111
p=0.088
D
TAT-RasGAP317-326
D-JNKI1
KCl [mM]

Figure 4

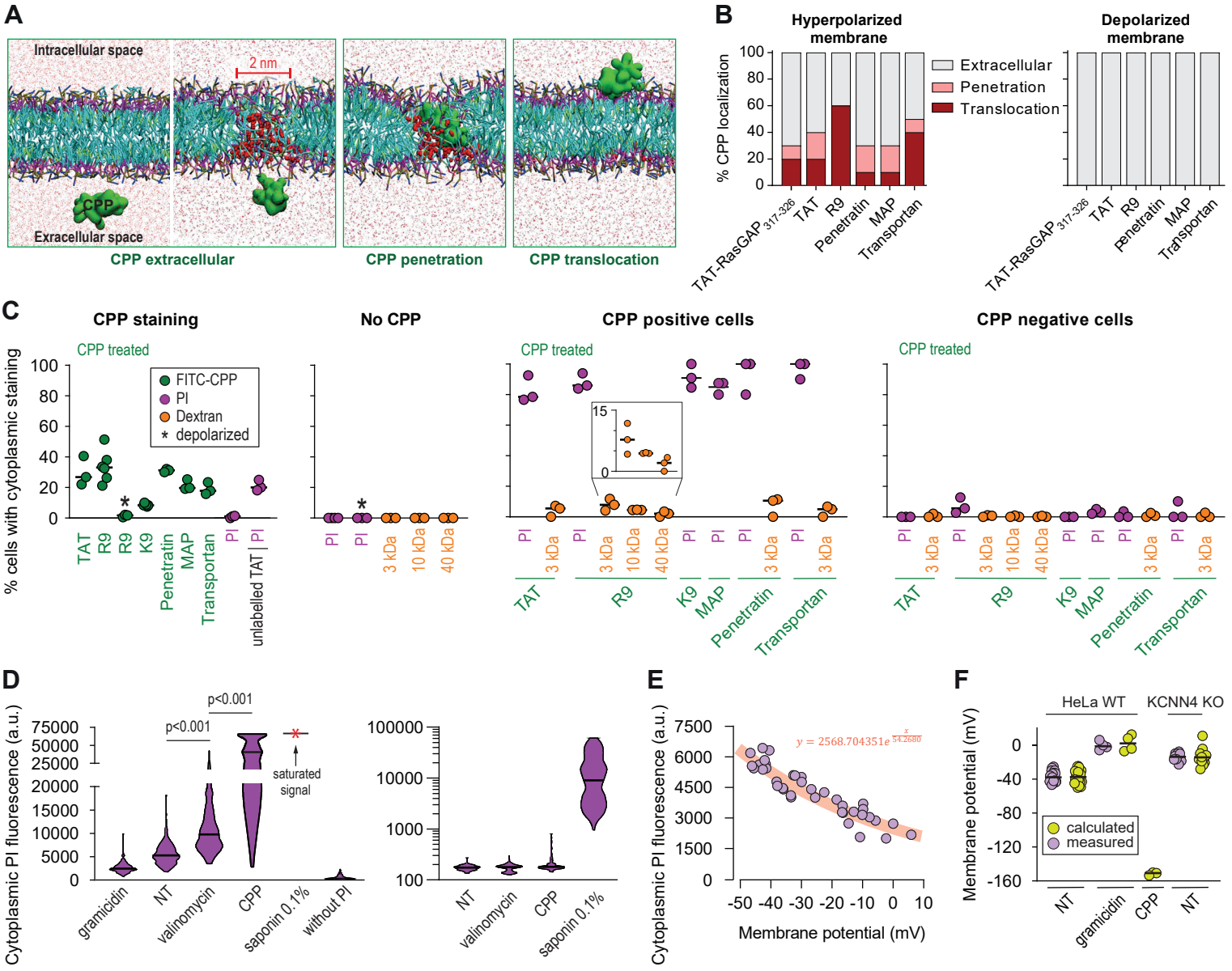
A
Intracellular space
2 nm
CPP
Exracellular space
CPP extracellular
CPP penetration
CPP translocation
B
Hyperpolarized membrane
Depolarized membrane
% CPP localization
Extracellular
Penetration
Translocation
TAT-RasGAP317-326
TAT
R9
Penetratin
MAP
Transportan
C
CPP staining
No CPP
CPP positive cells
CPP negative cells
CPP treated
% cells with cytoplasmic staining
FITC-CPP
PI
Dextran
depolarized
unlabelled TAT | PI
3 kDa
10 kDa
40 kDa
D
Cytoplasmic PI fluorescence (a.u.)
p<0.001
saturated signal
gramicidin
NT
valinomycin
CPP
saponin 0.1%
without PI
E
Cytoplasmic PI fluorescence (a.u.)
Membrane potential (mV)
F
HeLa WT
KCNN4 KO
Membrane potential (mV)
calculated
measured

Figure 5

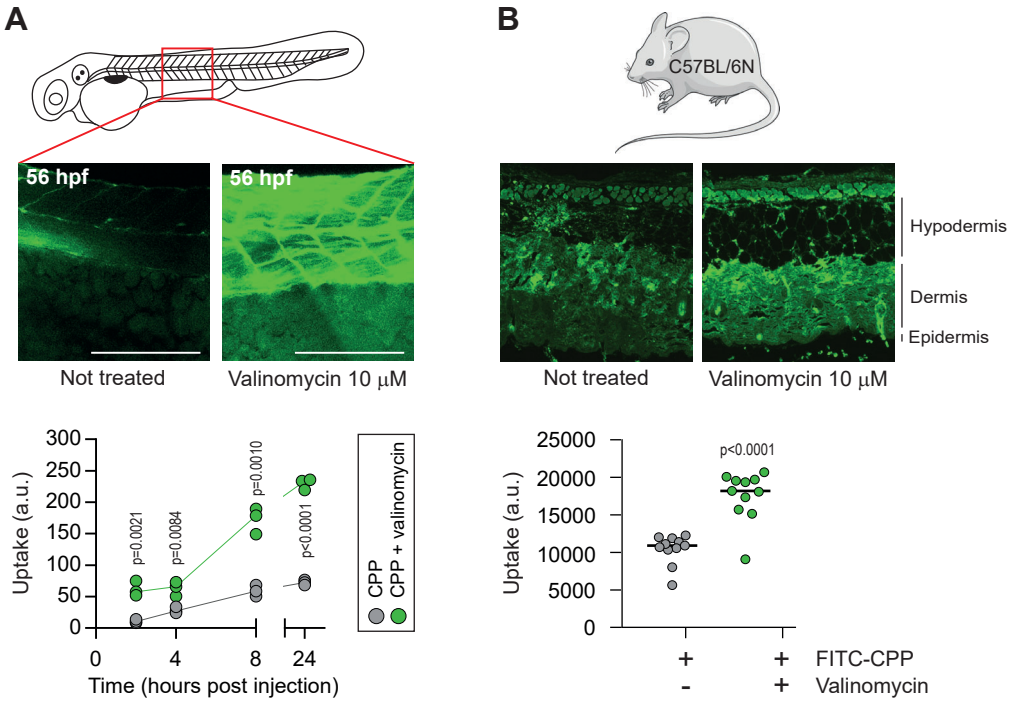
A
56 hpf
56 hpf
Not treated
Valinomycin 10 μM
Uptake (a.u.)
300
250
200
150
100
50
0
p=0.0021
p=0.0084
p=0.0010
p<0.0001
0
4
8
24
Time (hours post injection)
CPP
CPP + valinomycin
B
C57BL/6N
Hypodermis
Dermis
Epidermis
Not treated
Valinomycin 10 μM
Uptake (a.u.)
25000
20000
15000
10000
5000
0
p<0.0001
+
+
FITC-CPP
-
+
Valinomycin

Figure S1

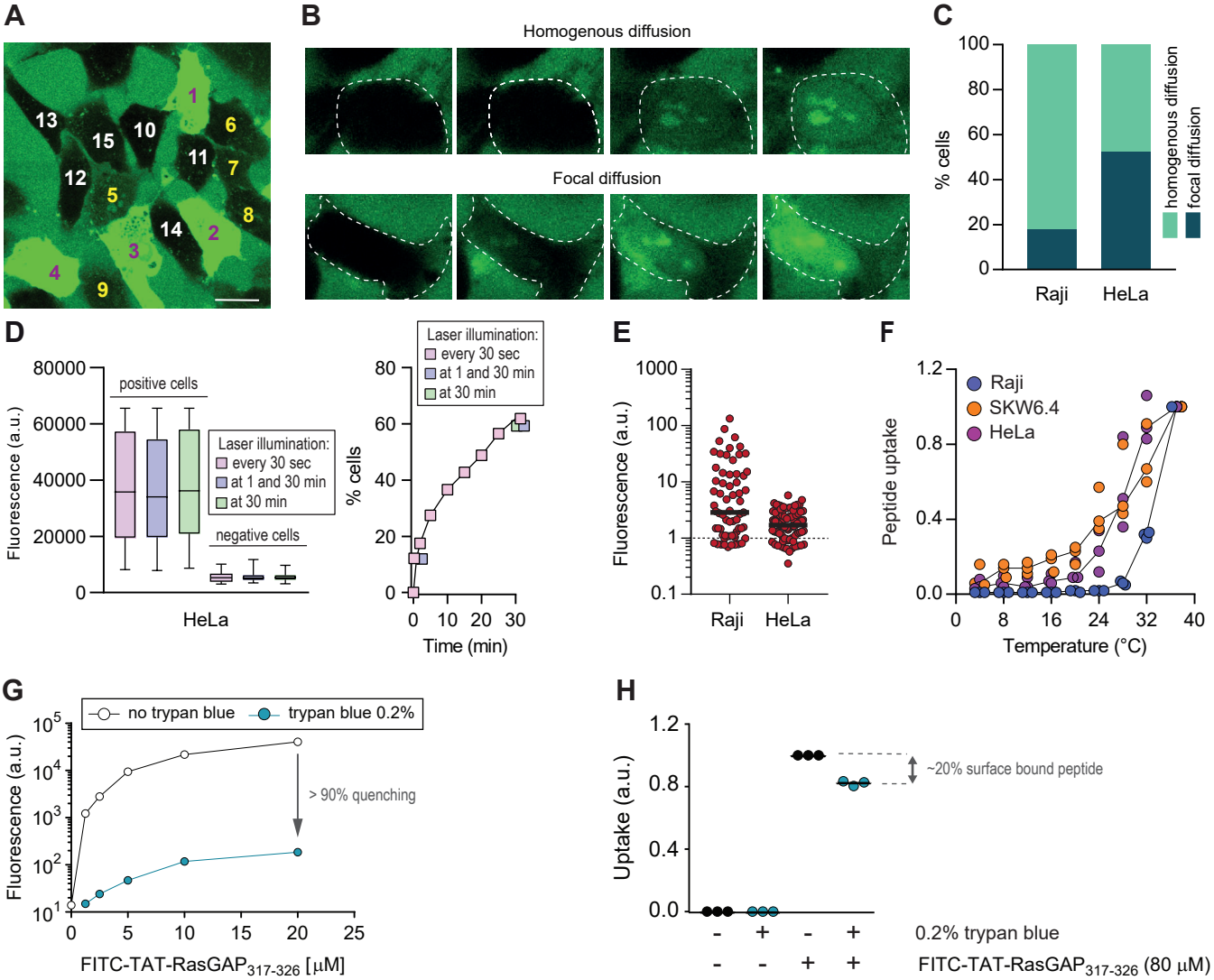
A
B
Homogenous diffusion
Focal diffusion
C
% cells
homogenous diffusion
focal diffusion
Raji
HeLa
D
Fluorescence (a.u.)
positive cells
negative cells
Laser illumination:
every 30 sec
at 1 and 30 min
at 30 min
HeLa
% cells
Time (min)
E
Fluorescence (a.u.)
Raji
HeLa
F
Peptide uptake
Raji
SKW6.4
HeLa
Temperature (°C)
G
no trypan blue
trypan blue 0.2%
Fluorescence (a.u.)
> 90% quenching
FITC-TAT-RasGAP317-326 [μM]
H
Uptake (a.u.)
~20% surface bound peptide
0.2% trypan blue
FITC-TAT-RasGAP317-326 (80 μM)

Figure S2

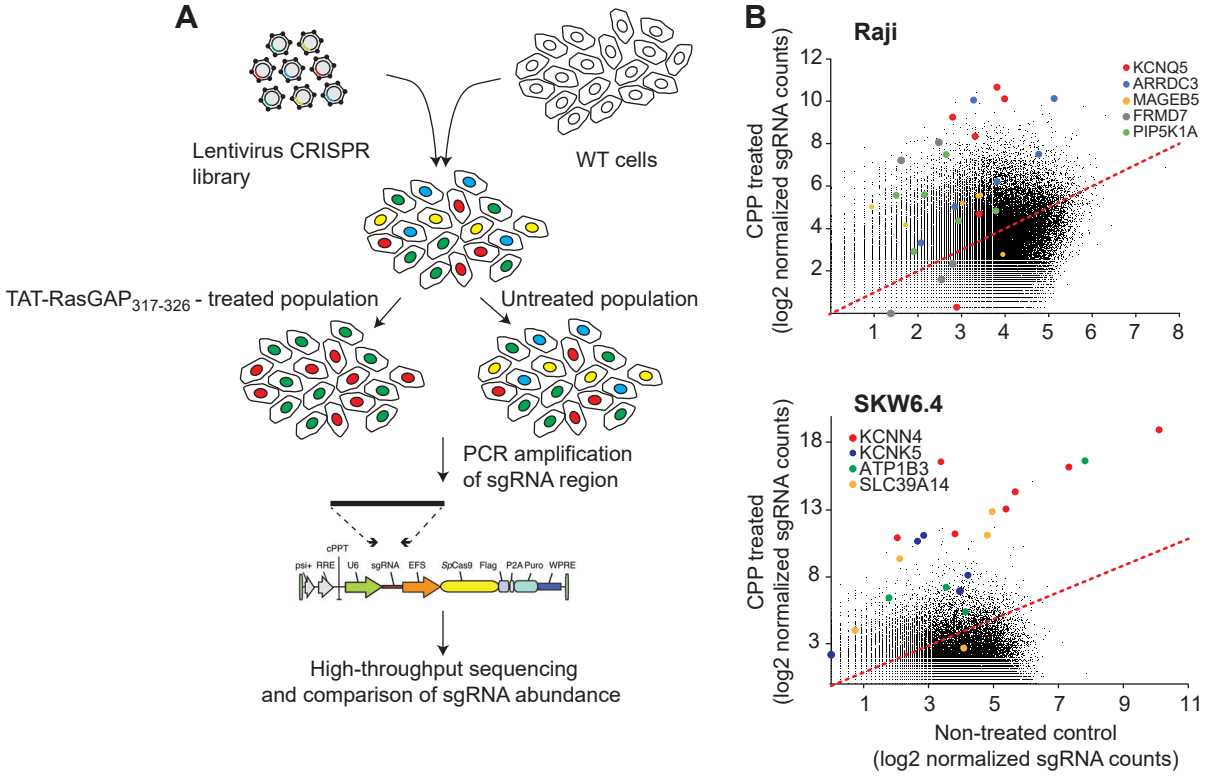
A
Lentivirus CRISPR library
WT cells
TAT-RasGAP317-326 - treated population
Untreated population
PCR amplification of sgRNA region
cPPT
psi+ RRE U6 sgRNA EFS SpCas9 Flag P2A Puro WPRE
High-throughput sequencing and comparison of sgRNA abundance
B
Raji
KCNQ5
ARRDC3
MAGEB5
FRMD7
PIP5K1A
CPP treated (log2 normalized sgRNA counts)
SKW6.4
KCNN4
KCNK5
ATP1B3
SLC39A14
Non-treated control (log2 normalized sgRNA counts)

Figure S3

A

Raji clone # Q5-1, KCNQ5 sequence

```
                  GC G  A  G
WT          TATCTAGGAATTAATCACA-GCTTGGTACATAGGTTTT
Allele 1    TATCTAGGAATTAATCACAAGCTTGGTACATAGGTTTT   +1  bp
Allele 2    TATCTAGGAATTAAT--------------------TTT   -20 bp
```

Raji clone # Q5-2, KCNQ5 sequence

```
WT          TATCTAGGAATTAATCACA-GCTTGGTACATAGGTTTT
Allele 1    TATCTAGGAATTAATCACA----TGGTACATAGGTTTT   -3  bp
Allele 2    TATCTAGGAATTAATCACAAGCTTGGTACATAGGTTTT   +1  bp
```

B

SKW6.4 clone # N4-1, KCNN4 sequence

```
WT          GAACATCCAGGCTTCTTGTAGCACTCGGGCAGCGGACTCCTT
Allele1     GAACATCCAGGCTTCTTGTAGC-------------ACTCCTT  -13 bp
Allele2     GAACATCCAGGCTTCTTGTAGC-------------ACTCCTT  -13 bp
```

SKW6.4 clone # N4-2, KCNN4 sequence

```
WT          GAACATCCAGGCTTCTTGTAGCACTCGGGCAGCGGACTCCTT
Allele1     GAACATCCAGGCTTCTTGTAGCACTCCGT------ACTCCTT   - 6 bp
Allele2     GAACATCCAGGCTTCTTGTAGCACTCCTT------ACTCCTT   - 6 bp
```

SKW6.4 clone # K5-1, KCNK5 sequence

```
WT          CACTGATCCACGTCAGGCAGAGCGGCACCCCGAAGAGACCAT
Allele_1    CACTGATCCACGTCAGGCA--------CCCCGAAGAGACCAT      -8 bp
Allele_2    CACTGATCCACGTCAGGCA--------CCCCGAAGAGACCAT      -8 bp
```

SKW6.4 clone # K5-2, KCNK5 sequence

```
WT          TTTTGCAGCGACCGTCATTACCACCATTGGTAAGTCTTCTGG
Allele_1    TTTTGCAGCGACCGTCATTACCA---TTGGTAAGTCTTCTGG   -3 bp
Allele_2    TTTTGCAGCGACCGTCATTAC--CCATTA------CTTCTGG   -8 bp
```

C

HeLa clone # N4-1, KCNN4 sequence

```
WT          TTCTTGTAGCACTCGGGCAGCGGACTCCTTCATCTGGGGGT
Allele 1    TTCTTGTAGCACTCGG----------------TCTGGGGGT   -16 bp
Allele 2    TTCTTGTAGC-----------GGACTCCTTCATCTGGGGGT   -11 bp
```

D

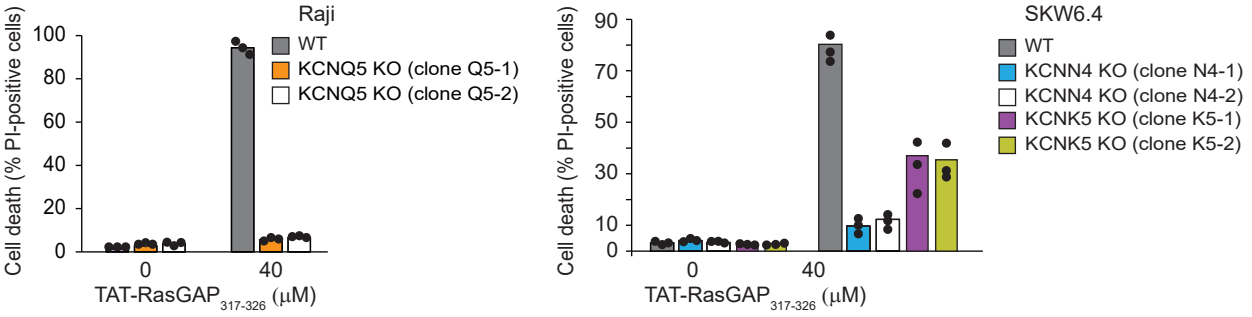

E

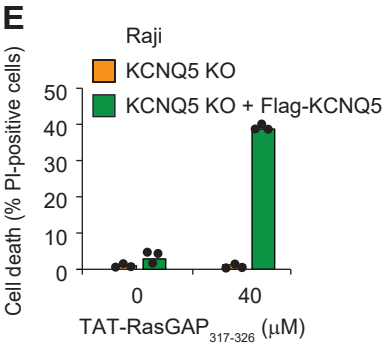

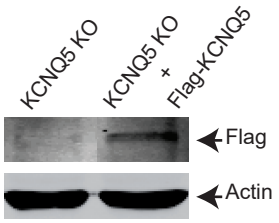

F

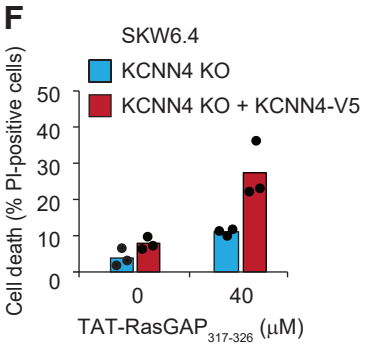

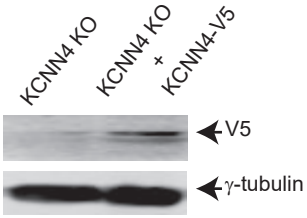

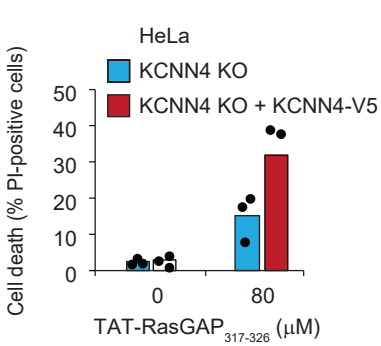

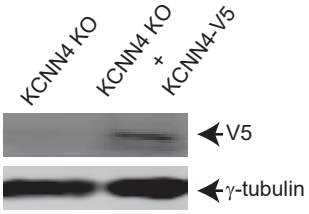

Figure S4

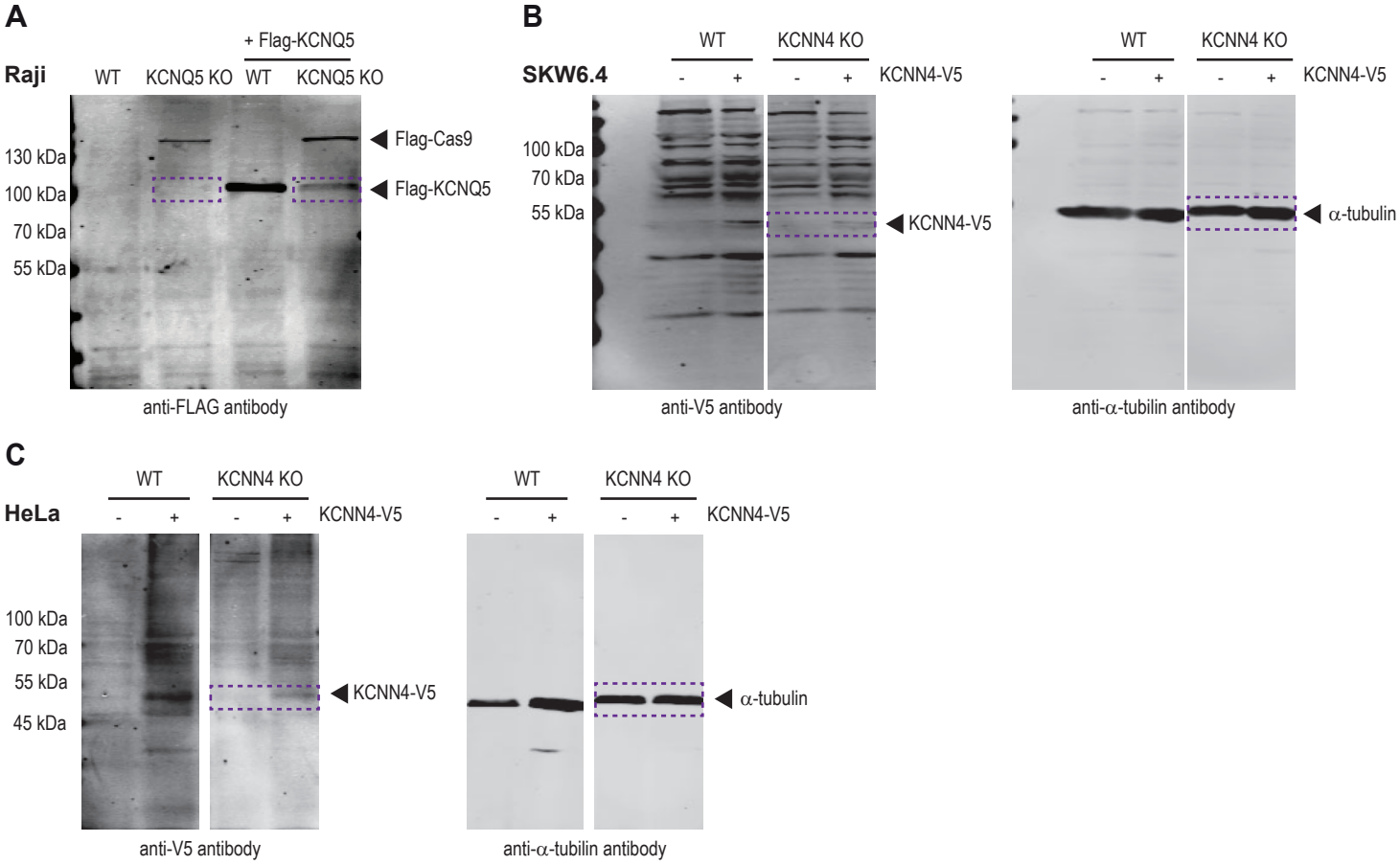
A
+ Flag-KCNQ5
Raji
WT
KCNQ5 KO
WT
KCNQ5 KO
130 kDa
100 kDa
70 kDa
55 kDa
Flag-Cas9
Flag-KCNQ5
anti-FLAG antibody
B
WT
KCNN4 KO
SKW6.4
-
+
-
+
KCNN4-V5
100 kDa
70 kDa
55 kDa
KCNN4-V5
anti-V5 antibody
WT
KCNN4 KO
-
+
-
+
KCNN4-V5
α-tubulin
anti-α-tubilin antibody
C
WT
KCNN4 KO
HeLa
-
+
-
+
KCNN4-V5
100 kDa
70 kDa
55 kDa
45 kDa
KCNN4-V5
anti-V5 antibody
WT
KCNN4 KO
-
+
-
+
KCNN4-V5
α-tubulin
anti-α-tubilin antibody

Figure S5

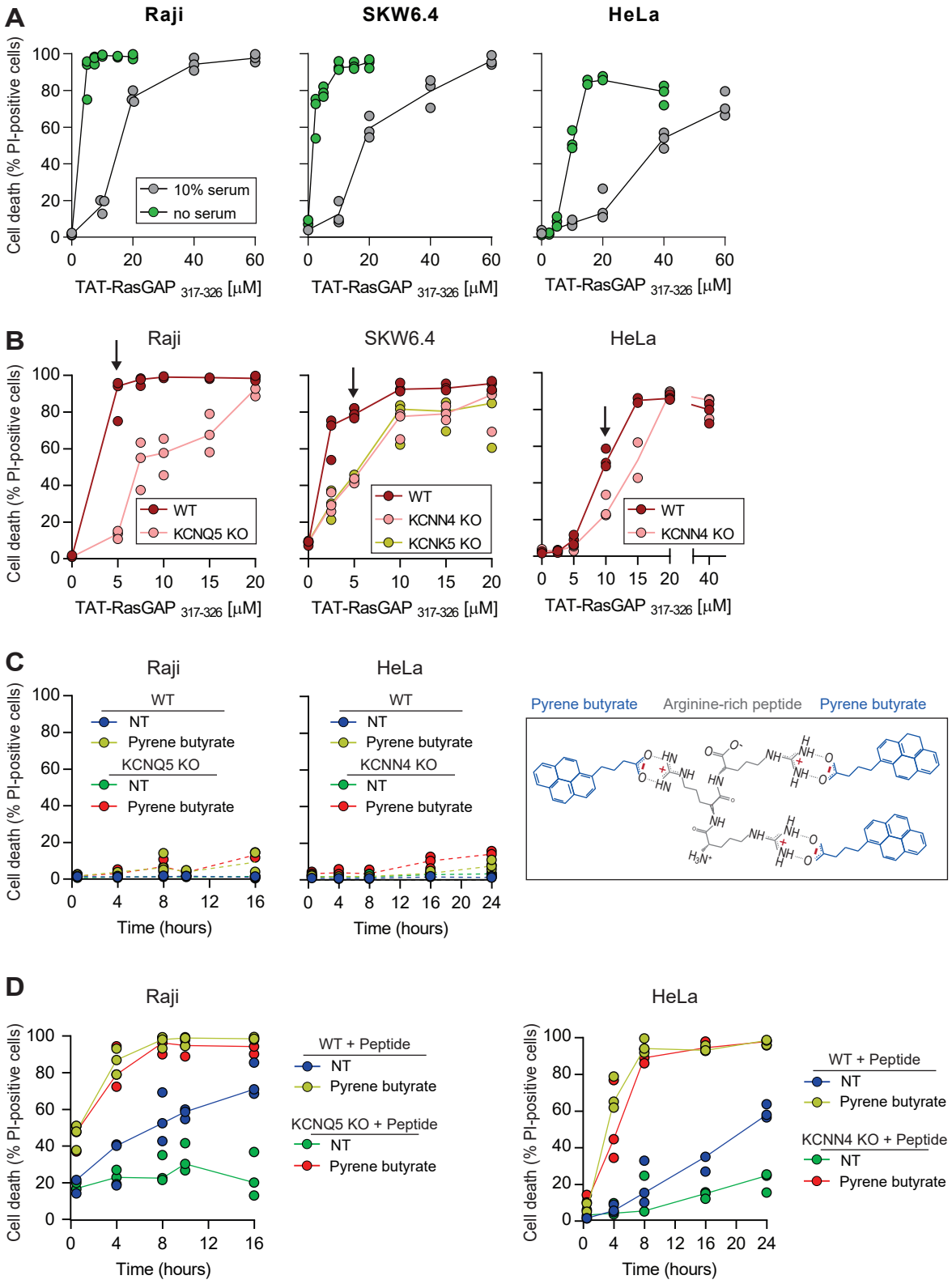
A
Raji
SKW6.4
HeLa
Cell death (% PI-positive cells)
10% serum
no serum
TAT-RasGAP 317-326 [μM]
B
Raji
SKW6.4
HeLa
WT
KCNQ5 KO
KCNN4 KO
KCNK5 KO
C
Raji
HeLa
WT
NT
Pyrene butyrate
KCNQ5 KO
KCNN4 KO
Time (hours)
Pyrene butyrate
Arginine-rich peptide
Pyrene butyrate
D
Raji
HeLa
WT + Peptide
KCNQ5 KO + Peptide
KCNN4 KO + Peptide

Figure S6

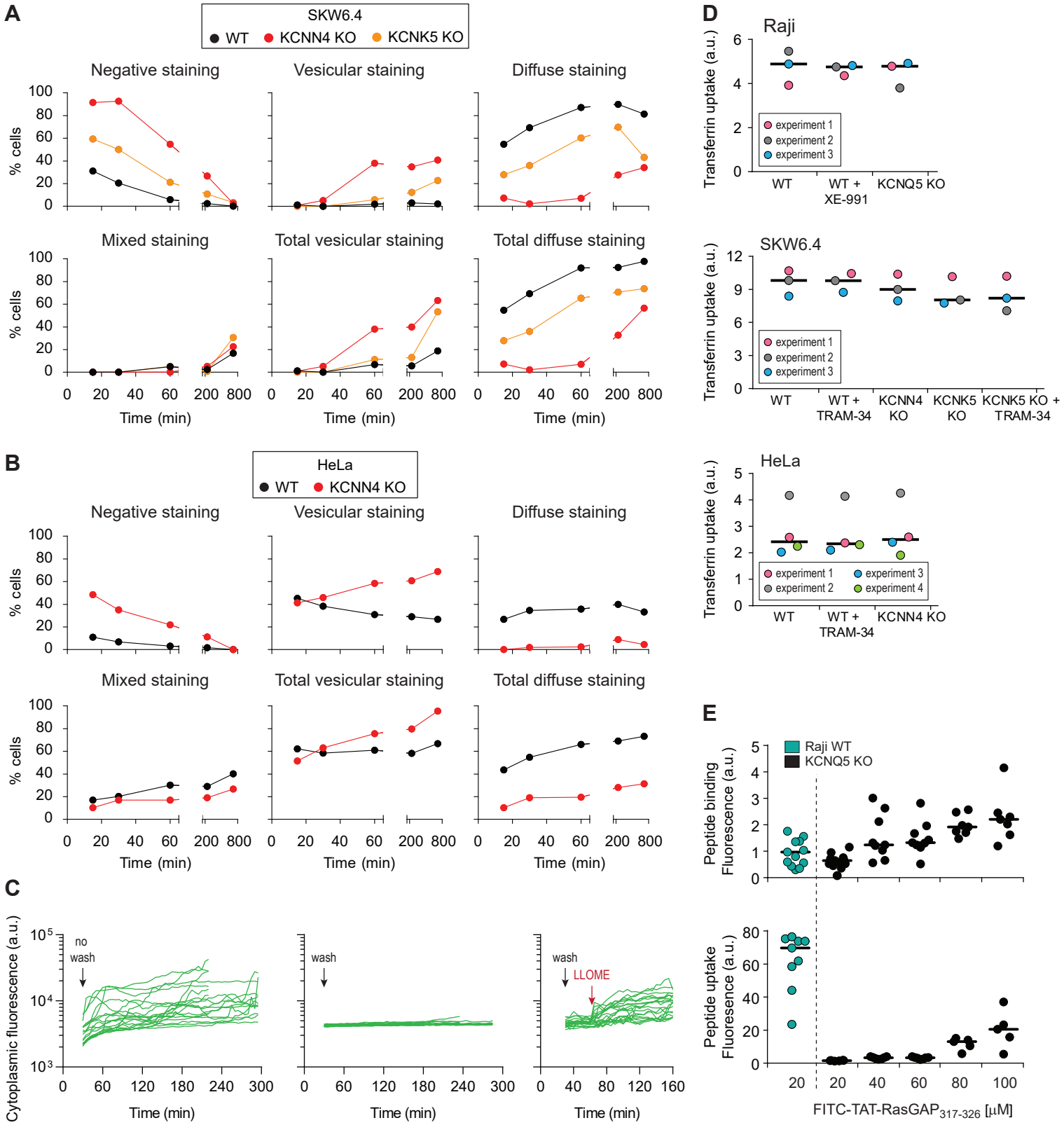
A
SKW6.4
WT
KCNN4 KO
KCNK5 KO
Negative staining
Vesicular staining
Diffuse staining
Mixed staining
Total vesicular staining
Total diffuse staining
% cells
Time (min)
B
HeLa
WT
KCNN4 KO
C
Cytoplasmic fluorescence (a.u.)
no wash
wash
LLOME
Time (min)
D
Raji
Transferrin uptake (a.u.)
experiment 1
experiment 2
experiment 3
WT
WT + XE-991
KCNQ5 KO
SKW6.4
WT + TRAM-34
KCNN4 KO
KCNK5 KO
KCNK5 KO + TRAM-34
HeLa
experiment 4
E
Raji WT
KCNQ5 KO
Peptide binding Fluorescence (a.u.)
Peptide uptake Fluorescence (a.u.)
FITC-TAT-RasGAP317-326 [µM]

Figure S7

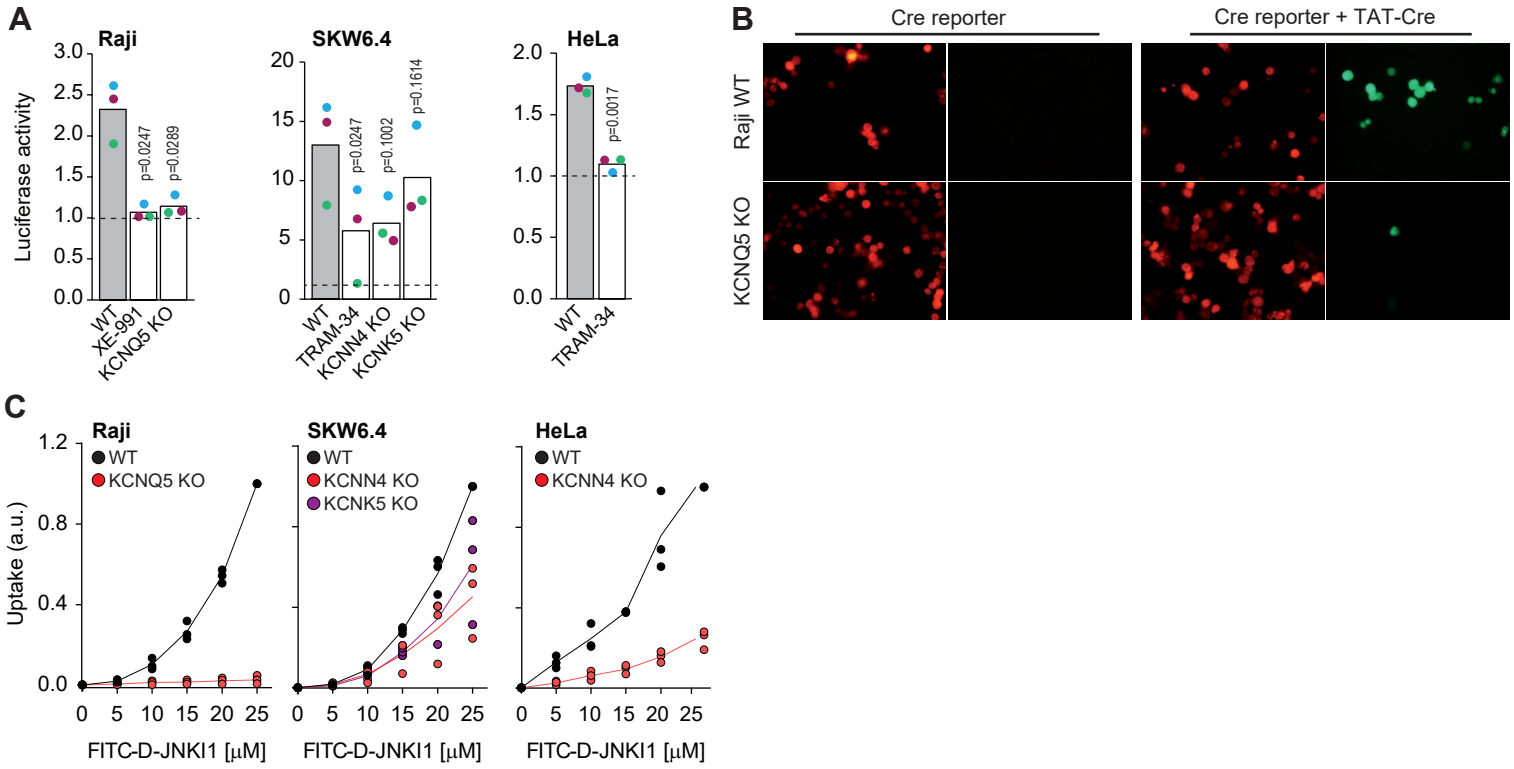
A
Raji
SKW6.4
HeLa
Luciferase activity
p=0.0247
p=0.0289
p=0.0247
p=0.1002
p=0.1614
p=0.0017
WT
XE-991
KCNQ5 KO
TRAM-34
KCNN4 KO
KCNK5 KO
B
Cre reporter
Cre reporter + TAT-Cre
Raji WT
KCNQ5 KO
C
Uptake (a.u.)
WT
KCNQ5 KO
KCNN4 KO
KCNK5 KO
FITC-D-JNKI1 [μM]

Figure S8

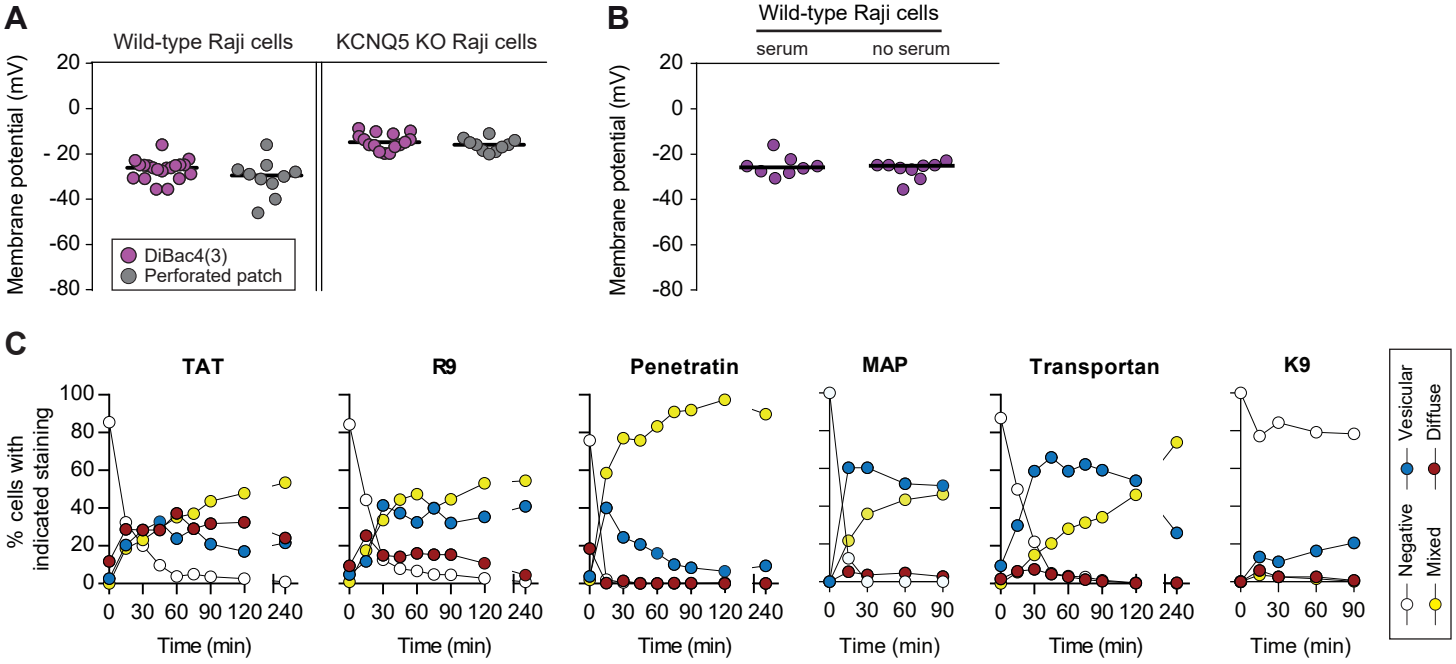

D

	Sequence	Net charge
R9	RRRRRRRRR	9
K9	KKKKKKKKK	9
TAT-RasGAP$_{317-326}$	GRKKRRQRRRGGWMWVTNLRTD	8
TAT$_{48-57}$	GRKKRRQRRR	8
Penetratin	RQIKIWFQNRRMKWKK	7
MAP	KLALKLALKALKAALKLA	5
Transportan	GWTLNSAGYLLGKINLKALAALAKKIL	4

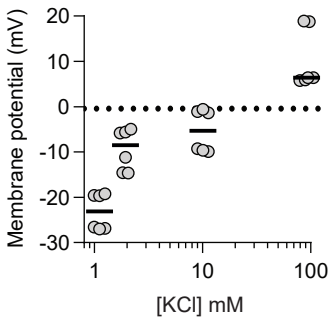

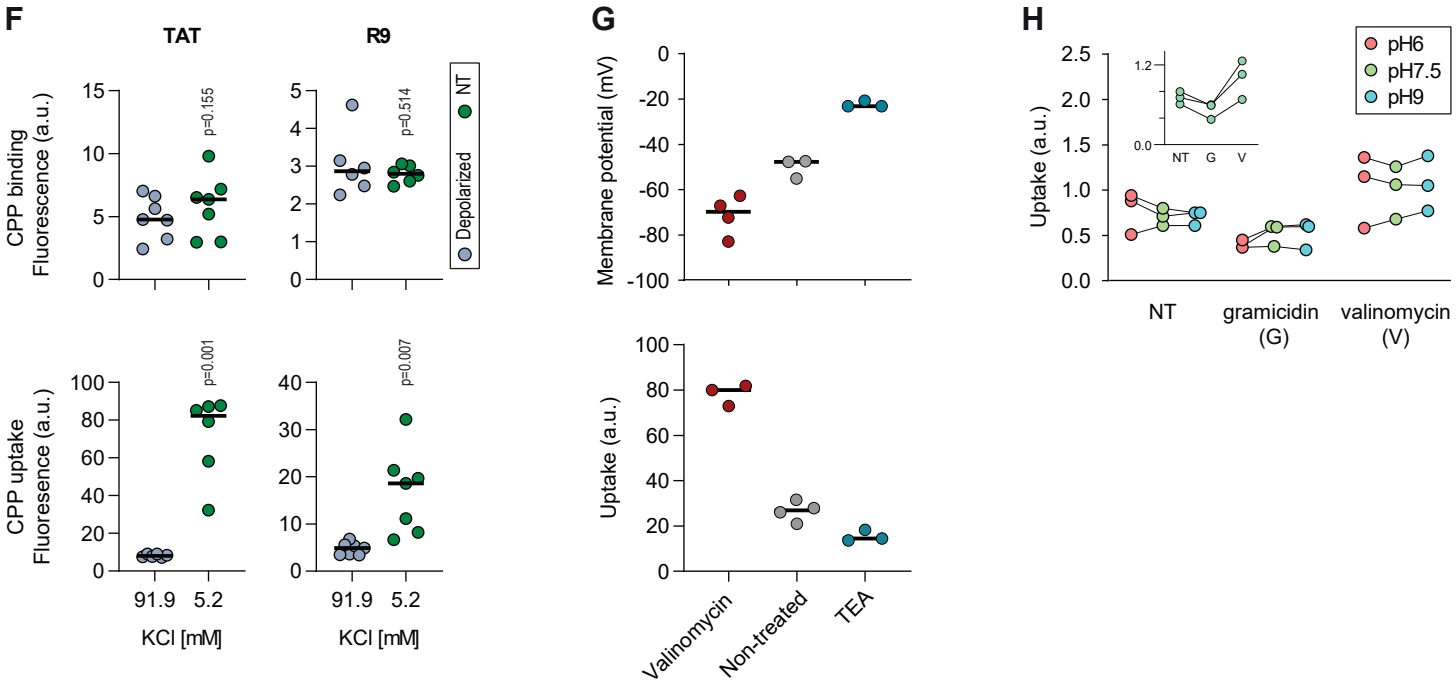

Figure S9

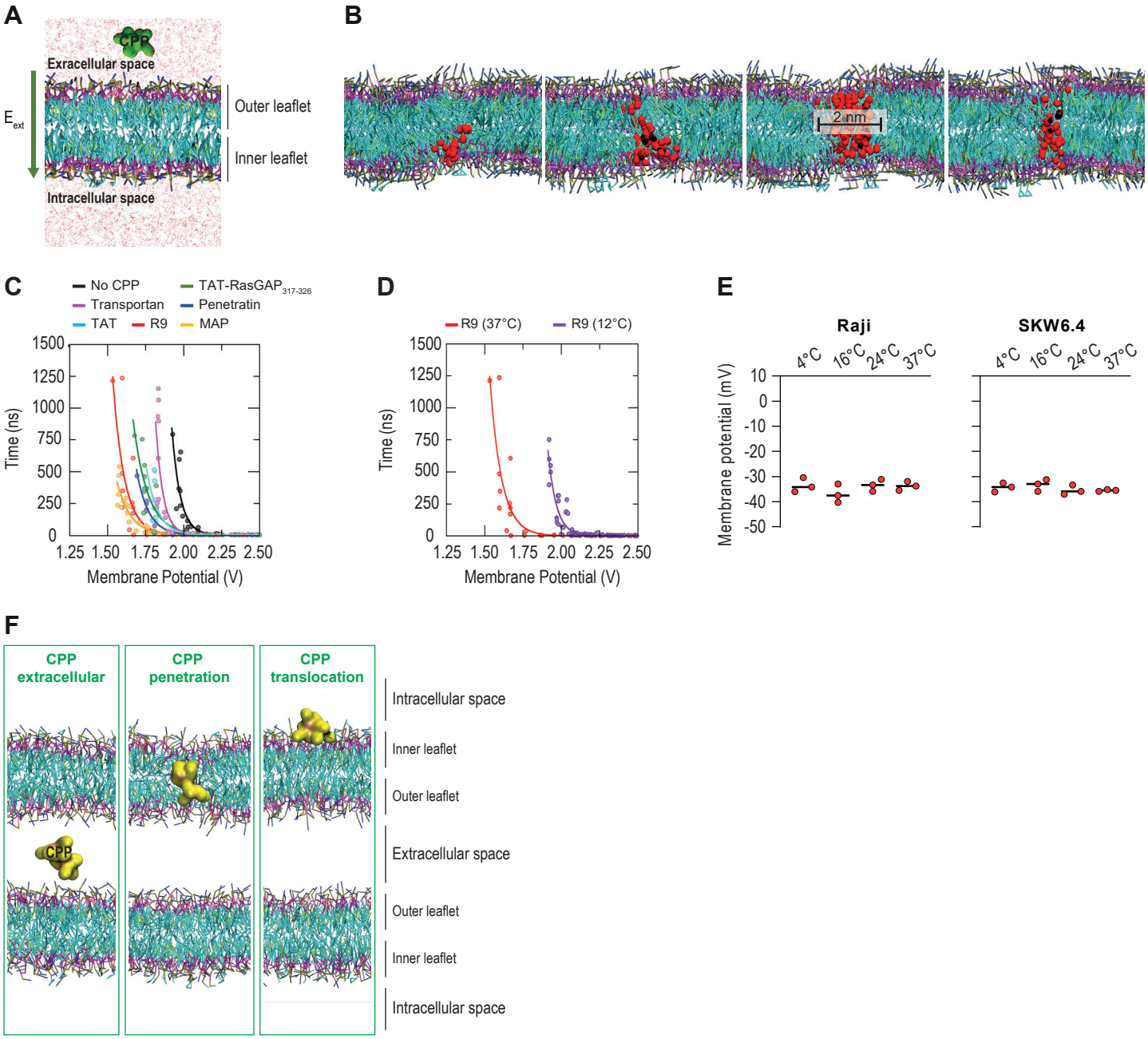
A
CPP
Exracellular space
E_{ext}
Outer leaflet
Inner leaflet
Intracellular space
B
2 nm
C
No CPP
TAT-RasGAP317-326
Transportan
Penetratin
TAT
R9
MAP
Time (ns)
Membrane Potential (V)
D
R9 (37°C)
R9 (12°C)
Time (ns)
Membrane Potential (V)
E
Raji
SKW6.4
4°C
16°C
24°C
37°C
Membrane potential (mV)
F
CPP extracellular
CPP penetration
CPP translocation
CPP
Intracellular space
Inner leaflet
Outer leaflet
Extracellular space
Outer leaflet
Inner leaflet
Intracellular space

Figure S10

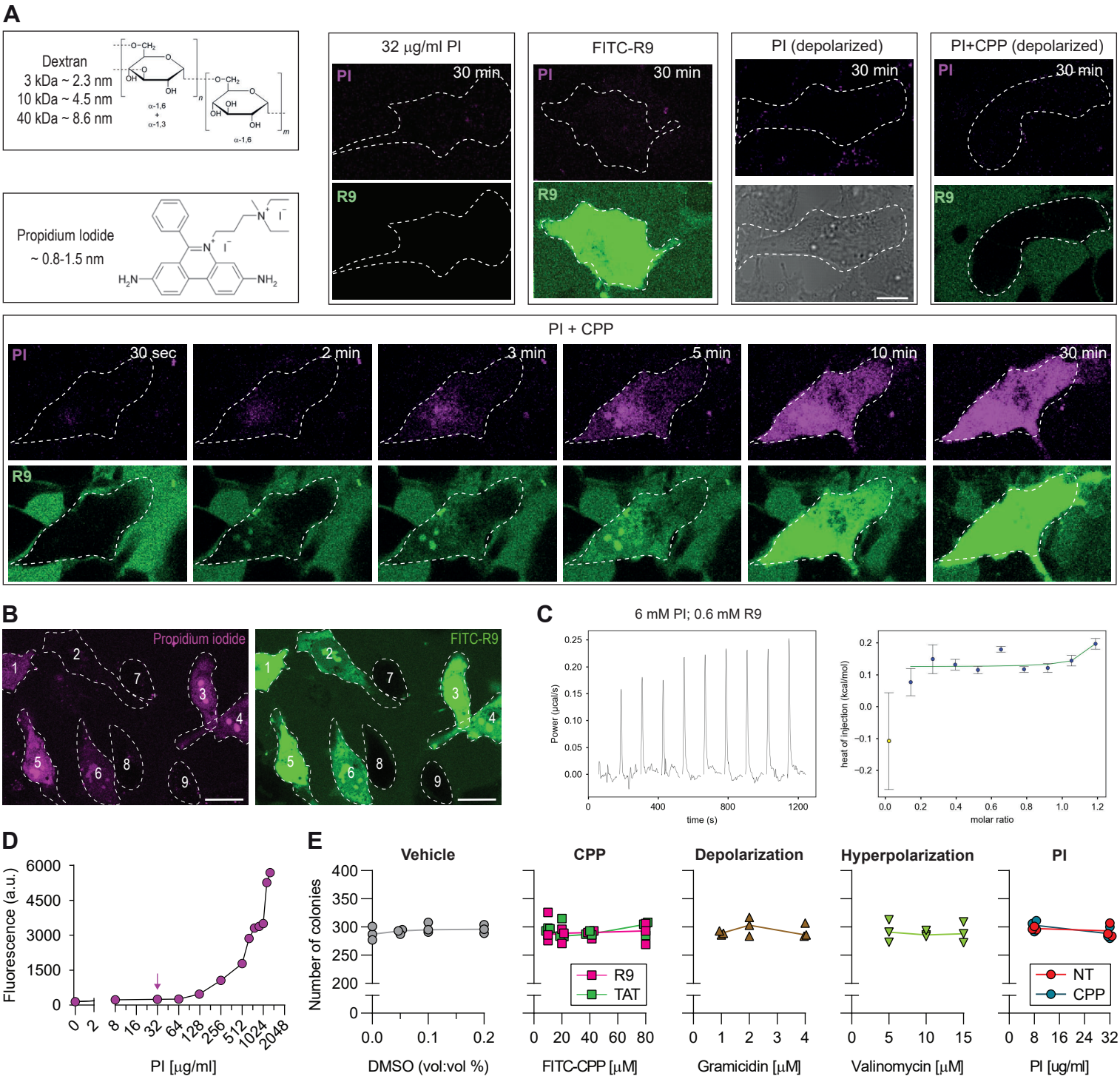
A
Dextran
3 kDa ~ 2.3 nm
10 kDa ~ 4.5 nm
40 kDa ~ 8.6 nm
α-1,6
+
α-1,3
α-1,6
Propidium Iodide
~ 0.8-1.5 nm
32 μg/ml PI
FITC-R9
PI (depolarized)
PI+CPP (depolarized)
PI
R9
30 min
PI + CPP
30 sec
2 min
3 min
5 min
10 min
30 min
B
Propidium iodide
FITC-R9
C
6 mM PI; 0.6 mM R9
Power (μcal/s)
time (s)
heat of injection (kcal/mol)
molar ratio
D
Fluorescence (a.u.)
PI [μg/ml]
E
Vehicle
CPP
Depolarization
Hyperpolarization
PI
Number of colonies
DMSO (vol:vol %)
FITC-CPP [μM]
Gramicidin [μM]
Valinomycin [μM]
PI [ug/ml]
R9
TAT
NT
CPP

Figure S11

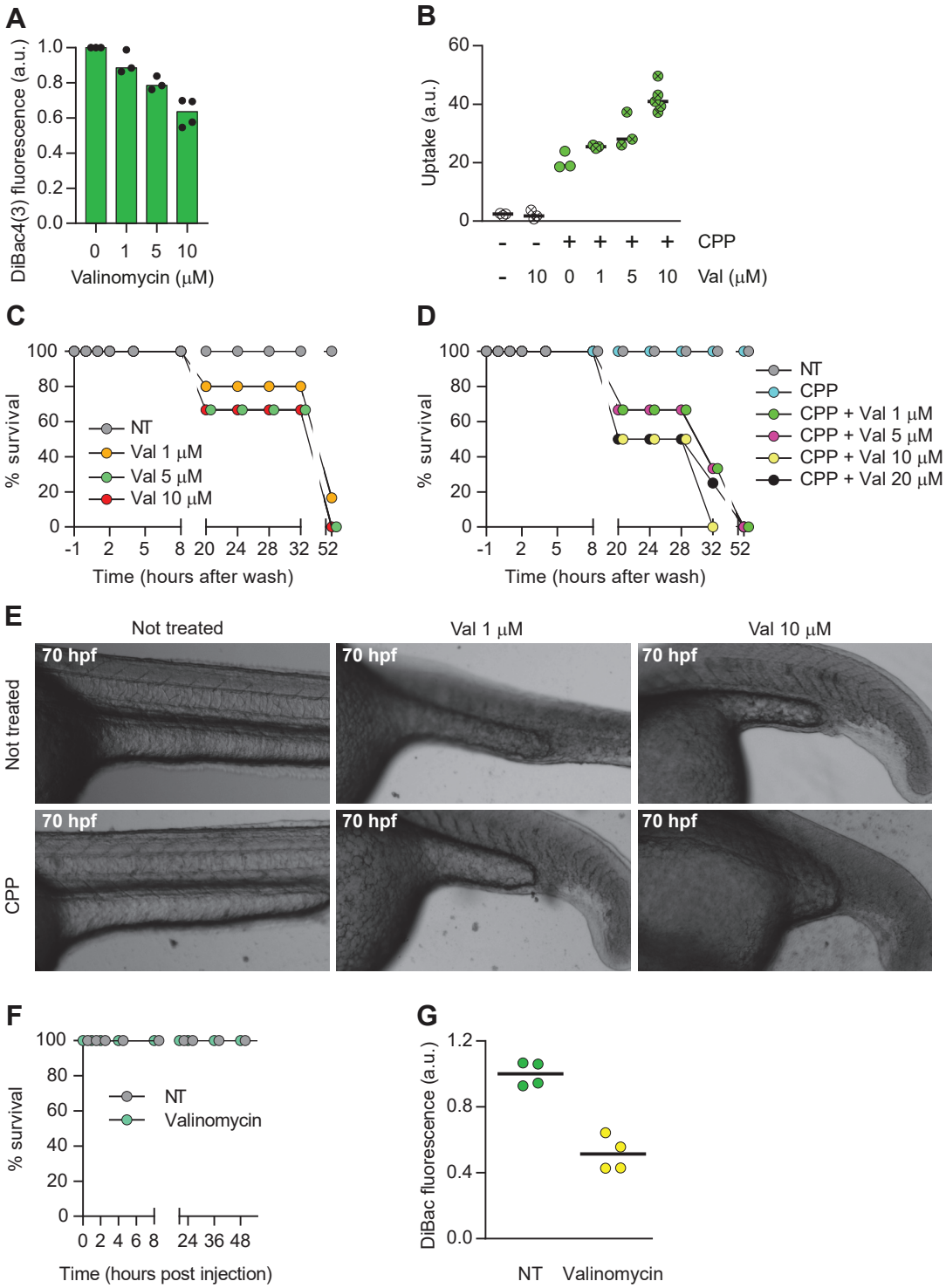
A
DiBac4(3) fluorescence (a.u.)
1.0
0.8
0.6
0.4
0.2
0.0
0 1 5 10
Valinomycin (μM)
B
Uptake (a.u.)
60
40
20
0
- - + + + + CPP
- 10 0 1 5 10 Val (μM)
C
% survival
100
80
60
40
20
0
NT
Val 1 μM
Val 5 μM
Val 10 μM
-1 2 5 8 20 24 28 32 52
Time (hours after wash)
D
% survival
NT
CPP
CPP + Val 1 μM
CPP + Val 5 μM
CPP + Val 10 μM
CPP + Val 20 μM
Time (hours after wash)
E
Not treated
Val 1 μM
Val 10 μM
Not treated
CPP
70 hpf
F
% survival
NT
Valinomycin
0 2 4 6 8 24 36 48
Time (hours post injection)
G
DiBac fluorescence (a.u.)
1.2
0.8
0.4
0.0
NT
Valinomycin

Figure S12

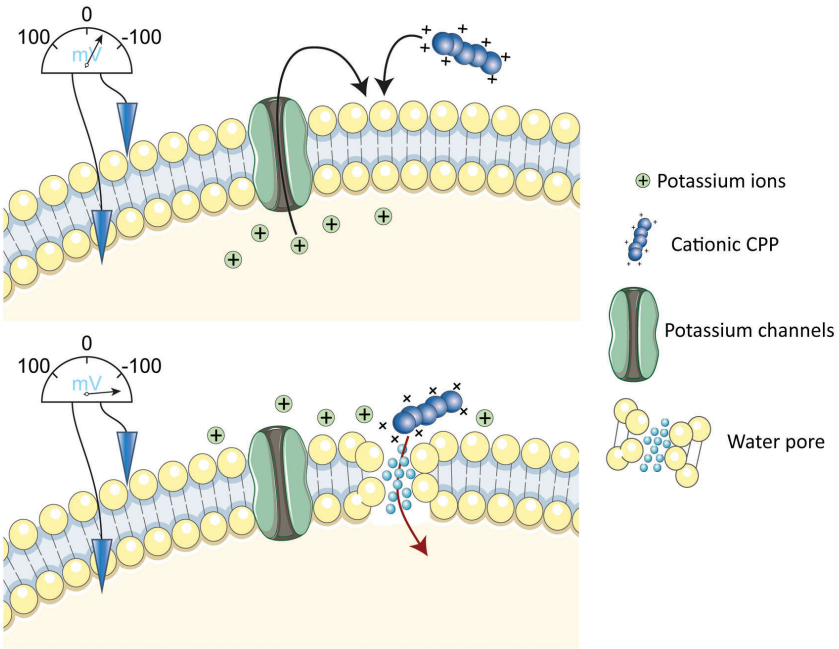
0
100
-100
mV
0
100
-100
mV
Potassium ions
Cationic CPP
Potassium channels
Water pore